SISSA

Scuola Internazionale Superiore di Studi Avanzati

Neuroscience Area – PhD course in

<Neurobiology>

The link between glioblastoma malignancy and calcium signalling

Thesis submitted for the degree of *"Doctor of Philosophy"*

Candidate:

Li Xiaoyun

Supervisor:

Prof. Vincent Torre

SISSA – Via Bonomea 265 – 34136 TRIESTE - Italy

Contents

List of publications

Li X., Spelat R., Bartolini A., Cesselli D., Ius T., Skrap M., Caponnetto F., Manini I., Yang Y., Torre V., Mechanisms of malignancy in glioblastoma cells are linked to mitochondrial Ca^{2+} uniporter upregulation and higher intracellular Ca^{2+} levels. *Journal of Cell Science* **2020**, 133(6).

Xiao M. [#], **Li X.** [#], Song, Q., Zhang Q., Lazzarino M., Cheng G.*, Ulloa Severino F. P.*, Torre V.*, A Fully 3D Interconnected Graphene-Carbon Nanotube Web Allows the Study of Glioma Infiltration in Bioengineered 3D Cortex-Like Networks. *Advanced materials* **2018,** *30* (52).

Molecular mechanisms of the blockage of glioblastoma motility. (In preparation).

1. Abstract

Glioblastoma (GBM), as one of the most malignant brain tumours, is mostly incurable. For a patient diagnosed with GBM, it is not a question whether the tumour will progress, but when and how fast the patient will die. In the past decades, medical doctors combined different treatments, such as surgical resection, radiation and chemotherapy, to save their lives. Unfortunately, the efficacy of these cures is limited, and patients usually die within 12-18 months. Researchers are trying to put immunotherapy, targeted therapy, and gene therapy into use [1]. So that revealing the molecular changes in GBM and figuring out biomarkers could promote the development of new GBM treatments.

Ca^{2+} signalling is crucial in cellular processes [2, 3], especially in cancer: cell proliferation, cell migration, metastasis and apoptosis. Mitochondrial Ca^{2+} uniporter (MCU), locating in the inner mitochondrial membrane, can regulate mitochondrial Ca^{2+} uptake and shape the amplitude and spatio-temporal patterns of Ca^{2+} signals [4]. According to previous research, MCU is highly expressed in GBM stem cells (GSC), embryonic stem cell lines (ESC) and GBM cell lines, compared with that in normal brain tissues [5].

The aims during my PhD:

- To establish a real-time method to measure Ca^{2+} concentration.
- To analyse Ca^{2+} signal and MCU expression level in GBM cells.
- To link these characteristics with GBM hallmarks: proliferation and migration.

I also tested GBM migration in a 3D neural scaffold in collaboration, and we compared the motility inhibition effects of inhibitors based on different molecular mechanisms.

The main results of my thesis:

1) By co-staining with Fluo-4 AM and Fura Red AM, we measured real-time Ca^{2+} oscillations in U87 GBM cell line, GSC cells and human astrocytes. The resting Ca^{2+} levels are similar, but Ca^{2+} signal amplitude in GBM cells is much higher than in human astrocytes.

2) MCU expression level in GBM cells is much higher than in human astrocytes. MCU knockdown in U87 GBM cells decreased Ca^{2+} signal amplitudes, cell proliferation and migration. MCU overexpression in human astrocytes increased Ca^{2+} signal level but triggered cell death, suggesting that human astrocytes cannot sustain a high Ca^{2+} level.

3) MCU silencing in U87 GBM cells decreased proliferation and migration. Cell proliferation was slowed down by arresting cells in the G1 phase.

4) We cultured healthy cortical cells on 3D Interconnected Graphene–Carbon Nanotube and establish an in vitro model. By culturing GBM cells in the 3D neural model, we investigated GBM cells infiltration and revealed its potential to screen anticancer drugs.

5) We employed three known inhibitors of small GTPases: ML141, R-ketorolac and EHT 1864. These three inhibitors can reduce the infiltration propensity of GBM cells by targeting two prototypical small Rho GTPase (Rac1 and Cdc42). The binding poses of these drugs on the target proteins provide a rationale at the atomic-level of detail of their non-competitive inhibition mechanism.

2. Introduction

Gliomas arise from glial or precursor cells and are thought to have potentially originated from the subventricular zone (SVZ) in the brain, where neural stem cells and neural progenitor cells are abundant [6, 7]. In general, gliomas include astrocytomas, oligodendrogliomas, oligoastrocytomas and glioblastomas (GBMs). GBM is the deadliest form of brain cancer, with an inferior prognosis. Scientists have been trying for decades to find effective treatment modalities to improve the life quality of GBM patients, prolong patients' life and even cure GBM. In fact, despite the significant advancements in therapeutic management, including surgical resection, radiotherapy, and chemotherapy, the median survival period for patients harbouring GBM remains less than 18 months [8]. GBM cells have the propensity to aggressively infiltrate/invade into the surrounding brain tissues and along the vascular tracks, which prevents complete resection of all malignant cells and limits the effect of localized radiotherapy while maintaining normal tissue [9]. The primary agent for GBM chemotherapy is temozolomide (TMZ) [10, 11], which can easily cross the blood-brain barrier but can only improve the median survival time of around three months. And then, to make matters worse, tumours recur almost in all cases [12]. In addition, GBM often causes other brain diseases [13-15], such as herniation, cerebral injury and cerebral haemorrhage, which can be lethal. However, the survival period of GBM patients can be variable and difficult to predict, which suggests unknown factors that are not yet well understood.

Nowadays, more and more scientists focus on revealing the molecular changes in GBM and are trying to use immunotherapy, targeted therapy and gene therapy to treat GBM [16-19]. Nevertheless, there remain few effective therapies due to redundancy of intracellular signalling pathways, tumour molecular heterogeneity, and lack of validated biomarkers [1]. The Cancer Cell Map Initiative [20], a new effort, focuses on mapping the cancer gene network to identify key tumour drivers and the genetic influences on response to treatment. Such a genomic

platform is likely to improve patient diagnosis, risk stratification, and treatment selection basing on molecular drivers rather than histology alone in the future. Therefore, GBM researchers' challenges are to reveal more genetic alterations related to GBM and translate the well understand pathophysiology into effective therapies.

2.1 Malignant Brain Tumours

The World Health Organization has assigned brain tumour into four grades [21]: grade I pilocytic astrocytomas with low proliferative potential and the possibility of cure following surgical resection alone; grade II diffuse astrocytomas with low proliferative activity, but often recur; grade III anaplastic astrocytomas with high proliferative activity, and patients with anaplastic astrocytomas receive adjuvant radiation and/or chemotherapy and grade IV GBM with high proliferative activity and widespread infiltration of surrounding tissue, is often associated with rapid pre- and postoperative disease evolution and a fatal outcome [21-23]. According to the CBTRUS statistical report of malignant primary brain and other CNS tumours in the United States in 2010–2014 [24], around 47.1% is GBM (Figure 1).

GBM evolves in the limited space of the cranium. In order to survive and develop, it eliminates the surrounding population of cells using numerous combined strategies to create space and form a single organismal unit. GBM cells can release significant quantities of glutamate, which can help GBM cells resist apoptosis, promote the proliferation and invasion of glioma cells, and induce cell death of neurons at the tumour margin [25].

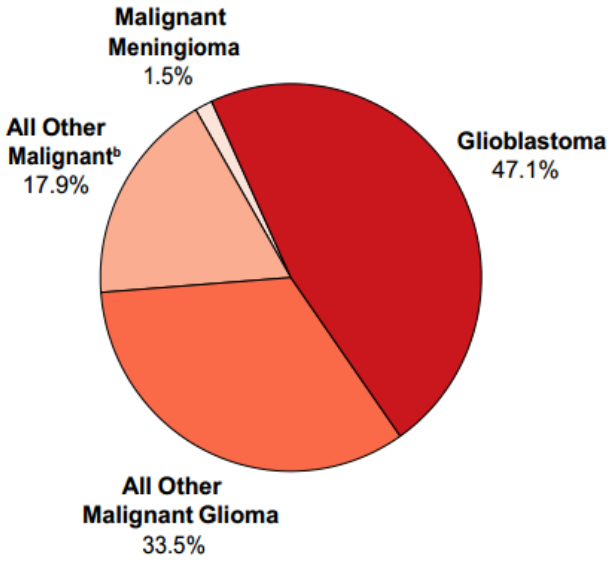

a. Percentages may not add up to 100% due to rounding.
b. Includes histologies with ICD-O-3 behavior code of 3 from choroid plexus tumors, neuronal and mixed neuronal glial tumors, tumors of the pineal region, embryonal tumors, nerve sheath tumors, mesenchymal tumors, primary melanocytic lesions, other neoplasms related to the meninges, lymphoma, other hemopoietic neoplasms, germ cell tumors, cysts and heterotopias, tumors of the pituitary, craniopharyngioma, hemangioma, neoplasm unspecified, and all other.

Figure 1. Distribution[a] of Malignant Primary Brain and Other CNS Tumours by Major Histology Groups (N=119,674). [24]

Currently, the standard approach in GBM treatment is maximum surgical resection plus radiation therapy and medical management/chemotherapy, considering that the entire tumour cannot be removed because GBM infiltrates surrounding tissue [26]. Despite this standard care, most patients with GBM do not survive beyond one year, and only about 5.5% survive beyond five years [24]. There are mainly three reasons: the blood-brain barrier (BBB), composed of continuous tight and adherent junctions between brain capillary endothelial cells, excludes the vast majority of cancer therapeutics from entering the brain parenchyma [27, 28]; glioma stem cells (GSCs), a population of cells that possess unique molecular signatures and reside within protective niches in the tumour, are a vital cause of treatment failure in GBM due to their intrinsic drug and radiation resistance and ability to repopulate the tumour mass [29, 30]; GBM cells have the propensity to aggressively infiltrate/invade into the surrounding

brain tissues and along the vascular tracks, which prevents complete resection of all malignant cells.

According to previous reports [31, 32], gene synthesis alterations can result in cell growth, proliferation, migration, angiogenesis and apoptosis. In this case, figuring out altered signalling pathways that are related to GBM and employing treatment targeting these signalling pathways become an innovative therapeutic method in GBM treatment, and some promising results have been achieved [24]. IL-13 Rα2 is present in over 75% of GBMs and is associated with activation of the phosphatidylinositol-3 kinase (PI3K)/Akt/mammalian target of rapamycin (mTOR) pathway [33], and is linked to increased tumour invasiveness and poor prognosis [34]. Besides, IL-13 Rα2 is specific for GBM tumour cells and limited expression in normal brain and other tissues [35]. In this case, IL-13 Rα2 has long been recognized as an attractive candidate for CAR T-cell targeting [36]. Approximately 40% of all newly diagnosed GBMs carry amplification of the EGFR gene, and about 50% of EGFR-amplified GBMs contain constitutively active and oncogenic EGFRvIII [37], and immunotherapy researches taking advantage of this character are carrying on.

2.2 Ca^{2+} signalling and cancer malignancy hallmarks

The concentration of cytosolic free Ca^{2+} ($[Ca^{2+}]_i$) (~100 nM) is 10000 times lower compared with the level of free Ca^{2+} in most extracellular fluids (>1 mM). This large concentration gradient is achieved by the Ca^{2+}-transporting ATPases, Na^+/Ca^{2+} exchangers and Ca^{2+}-binding proteins [38]. When cells are activated, Ca^{2+}-permeable ion channels open, and Ca^{2+} flow into the cells, which induces an increase in the $[Ca^{2+}]_i$ and Ca^{2+} oscillations. In order to detect and record these Ca^{2+} signals, plenty of calcium indicators, based upon selective calcium binding to fluorescent dyes that were made membrane-permeable temporarily [39-41], were put into use, and calcium imaging techniques developed. Traditional calcium imaging using calcium indicators can show the calcium signals in single cells, in microdomains [42, 43] such as dendritic spines or

synapses, even in thick samples such as mammalian brains. Cells usually choose a unique set of Ca^{2+} signals, including $[Ca^{2+}]_l$ level, to control its function. For example, dynamic changes in $[Ca^{2+}]_i$ contribute to key signalling cascades in brain cells, including the axonal release of neurotransmitters [44], dendritic control of synaptic plasticity [45], and intracellular communication in electrically passive astroglia [46]. In general, when $[Ca^{2+}]_i$ increases above the micromolar level, cell death can be initiated [47], but the precise dangerous level of $[Ca^{2+}]_i$ varies in different cell types. Therefore, to quantify the absolute intracellular calcium concentration can help us understand the cell functions regulated by $[Ca^{2+}]_i$. However, the usage of single-wavelength indicators in traditional calcium imaging is associated with variable dye loading and extrusion, making it difficult to accurately determine absolute Ca^{2+} concentration. With the development of fluorescent indicators, a class of calcium imaging indicators [48-50], which exhibit two peak excitation/emission wavelengths when either bound or free of Ca^{2+}, were applied to measure absolute Ca^{2+} concentration with ratiometric method. This class of indicators permits a very accurate quantification of Ca^{2+} concentration that is corrected for uneven dye loading, dye leakage, photo-bleaching and changes in cell volume, but at the cost of increased spectral bandwidth [51]. So imaging equipment that can minimize spectral overlap is required. Since Ca^{2+} indicators themselves also act as Ca^{2+} buffers and can therefore impact both the levels and the kinetics of Ca^{2+}-signalling within cells, the strength and speed of Ca^{2+} indicators binding to Ca^{2+} should be considered. For accurate calibration of Ca^{2+} levels, high-affinity Ca^{2+} indicators are required.

According to previous studies, Ca^{2+} signalling is crucial in plenty of cellular processes [2, 3], including cell proliferation, cell migration, metastasis, and confers apoptosis resistance, which are key malignancy hallmarks in cancers (Figure 2). Generally, these functions are usually achieved in cancers via nuanced regulation of tumorigenic pathways by Ca^{2+}, frequently through spatially and/or temporally defined changes in Ca^{2+} [3].

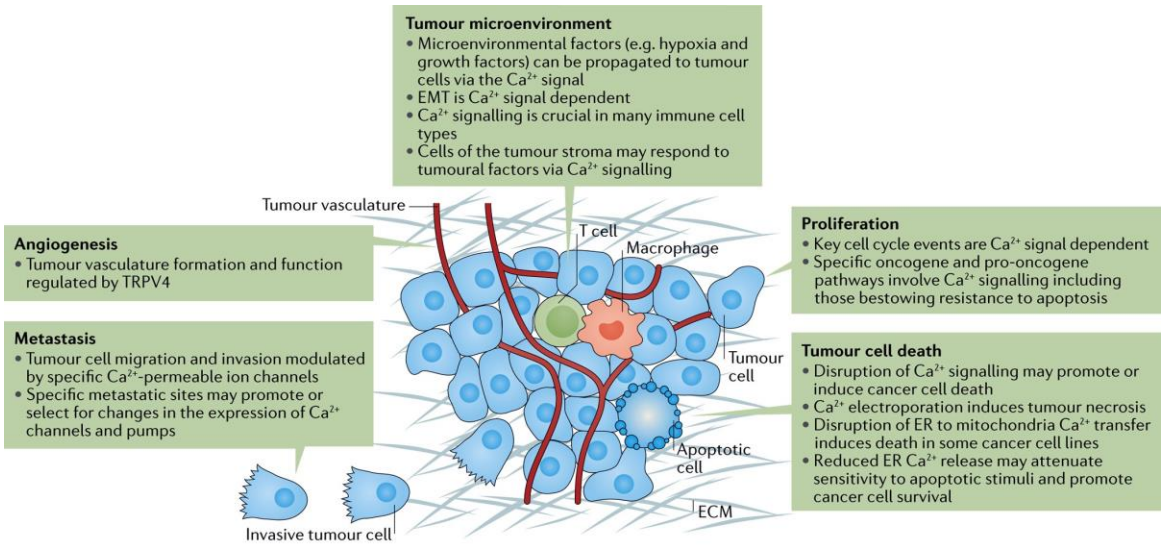

Figure 2. The Ca^{2+} signal and tumour progression [3]. The Ca^{2+} signal often intersects through specific Ca^{2+}-permeable ion channels and Ca^{2+} pumps, with various processes relevant to the growth, metastasis and death of cancer cells. ECM, extracellular matrix; EMT, epithelial to mesenchymal transition; ER, endoplasmic reticulum; TRP, transient receptor potential.

2.2.1 The relation between Ca^{2+} signalling and cell migration

Unlike other aggressive cancers that metastasize to organs through the circulatory system or lymphatic system, GBM cells rarely metastasize outside of the brain and instead actively migrate through the perivascular space around blood vessels and the space between neurons and glial cells [9]. In order to invade through these spaces, GBM cells alter the cell shape and volume to fit differently sized spaces and interact with the extracellular matrix to gain mobility [52, 53]. While the focal, adhesion molecules and cell morphology [54, 55], which are critical factors of cell migration, are maintained by Ca^{2+} signals. Tsai's group [56] showed that cells usually maintain a Ca^{2+} gradient with lower basal Ca^{2+} levels in the front to prevent persistent myosin light chain kinase (MLCK) activation. When cells migrate, local Ca^{2+} pulses near the front of migrating cells dynamically regulate MLCK and the retraction and adhesion of lamellipodia. BTP2 [57], a store-operated Ca^{2+} (SOC) influx pathway inhibitor, decreases local

Ca^{2+} pulses and focal adhesions, and the effect is similar to that caused by the myosin II inhibitor blebbistatin. Rac1 has been proved to promote GBM cells progression by regulating cell adhesion formation [58], and depletion/inhibition of Rac1 in GBM cells disrupted the disassembly of cell adhesion concomitant with defects in the actin web and switched the proportion of stable cell adhesion complex, thus reduced cell motility. Stimulation of VCAM-1 leads to the mobilization of intracellular Ca^{2+} and Rac1 activation, which are required for the activation of NADPH oxidase that induces actin restructuring for endothelial cell shape changes, and all these activities can be blocked by a Ca^{2+} channel inhibitor or a Ca^{2+} chelator [59]—confirming that Ca^{2+} can regulate cell migration via Rac1.

All these results demonstrate the fact that Ca^{2+} regulates cell migration. However, the effect of adhesion on cell motility depends on the cell types, and strong cell-matrix adhesion can impede cell motility. Therefore, increased cell-matrix adhesion might have contrasting effects on cell migration in weakly adherent cell types than strongly adherent cell types. In MDA-MB-468 breast cancer cells [60], Ca^{2+} homeostasis is different between the more epithelial and the more mesenchymal cell phenotypes. Epithelial to mesenchymal transition (EMT) occurs with attenuation of both SOC influx and ATP-mediated $[Ca^{2+}]_i$ changes. Actually, during cancer cell migration and invasion, the contribution of Ca^{2+} channels and pumps to Ca^{2+} changes could vary between different cancer types with the nature of stimulation.

Researches on cell migration using flat, 2D tissue culture surfaces have elucidated detailed molecular and biophysical mechanisms of cultured cells. In fact, most cells migrating through tissues undergo 3D migration, meaning that while migrating, they are continuously embedded in an extracellular matrix (ECM) environment. In this case, cell migration differs between in vivo and in vitro, potentially due to the more complex cell interactions in 3D [61]. To overcome this limitation, researchers created 3D cell culture. A well-designed microenvironment

in tissue and cell engineering can be used to mimic in vivo conditions and study cell migration in a more proper way.

2.2.2 The relation between Ca^{2+} signalling and cell proliferation

When extracellular Ca^{2+} is lowered from 1 mM to 0.1 mM, cell proliferation ceases [62]. Mammalian cells required Ca^{2+} during at least two distinct points, in early G1 and close to the G1/S boundary [63]. Besides, Ca^{2+} oscillations can be detected at the G2/M transition [64], suggesting that Ca^{2+} signalling plays an essential role in cellular proliferation and cell cycle by regulating the G1/S and G2/M transitions. Cells are most sensitive to depletion of extracellular Ca^{2+} in G1 [65], in which Ca^{2+} regulates the expression of immediate-early genes, such as FOS, JUN and MYC, and later towards the G1/S boundary where Ca^{2+} is required for retinoblastoma protein (Rb) phosphorylation [65]. Cyclin D1 and cyclin E1, members of cell cycle proteins, are essential regulators of the G1/S transition. Cyclin D1 forms an active complex with its interacting partner cyclin-dependent kinase 4 (CDK4). This cyclin D1/CDK4 complex can phosphorylate the Rb to disable their function as transcriptional suppressors and allows activation of E2F-dependent transcription to promote S phase entry and transcriptional activation of genes that control cell cycle progression [66, 67]. Moreover, cyclin E1 regulates the G1/S transition by activating CDK2 [68]. Their timing expression plays a direct role in DNA replication initiation [69], the control of histone biosynthesis [70], and the centrosome cycle [71]. It has been reported that downregulation of Piezo1 considerably suppressed Ca^{2+} signal increments, inhibited the phosphorylation of Akt and mTOR and arrested the cell cycle of prostate cancer cells at G0/G1 phase by inhibiting the activation of CDK4 and cyclin D1 [72]. Choi [73] and colleagues showed that a coordinate elevation in the intracellular free Ca^{2+} concentration is required for G1 to S phase cell cycle progression, and later they identified a CaM-binding site on cyclin E1, which supports a direct role for CaM in mediating Ca^{2+}-sensitive cyclin E/CDK2 activity and G1 to S phase transitions in VSMC.

In some cancer cells, Ca^{2+} channels or pumps altered [74], affecting the resting Ca^{2+} level in the cellular compartments and can change the spatial and temporal characteristics of the intracellular calcium transients. The proliferation of cancer cells can be suppressed by reducing or increasing the expression of specific Ca^{2+} channels or pumps. A tissue microarray analysis of breast tumours [75] showed that the expression level of plasma membrane Ca^{2+}-transporting ATPase 2 (PMCA2) is positive correlated with human epidermal growth factor receptor 2 (HER2) positivity, which mediates cell growth, and knocking down PMCA2 decreased breast cancer cell proliferation and increased the sensitivity to doxorubicin treatment. It has been reported that proliferation of breast, colorectal, gastric and prostate cancer cells requires T-type Ca^{2+} channels [74]. Based on the above background, targeting Ca^{2+} related channels or pumps may point the way to suppress GBM proliferation.

2.2.3 The relation between Ca^{2+} signalling and cell death

The magnitude, the spatial and temporal characteristics of Ca^{2+} signals are variable during cell processes. Sustained and large increases in $[Ca^{2+}]_i$ can be associated with cell death [76]. The ER and mitochondria are crucial stores where intracellular Ca^{2+} fluxes are governed and control many processes essential for life. However, Ca^{2+} arising from them can be a potent death-inducing signal [74]. Usually, 1,4,5-triphosphate (IP3) triggers the release of Ca^{2+} from these intracellular stores, which creates microdomains of high Ca^{2+} concentration between the ER and the mitochondria and accelerates Ca^{2+} in the mitochondrial network (Figure 3 left panel). Ca^{2+}-accelerated in mitochondria generates reactive oxygen species (ROS), which can damage DNA, promote Ca^{2+}-induced permeability transition pore opening, inhibit respiration and peroxide cardiolipin, causing it to dissociate from cytochrome c, which then exits the mitochondria to activate the intrinsic apoptotic pathway [77]. The increase of $[Ca^{2+}]_i$ can also activate calpain and promote proteolysis of BCL2, mitochondrial permeabilization and cytochrome c release, resulting in cell death.

Tumour cells should take advantage of the Ca^{2+} signalling to promote proliferation, meanwhile, protect itself from apoptosis. In U87 GBM cell lines [78, 79], which show loss of PTEN and augmented PKB activity, exhibit increased PKB-dependent phosphorylation of $InsP_3Rs$, decreased flux of Ca^{2+} from the ER to the mitochondria and decreased apoptosis (as shown in Figure 3 right panel). BCL2 has been reported to reduce ER Ca^{2+} by inhibition of SERCA2, decrease the sensitivity of the mitochondrial uptake process, and increase the capacity to accumulate Ca^{2+}. In fact, cancer cells usually exhibit upregulation of anti-apoptotic proteins of BCL2 (Figure 3), which can inhibit cell apoptosis by modulating intracellular Ca^{2+} signals [80]. In recent research, Osswald and coworkers [81] established that the adjacent tumour cells are linked by tumour microtubes (TMs) and form a network in brain tumours. The connecting cells can propagate Ca^{2+} to adjacent cells and share deleterious stimuli through TMs. So cells in the network can survive when suffering huge increases in Ca^{2+}, which would, if not dissipated, kill single isolated cells.

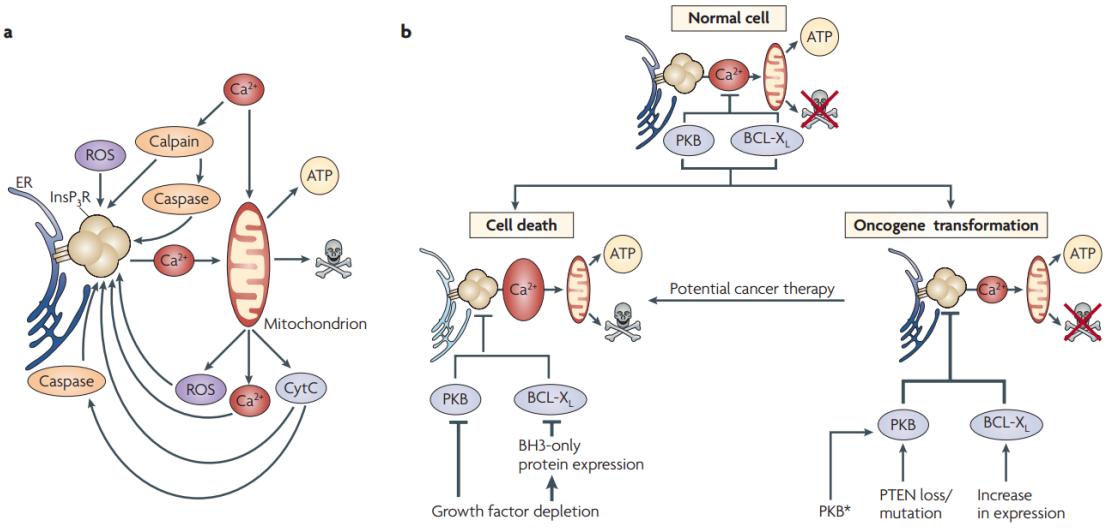

Figure 3. Apoptotic signals that induce endoplasmic reticulum (ER)–mitochondrial Ca^{2+} flux and their remodeling during cancer [74]. a, The transfer of Ca^{2+} from the ER to the mitochondria is a potent signal for death. A conduit for this Ca^{2+} transfer from the ER is the inositol 1,4,5-trisphosphate receptor ($InsP_3R$). $InsP_3Rs$ are sensitized by phosphorylation

(cell division cycle 2 (CDC2)–cyclin B), reactive oxygen species (ROS) and Ca^{2+}. $InsP_3Rs$ are deregulated by caspase, calpain cleavage and/or binding of cytochrome c (CytC). As mitochondria release many of these $InsP_3Rs$ regulatory factors, a feedforward loop is set up to amplify death signalling. b, Suppression of $InsP_3R$–mitochondrial Ca^{2+} flux during cancer. In naturally dividing cells experiencing normal levels of growth factor stimulation, $InsP_3Rs$ are tonically inhibited as a result of protein kinase B (PKB) phosphorylation and/or binding of BCL-XL. Reduction of growth factors or cell stress causes decreased PKB activity and the induction of BH3 (BCL2 homology 3)-only proteins. As a result, $InsP_3Rs$ are no longer phosphorylated by PKB and the interaction with BCL-XL is lost. Under these conditions, Ca^{2+} flux to the mitochondria is enhanced and cell death ensues. During cancer, BCL-XL expression and/or PKB expression and/or activity are increased, resulting in greater inhibition of $InsP_3R$ activity and mitochondrial Ca^{2+} accumulation. Thus, cell death is prevented and oncogenesis progresses. Reversing the remodelling that occurs during cancer to suppress Ca^{2+} flux to the mitochondria might be a therapeutic opportunity. Indeed, this might be achieved with BH3 mimetics or PKB inhibitors.

2.3 The MCU complex in cancer

Mitochondrial Ca^{2+} uptake can shape the amplitude and spatio-temporal patterns of Ca^{2+} signals [4] and regulate cell process. Mitochondrial Ca^{2+} uniporter (MCU), identified as a 40 kDa protein, locates in the inner mitochondrial membrane and regulates mitochondrial Ca^{2+} uptake. Hamilton and co-workers find that the genetic ablation of MCU decreases mitochondrial Ca^{2+} uptake in brain mitochondria [82].

2.3.1 The structure of the MCU complex

In mammals, the MCU complex contains four core components shown in Figure 4: the pore-forming MCU protein, the gatekeepers MICU1 and MICU2, and an essential regulatory subunit EMRE [4, 83, 84]. MCU is quiescent in resting $[Ca^{2+}]_i$ level (~100 nM) and becomes activated only when local Ca^{2+} levels rise to 1 μM. MICU1 and MICU2 sense changes of $[Ca^{2+}]_i$ to switch MCU on and off and avoid detrimental Ca^{2+} overload [85, 86].

In low-Ca^{2+} condition, the MCU complex is quiescent, and its structure reveals a 4:4:1:1 stoichiometry of MCU, EMRE, MICU1 and MICU2 (Figure 4). MCU tetramerizes to form a Ca^{2+}-conducting pore with EMREs attached to its periphery around a central approximate fourfold symmetry axis. MICU1 forms an extensive interacting surface with MCU to seal the pore's intermembrane space entrance, while MICU2 binds to MICU1 from the side without contacting MCU (Figure 4).

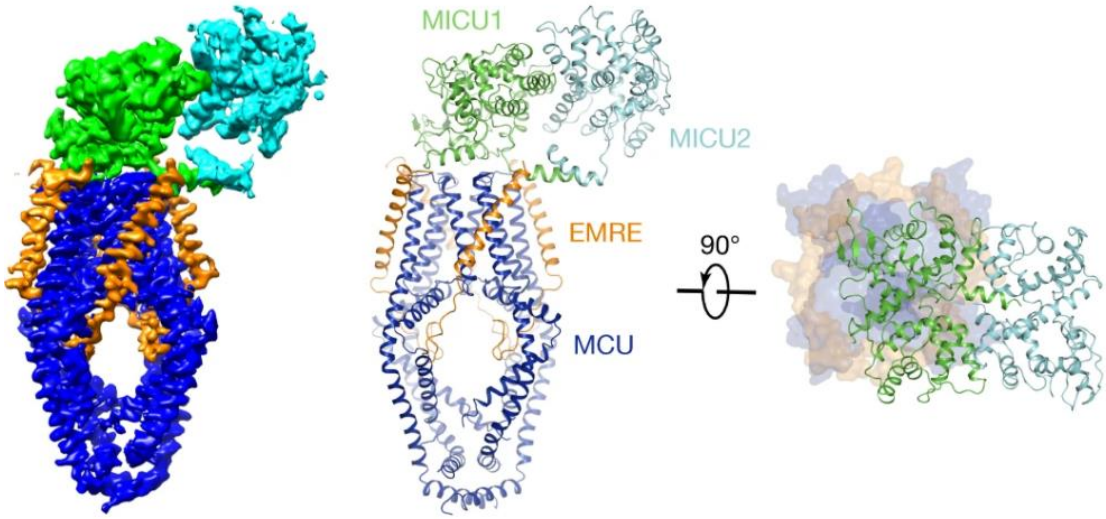

Figure 4. Architecture of the human MCU complex in low-Ca^{2+} conditions [83]. The cryo-EM map (left) and ribbon representation (middle) are viewed from the membrane. On the right, the uniplex (with MCU–EMRE shown as a surface representation and MICU1–MICU2 as a ribbon) is viewed from the top.

When Ca^{2+} activates the channel, the top of the MCU–EMRE tetramers moves closer with two MICU1–MICU2 heterodimers arching over it. But MICU1 no longer covers the pore in high Ca^{2+}; instead, it moves to the edge of the MCU–EMRE tetramer, losing most of its interactions with MCU (Figure 5), suggesting that Ca^{2+} activates the uniporter by removing MICU1 from the MCU surface to open the pore.

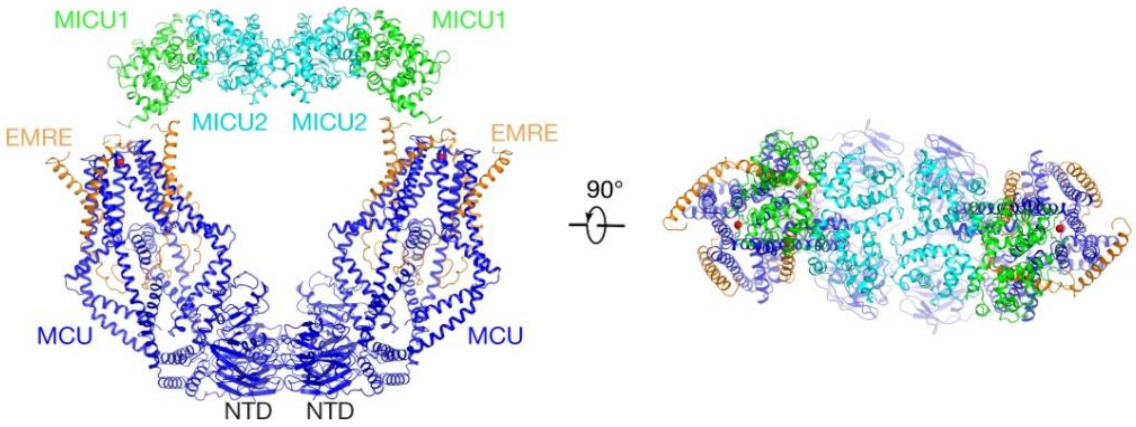

Figure 5. Architecture of the human MCU complex in high-Ca^{2+} conditions [83]. Red spheres represent Ca^{2+}.

2.3.2 The relation between MCU and cancer

MCU dysregulation is believed to be closely related to tumorigenesis. According to The Human Protein Atlas (www.proteinatlas.org), moderate to strong MCU immunoreactivity was shown in a majority of cancer tissues. The most robust protein expression was found in colorectal and ovarian cancers; high MCU expression was also detected in many other cancers, such as pancreatic, stomach, and prostate cancer. Moreover, in The Cancer Genome Atlas (TCGA; www.cancergenome.nih.gov), gene amplification of MCU was found in prostate cancer as well as breast cancers. According to datasets, MCU gene deletions were shown in malignant peripheral nerve sheath tumours (MPNST), and the highest rate of MCU mutation was observed in uterine carcinosarcoma. Tosatto

and co-workers [87] studied the role of MCU in triple-negative breast cancer (TNBC) migration and invasion and confirmed that MCU expression is correlated with tumour size and lymph node infiltration. In contrast, MCU knockdown decreased cell motility and invasion potential, as well as tumour growth in xenograft models of TNBC. However, Marchi and colleagues [88] suggested that microRNA-25 targets MCU and reduces the sensitivity of colon and prostate cancer cells to apoptosis-inducing agents through MCU downregulation.

Based on the researches of different tumour types, MCU shows complex and changeable characters (Table 1). The mechanisms of the MCU complex genetic modifications affect cancer biology and why their patterns differ across cancer types are not well understood yet, and more efforts still need to be paid in the future.

Table 1. Summary of publications featuring MCU in cancer [89].

Cancer type	Highlights
Breast cancer [90]	MCU promotes metastasis via Warburg effect; MCU is a direct target of microRNA-340; MCU expression is higher in metastatic breast cancer patients.
Triple negative Breast cancer [87]	MCU correlates with tumour size and lymph node infiltration; MCU knockdown (KD) reduces motility and invasion, tumour growth, lymph node infiltration, and lung metastasis in TNBC xenografts; MCU controls mROS and HIF-1α.
Breast and colon cancer cell lines [91]	IP_3R-mediated release of Ca^{2+} from ER and MCU-mediated mCa^{2+} influx is needed for celastrol-induced paraptosis in cancer cells.
Hepatocellular carcinoma [92]	MCU expression correlates with metastasis and poor prognosis; High MCU levels increase mCa^{2+} uptake and promote

	mROS via NAD+/SIRT3/SOD2 pathway; High MCU levels promote MMP2, cell motility, and intrahepatic and distal lung metastasis in vivo.
Pancreatic cancer [93]	HINT2 triggers cancer cell death via MCU; HINT2 overexpression is associated with MICU1 and MICU2 downregulation and EMRE upregulation.
Head and neck squamous cell carcinoma (HNSCC)[94]	EZH2 is a negative prognostic factor; its inhibition in vitro causes cell death and cell cycle arrest; EZH2 inhibition causes MICU1 downregulation; EZH2 and MICU1 are required to maintain mitochondrial membrane potential.
Multiple myeloma [95]	CYPD, SOD2, and MCU are differentially expressed in KMS cells and control mitochondrial activity and bortezomib sensitivity; Membrane potential, oxygen consumption rate, ATP, and mCa^{2+} concentrations correlate with KMS drug resistance.
$p53^{-/-}$ MEFs; HCT-116; HeLa; H1299 [96]	Links p53 to Ca^{2+} signaling in cell death regulation In vivo Ca^{2+} imaging in 3D tumour masses and photodynamic stress reveal high mCa^{2+} as a cause of p53-dependent cell death.
MDA-MD-468 (breast cancer) HeLa and EA.hy926 cells [97]	ER-mitochondria tethering increases cancer cells sensitivity to resveratrol/piceatannol; MCU and LETM1 control mCa^{2+} uptake; MCU and LETM1 control resveratrol/piceatannol-induced cancer cell death.
Oncogene-induced senescence in HEC cells [98]	MCU loss enables escape from oncogene-induced senescence.
Prostate cancer [99]	Mitochondrial swelling induced by metformin is due to enhanced mCa^{2+} and is reversed by MCU inhibition.
Melanoma [100]	Drug resistant and tumour maintaining melanoma cells display elevated mCa^{2+}.

Melanoma and osteosarcoma [101]	Ca^{2+} protects osteosarcoma and melanoma cells from tumour necrosis factor (TNF)-related apoptosis-inducing ligand (TRAIL) cytotoxicity; Ca^{2+} chelators and the MCU inhibitor ruthenium 360 decrease mCa^{2+} and sensitize tumour cells to TRAIL cytotoxicity.

The expression level of MCU in the brain, especially in the cerebral cortex, is high. Nonetheless, MCU is highly expressed in GBM stem cells (GSC), embryonic stem cell lines (ESC) and GBM cell lines, compared with that in normal brain tissues [5]. However, the exact function of MCU in GBM cells has not yet been fully described or understood. During my PhD, I am committed to studying the relation between Ca^{2+} signals, the MCU complex and the hallmarks, proliferation and migration, in GBM cells.

3. Results

This section is about papers published and papers in preparation during my PhD. My collaborators and I finished them under the supervision of Prof. Vincent Torre and his collaborators. In detail:

- In the first article published in Journal of Cell Science, I set the cell culture protocol, performed the live-cell imaging, calcium imaging, ratiometric calcium imaging, prepared the samples for Western Blot and FACS analysis, and analysed the data. I prepared the figures and wrote the manuscript with all the authors.

- In the second article published in Advanced Materials, I set the glioma-cortex co-culture protocol, performed the live-cell imaging experiment, and participated in data analysis and figure preparation. I wrote the manuscript with all the authors.

- In the third article in preparation, I set the cell culture protocol, performed the live-cell imaging, transwell assay. I analysed the data and prepared the figures. I wrote the manuscript with all the authors.

I actively participate and have a major contribution to all these works.

3.1 Mechanisms of malignancy in glioblastoma cells are linked to mitochondrial Ca^{2+} uniporter upregulation and higher intracellular Ca^{2+} levels

Li X., Spelat R., Bartolini A., Cesselli D., Ius T., Skrap M., Caponnetto F., Manini I., Yang Y., Torre V.

Journal of Cell Science

© 2020. Published by The Company of Biologists Ltd | Journal of Cell Science (2020) 133, jcs237503. doi:10.1242/jcs.237503

RESEARCH ARTICLE

Mechanisms of malignancy in glioblastoma cells are linked to mitochondrial Ca^{2+} uniporter upregulation and higher intracellular Ca^{2+} levels

Xiaoyun Li[1], Renza Spelat[1], Anna Bartolini[2], Daniela Cesselli[2,3], Tamara Ius[4], Miran Skrap[4], Federica Caponnetto[3], Ivana Manini[3], Yili Yang[5] and Vincent Torre[1,5,*]

ABSTRACT

Glioblastoma (GBM) is one of the most malignant brain tumours and, despite advances in treatment modalities, it remains largely incurable. Ca^{2+} regulation and dynamics play crucial roles in different aspects of cancer, but they have never been investigated in detail in GBM. Here, we report that spontaneous Ca^{2+} waves in GBM cells cause unusual intracellular Ca^{2+} ($[Ca^{2+}]_i$) elevations (>1 µM), often propagating through tumour microtubes (TMs) connecting adjacent cells. This unusual $[Ca^{2+}]_i$ elevation is not associated with the induction of cell death and is concomitant with overexpression of mitochondrial Ca^{2+} uniporter (MCU). We show that *MCU* silencing decreases proliferation and alters $[Ca^{2+}]_i$ dynamics in U87 GBM cells, while *MCU* overexpression increases $[Ca^{2+}]_i$ elevation in human astrocytes (HAs). These results suggest that changes in the expression level of MCU, a protein involved in intracellular Ca^{2+} regulation, influences GBM cell proliferation, contributing to GBM malignancy.

This article has an associated First Person interview with the first author of the paper.

KEY WORDS: MCU, Ca^{2+} waves, Glioblastoma, Malignancy

INTRODUCTION

When primary glioblastoma (GBM; World Health Organization grade IV glioma) cells derived from patients are implanted in mouse brains, long and thin membrane protrusions originating from the cell body of the GBM cells are observed (Osswald et al., 2015). These thin protrusions, which can be as long as hundreds of microns and connect tumour cells in a multicellular network, are referred to as tumour microtubes (TMs). TMs have two features possibly contributing to GBM malignancy: they provide a way for GBM to invade and infiltrate, and they form one large syncytium that confers to the cellular network resistance to radiotherapy (Osswald et al., 2015; Osuka and Van Meir, 2017). Oncotherapy, based on either radiotherapy or chemotherapy, is usually associated with increased intracellular Ca^{2+} ($[Ca^{2+}]_i$) (McFerrin et al., 2012; Tombal et al., 2002), and the control of $[Ca^{2+}]_i$ plays major roles in healthy and cancerous cells. Indeed, when $[Ca^{2+}]_i$ is elevated to micromolar levels, cells usually undergo apoptosis within 6 h (Tombal et al., 2002). The unusual resistance of GBM cells to oncotherapy has been attributed to the ability of TMs to facilitate Ca^{2+} fluxes among different GBM cells, leading to the distribution of $[Ca^{2+}]_i$ away from damaged cells to all the other cells connected to it by the TMs. However, it is possible that GBM cells also have an intrinsic resistance – originating from their altered genomic landscape – to the elevation of $[Ca^{2+}]_i$, as we argue in the present paper.

Mitochondria accumulate large amounts of Ca^{2+} and contribute to the maintenance of a low resting $[Ca^{2+}]_i$ (Foskett and Philipson, 2015): if $[Ca^{2+}]_i$ exceeds a threshold in the micromolar range, cells trigger metabolic pathways leading to cell death (Liu et al., 2015). Ca^{2+} influx into mitochondria is mediated by mitochondrial Ca^{2+} uniporter (MCU), and genetic ablation of *Mcu* decreases mitochondrial Ca^{2+} uptake (Hamilton et al., 2018), while persistent MCU activity enhances mitochondrial Ca^{2+} uptake (Dong et al., 2017). It has been proposed that cancer stem cells share several properties of adult neural stem cells, in particular altered Ca^{2+} regulation (Leclerc et al., 2016). On the basis of a bioinformatics analysis, several genes involved in Ca^{2+} regulation with altered expression in GBM cells have been identified, among which *MCU* has been found to be overexpressed (Robil et al., 2015). There is now considerable evidence suggesting crucial roles for MCU and its regulators in cancer (Mammucari et al., 2017), but the exact function of MCU in GBM cells has not yet been fully described or understood.

To perform measurements of Ca^{2+} dynamics and $[Ca^{2+}]_i$, we looked for U87 GBM cells connected by TMs in a single layer (Fig. 1A), in which Ca^{2+} measurements are feasible and reliable. We also observed TMs in cultures of the U251, T98G GBM cell lines and in glioblastoma stem cells (GSCs) from patients cultured in adhesion. We analysed Ca^{2+} transients in the somas and TMs of U87 cells using the fluorescent Ca^{2+} probe Fluo-4 AM and with ratiometric Ca^{2+} imaging using Fluo-4 AM and Fura Red AM, providing a quantitative measure of Ca^{2+} transients (Assinger et al., 2015). Our results show some unusual properties of Ca^{2+} dynamics in GBM cells: first, spontaneously occurring transients originating in the middle of TMs did not always propagate to the somas of connected cells, but large Ca^{2+} waves originating in the somas propagated along the TMs more easily; second, spontaneous Ca^{2+} transients in U87 cells and GSCs from patients could reach values up to 1–3 µM for long durations and not lead to cell death; and third, MCU, a protein involved in the influx of Ca^{2+} into the mitochondria, is overexpressed in GBM cells.

Our results suggest that the mitochondrial $[Ca^{2+}]$ overload after overexpression of *MCU*, causes large and unusual $[Ca^{2+}]_i$

[1]Neurobiology Sector, International School for Advanced Studies (SISSA), 34136 Trieste, Italy. [2]Institute of Pathology, University Hospital of Udine, 33100 Udine, Italy. [3]Department of Medicine, University of Udine, 33100 Udine, Italy. [4]Neurosurgery Unit, Department of Neurosciences, University Hospital of Udine, 33100 Udine, Italy. [5]Joint SISSA-ISM Laboratory, Suzhou Institute of Systems Medicine, Chinese Academy of Medical Sciences, 215000 Suzhou, Jiangsu, China.

*Author for correspondence (torre@sissa.it)

T.I., 0000-0003-3741-0639; I.M., 0000-0002-3319-7749; V.T., 0000-0001-8133-3584

Received 6 August 2019; Accepted 28 January 2020

Journal of Cell Science (2020) 133, jcs237503. doi:10.1242/jcs.237503

dynamics. Moreover, a higher MCU level in GBM cells promotes cell proliferation, which is an important factor contributing to GBM malignancy, possibly through activation of the Ca^{2+}-calmodulin complex and calmodulin-dependent protein kinase II (CaMKII) (Fischer et al., 2013), and specific transcription factors, such as members of the cAMP response element-binding protein (CREB) family (Shanmughapriya et al., 2015).

RESULTS

TMs connecting separated GBM cells

The proliferation and migration of cultured GBM cells were followed by live-cell imaging, in which an image was acquired every 1 or 2 min for several days. When GBM cells were imaged under bright-field illumination, thin structures connecting two GBM cells reminiscent of tumour TMs were detected (Fig. 2A). When GBM cells were either stained with the fluorescent membrane marker Vybrant™ DiD or labelled with the fluorescent probe mCherry, TMs were better visualized, and their dynamics could be followed for several hours (Fig. 2B,C).

Often, GBM cells retracted all their processes and assumed a rounded shape, which was followed by the emergence of two lobes, preceding cell division (Fig. 2D, 0 min). During mitosis, on several occasions, a thick structure with a width of several microns formed, and within tens of minutes, when the two GBM cells started to move apart, one to six TMs could be clearly seen (Fig. 2D, 10 min; Movie 1). The TMs formed in this way could be observed for several hours (Fig. 2D). In most cases, TMs formed during mitosis, but we occasionally also observed the formation of TMs following an encounter between two distinct U87 GBM cells (Fig. S1 and Movie 2). During such collisions, the two cells joined very closely, and following this apparent fusion, they separated again, leaving between them connecting TMs. This phenomenon – never observed in normal, healthy neurons – suggests a transient fusion of the cellular membrane of the two GBM cells.

We followed individual TMs for up to 5–6 h, and, at later times, the TMs were usually lost, either because of dye bleaching or because of disruption following the vigorous GBM cell motion. The mean duration of TM persistence in our experimental conditions was 67±7 min, and the TM lengths varied from a few microns to more than 100 µm (Fig. 2F), equivalent to approximately three times the diameter of the GBM cell body. Some TMs extended up to 100–200 µm following GBM cell motion, and some TMs persisted for several hours (Fig. 2E,F).

Ca^{2+} transients in GBM soma

U87 GBM cells were seeded on 15-mm coverslips at a density of 2.0×10^4 cells, and Ca^{2+} transients in their somas were analysed using the Ca^{2+} indicator Fluo-4 AM. GBM cells moved during the Ca^{2+}-imaging experiments, and often in 5–10 min, their somas could move by 1–3 µm. Therefore, we analysed Ca^{2+} dynamics only in cells that did not move during the experiment.

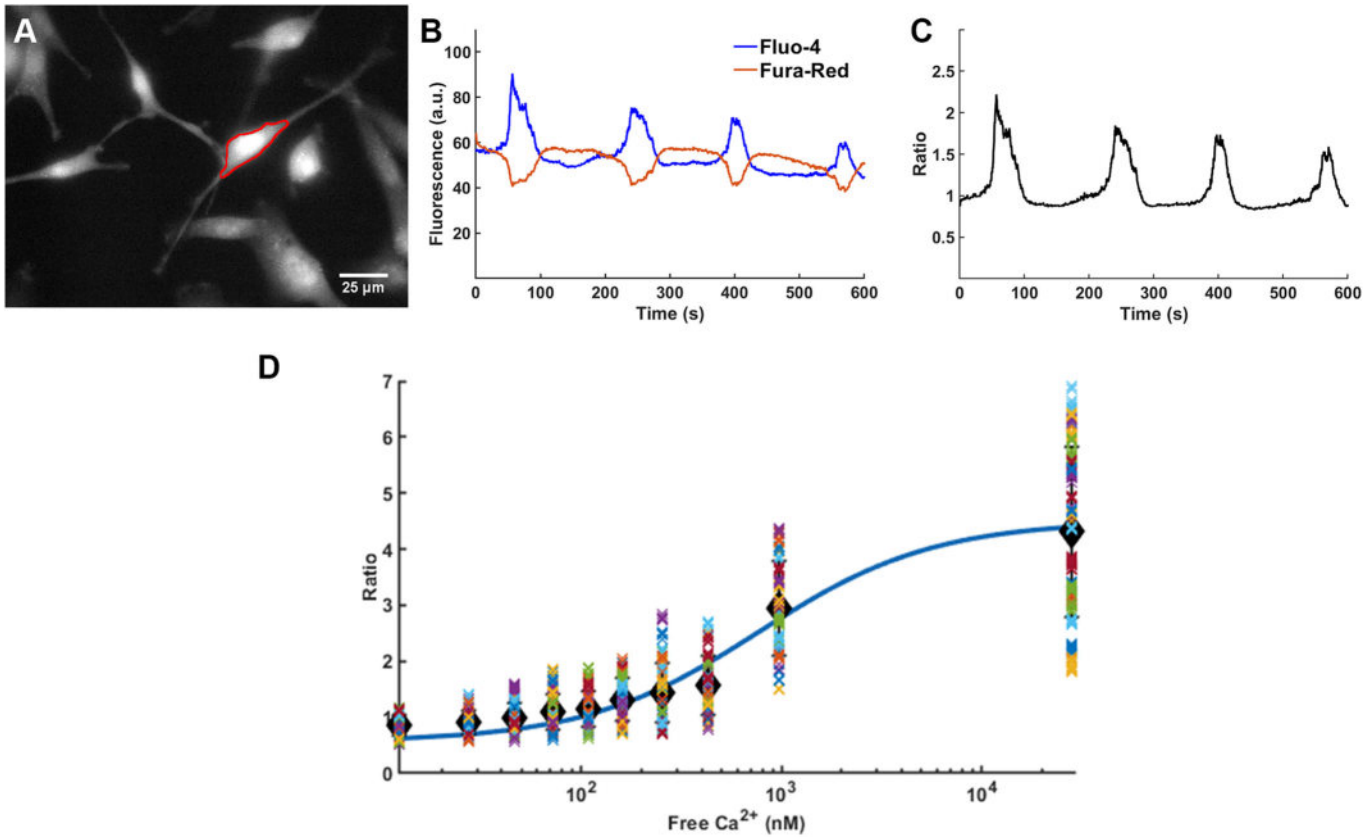

Fig. 1. Ca^{2+} calibration method. (A) U87 GBM cells transduced with mCherry. The red outlined area represents a typical region of interest (ROI) used to measure the emitted fluorescence in GBM cells loaded with Fluo-4 AM and Fura Red AM. (B) Time course of the emitted fluorescence by Fluo-4 AM (F1 blue line) and by Fura Red AM (F2 red line) from the ROI of A. The upward and downward signals indicate the optical recordings of the spontaneous Ca^{2+} transients. (C) The fluorescence ratio R obtained from the data shown in B. The amplitude of transients of R=F1/F2 is less affected by dye bleaching than in F1 and F2. (D) Estimation of the parameters used in Eqn 3 to obtain the value of $[Ca^{2+}]_i$ from R. Each coloured dot represents values from a single U87 GBM cell. Data are from 32 different GBM cells in three distinct experimental sessions, and the values obtained for K_d, R_{min} and R_{max} are 810.3 nM, 0.56 and 4.60, respectively.

Journal of Cell Science (2020) 133, jcs237503. doi:10.1242/jcs.237503

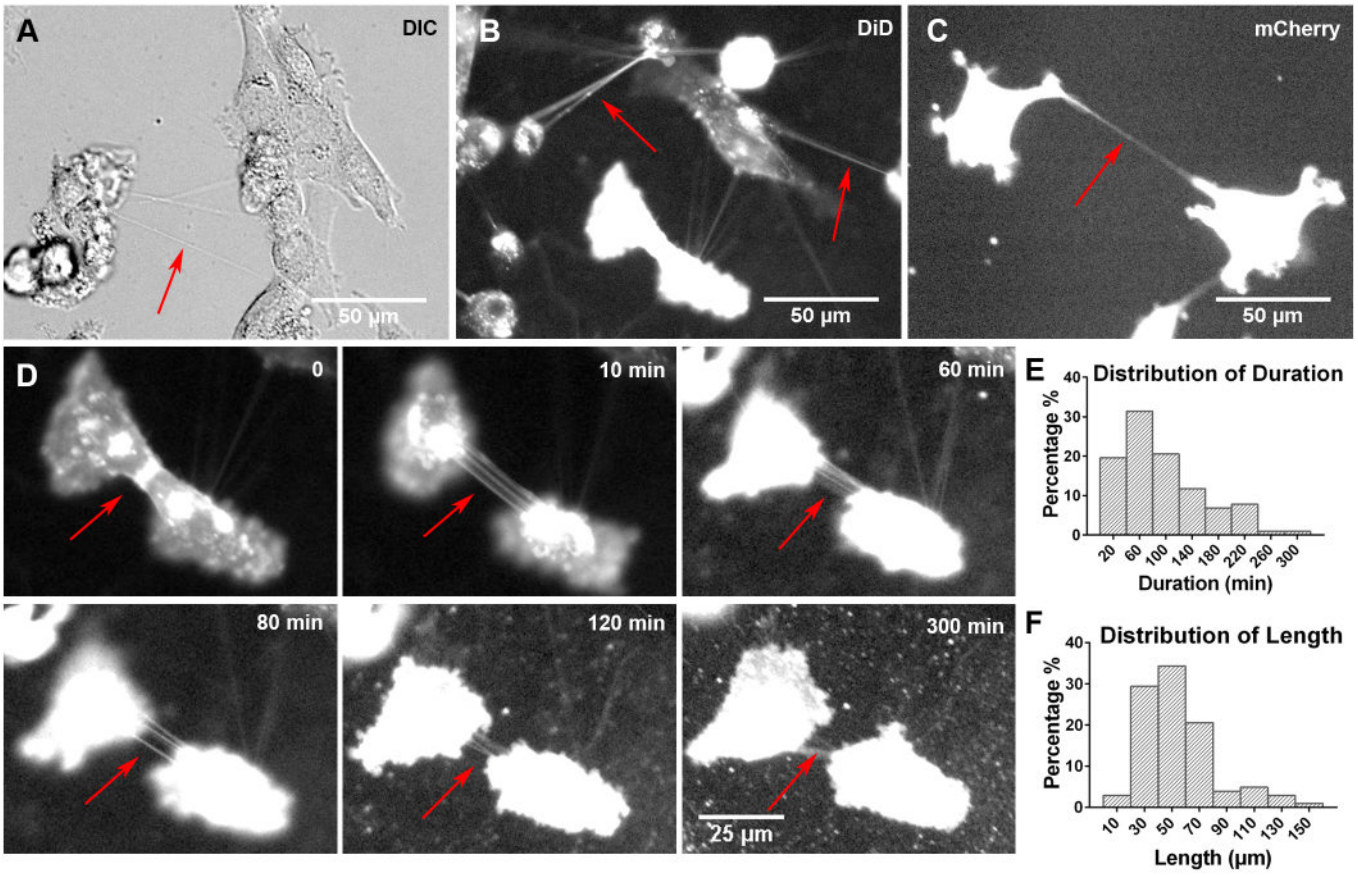

Fig. 2. Tumour microtubes (TMs) connect U87 GBM cells. (A) A differential interference contrast (DIC) image of U87 GBM cells. (B) Fluorescence image of U87 GBM cells stained with the fluorescent membrane marker Vybrant™ DiD. (C) Fluorescence image of U87 GBM cells labelled with mCherry. (D) A sequence of fluorescence images of U87 cells stained with Vybrant™ DiD undergoing mitosis. The red arrows in A–D point to TMs, which are more visible when stained by a fluorescent label. (E) Distribution of the durations of TMs. (F) Distribution of the lengths of TMs. The data in E and F were collected from 146 U87 GBM cells in three distinct experimental sessions.

During the first day of culture (Day 1), the great majority of U87 cells remained isolated, and only a small fraction of them was connected by TMs; only occasional Ca^{2+} transients could be detected (Fig. 3A). After culture for 2–3 days (Day 2 and Day 3), more cells had become connected by TMs and had formed a functional network. On Day 2 and Day 3, spontaneous Ca^{2+} waves with durations of ∼1 min could be detected; these waves were almost periodic but exhibited low synchrony (Fig. 3B,C). The amplitude of these optical signals was large, and the value of DF/F_0 could exceed 1 (Fig. 3B,C,E). After culture for 4 days (Day 4), the GBM cells had formed a morphologically connected dense layer, and only a few TMs could be detected; the Ca^{2+} transients had become shorter and weaker, with a DF/F_0 value less than 0.5 (Fig. 3D,E).

Ca^{2+} transients in TMs

As represented in Fig. 3E, the properties of the Ca^{2+} transients changed with time after the U87 GBM cells were moved into culture dishes: initially, the cells were isolated, with very few connecting TMs (Day 1), but the fraction of connected cells increased following proliferation (Day 2 and Day 3), and when tumour spheres started to form, the number of visible TMs dropped substantially (Day 4). Similarly, the amplitude and duration of the measured optical transients changed from Day 1 to Day 4 (Fig. 3E), and spontaneous Ca^{2+} waves had a larger amplitude on Day 2 and Day 3 than on Day 1 and Day 4, which suggests that the Ca^{2+} elevation was higher. For these reasons, Ca^{2+} transients were analysed in detail on Day 2 and Day 3.

In several cases, Ca^{2+} transients propagated with a delay varying from 1 to 10 s to a nearby cell, but with a reduced amplitude. In other cases, a small Ca^{2+} transient originating in a distal process was amplified and propagated to the soma. The propagation of Ca^{2+} transients between morphologically connected cells was not always bi-directional, especially in cells connected by TMs (Fig. 4A,C): we often observed the presence of spontaneous localized Ca^{2+} transients in TMs with stereotypical shapes and amplitudes (see orange shading in the red trace in Fig. 4B). However, these transients often did not propagate to the neighbouring portions of the same TM. These experiments were performed with the single Ca^{2+} indicator Fluo-4 AM, and, given the high motility of GBM cells and of the connecting TMs, localized optical transients could be caused by a small motion of the TM itself rather than by a genuine Ca^{2+} hotspot. Therefore, we moved to ratiometric Ca^{2+} imaging based on Fluo-4 AM and Fura Red AM (Assinger et al., 2015); in this method, an increase in $[Ca^{2+}]_i$ causes an increase in the fluorescence emitted by Fluo-4 AM but a decrease in the fluorescence emitted by Fura Red AM (Fig. 1B).

Using ratiometric Ca^{2+} imaging, we determined the complexity of Ca^{2+} propagation along TMs connecting the somas of two GBM cells. Large Ca^{2+} transients originating in the soma of one of the two

Journal of Cell Science (2020) 133, jcs237503. doi:10.1242/jcs.237503

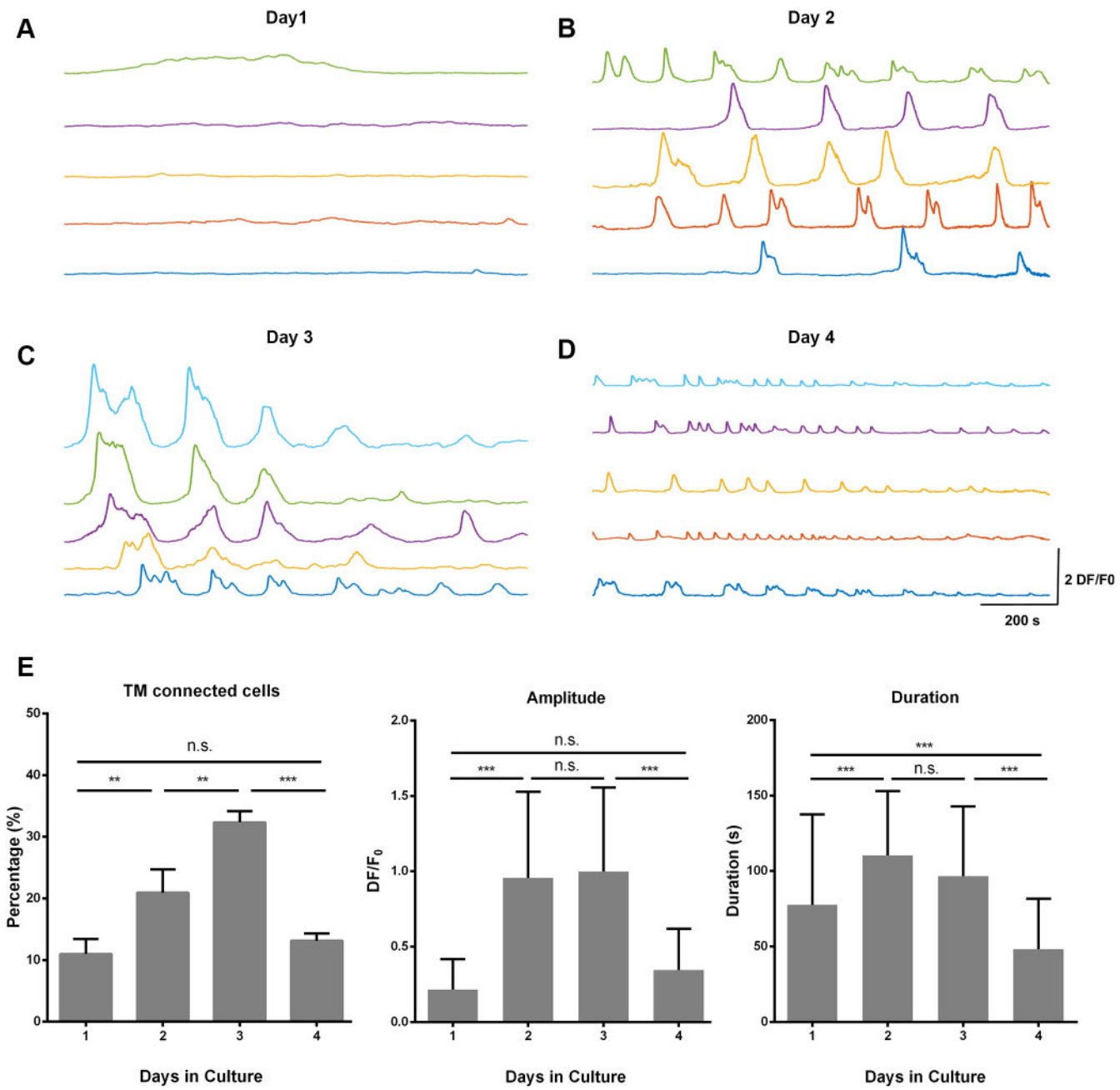

Fig. 3. Spontaneous Ca^{2+} transients in U87 cells. (A–D) Optical traces from U87 cells loaded with the Ca^{2+} indicator Fluo-4 AM after cultivation for 1 (A), 2 (B), 3 (C) and 4 (D) days. (E) Distribution of cells connected by TMs (left), amplitude of fluorescent signals during spontaneous optical transients (DF/F_0) (middle) and duration of optical transients (right) as a function of days in culture. The data in E were collected from 160 U87 GBM cells in three distinct experimental sessions. The duration of optical transients was measured as the time during which DF/F_0 was larger than 0.3 times the peak amplitude of the optical transient. $^{**}P<0.01$, $^{***}P<0.001$. n.s., not significant.

cells propagated along the TM (see the initial large increase in R in the red and blue traces in Fig. 4D). Frequently, following this conventional Ca^{2+} propagation, we observed a Ca^{2+} transient originating in the middle of the same TM that remained localized and did not propagate to the two ends of the TM (see optical transients in the blue trace within the orange shading in Fig. 4D). Similar observations obtained in the other seven TMs suggest that large Ca^{2+} transients originating in GBM cell somas are global events that can invade the entire cell and propagate along the TMs, but small Ca^{2+} transients originating in TMs do not easily propagate and represent localized hotspots.

The presence of Ca^{2+} hotspots along TMs could originate from the presence of local barriers preventing the free diffusion of Ca^{2+}. Barriers to free diffusion along TMs could be formed by mitochondria operating in these narrow structures (Bindocci et al., 2017). Therefore, we analysed the presence of mitochondria in the TMs (Fig. 4E) using the dye MitoTracker Red FM (Fig. 4F). We found clear spots of the dye in the middle of TMs, indicating the presence of mitochondria in restricted regions of TMs. These mitochondrial hotspots were also highly dynamic and could move along the TM with a velocity of ∼1 µm/min (compare the 0 min and 15 min images in Fig. 4F; Movie 3).

Journal of Cell Science (2020) 133, jcs237503. doi:10.1242/jcs.237503

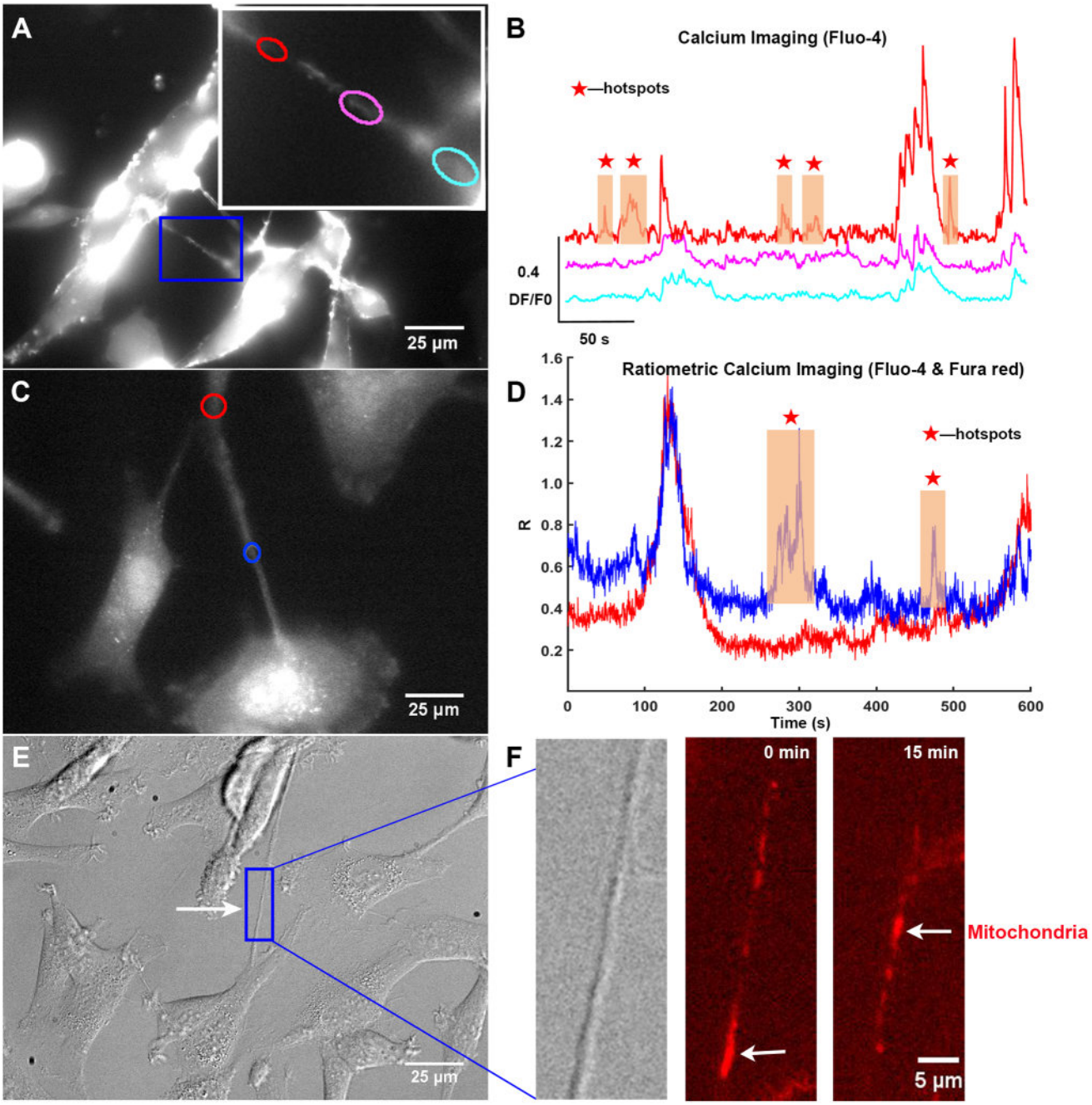

Fig. 4. Properties of Ca^{2+} transients in TMs. (A) Fluorescent image of U87 GBM cells loaded with Fluo-4 AM. (B) Optical transients (DF/F_0) from the three regions along the TM outlined in colours in A. The red stars indicate the localized optical signals that did not propagate along the TM. (C) As in A, but GBM cells were loaded with both Fluo-4 AM and Fura Red AM to perform ratiometric Ca^{2+} imaging. (D) Time course of R from the red and blue regions shown in C. The initial large optical signal propagated from the red to the blue region, while the optical transients shown in the orange boxes remained confined to the blue region in the middle of the TM. (E) DIC image of a TM connecting two U87 GBM cells, and TM is indicated by an arrow. (F) Magnified images of the staining of mitochondria labelled with MitoTracker Red FM, and mitochondria are indicated by arrows.

$[Ca^{2+}]_i$ transients reach higher levels in GBM cells than in human astrocytes (HAs)

The use of ratiometric Ca^{2+} imaging not only allows us to verify and rule out possible artefacts caused by cell motion but also enables quantitative estimation of increases in $[Ca^{2+}]_i$ (see Materials and Methods). We examined spontaneous Ca^{2+} waves in HAs (Fig. 5A), U87 cells (Fig. 5B) and GSCs from patients (Fig. 5C) when these cells had formed monolayers in the dishes (Day 2 and Day 3). We often observed global intermittent behaviour in these monolayers: large, synchronous Ca^{2+} transients appeared in most of the visualized cells, but at different times, the Ca^{2+} waves were completely asynchronous. This intermittency between a state with highly synchronous Ca^{2+} waves and a state with randomly occurring Ca^{2+} transients was typical of cells connected by TMs.

In healthy HAs, the spontaneous Ca^{2+} waves reached maximal values below 1 μM (pCa<6 and corresponding to values of R between 2.5 and 3). We never observed $[Ca^{2+}]_i$ elevations above 1 μM in HAs other than those triggering cell death. In U87 cells, the elevation of $[Ca^{2+}]_i$ was much more significant, and the value

Journal of Cell Science (2020) 133, jcs237503. doi:10.1242/jcs.237503

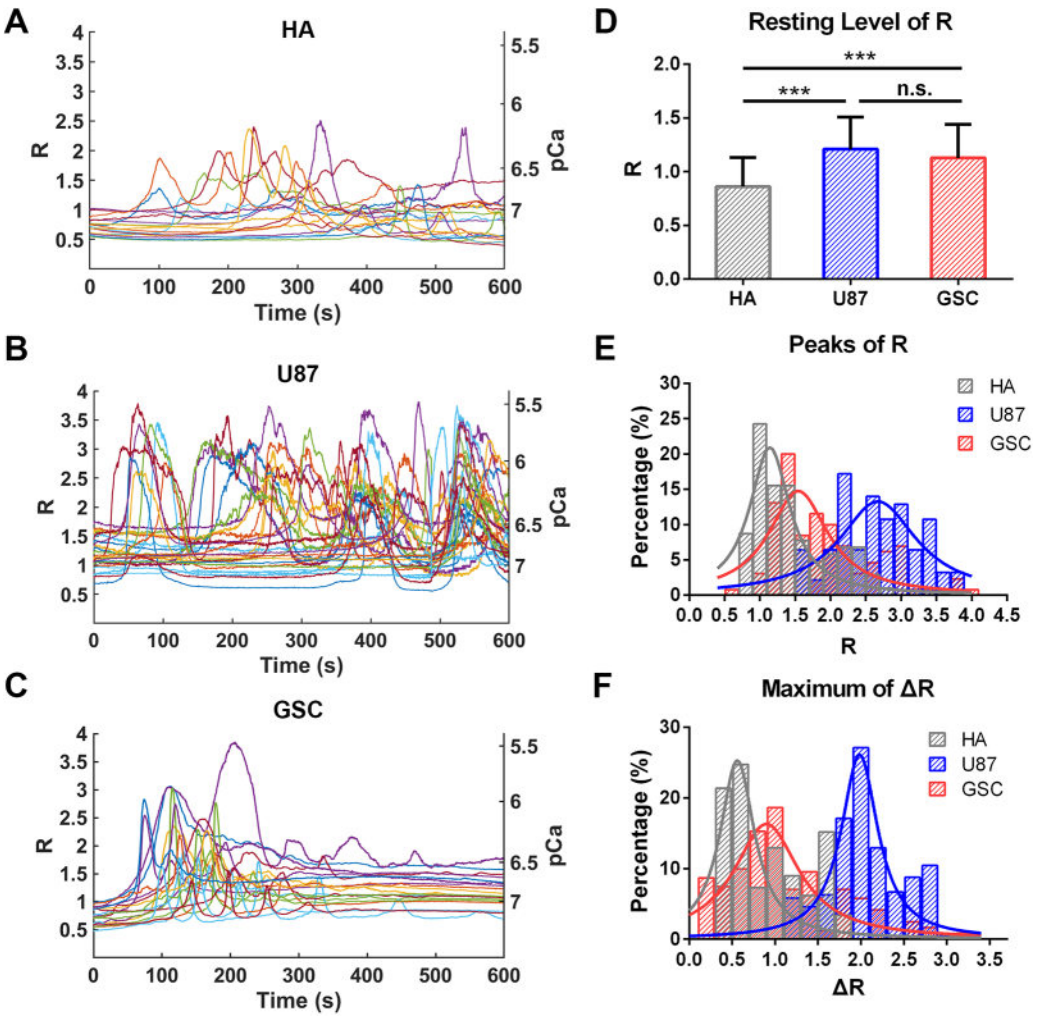

Fig. 5. Intracellular Ca^{2+} levels in HAs, U87 GBM cells and GSCs from patients. (A–C) Representative spontaneous intracellular Ca^{2+} waves measured with ratiometric Ca^{2+} imaging in HAs (A), U87 GBM cells (B) and GSCs from patients (C). (D) Average basal values of R in HAs, U87 GBM cells and GSCs. (E) Distribution of the peak values of R during spontaneous Ca^{2+} waves in HAs, U87 GBM cells and GSCs. (F) Distribution of ΔR during spontaneous Ca^{2+} waves in HAs, U87 GBM cells and GSCs. The data in D–F were collected from three distinct experimental sessions. In D, the data represent the mean±s.d. ***P<0.001. n.s., not significant.

of R could increase from values of ∼1 to 3.5 and occasionally close to 4 (Fig. 5B). On the basis of the calibration curve (see Fig. 1D), $[Ca^{2+}]_i$ increased to values exceeding 1 µM during the spontaneous Ca^{2+} waves. In GSCs from patients, we observed spontaneous Ca^{2+} waves reaching peak values above 1 µM, and often $[Ca^{2+}]_i$ remained elevated for several minutes (Fig. 5C). Following this unusual $[Ca^{2+}]_i$ elevation, a resting level of ∼100 nM was reached in several minutes without changes in morphology or motility.

Given the uncertainty in estimating the exact value of $[Ca^{2+}]_i$ from R, we compared changes in R and not in $[Ca^{2+}]_i$ in different cell types. The mean resting level of R was close to 1 in HAs and slightly greater in U87 cells and GSCs (Fig. 5D). The change in R (ΔR) and the maximal value of R at the peak of the spontaneous Ca^{2+} waves were significantly higher in U87 GBM cells than in HAs or GSCs (Fig. 5E,F). Both ΔR and the peak values of R were higher in GSCs than in HAs, but to a lesser extent. Based on these results, we conclude that $[Ca^{2+}]_i$ in U87 cells and in GSCs from patients can reach levels much higher than those in HAs without causing any signs of cell death.

Comparison of the expression of MCU in HAs, U87 GBM and GSCs

There are several indications that Ca^{2+} regulation and homeostasis are different in cancer cells than in normal healthy cells, particularly in glioma and GBM (Farfariello et al., 2015; Marchi and Pinton, 2016). Indeed, a recent bioinformatics analysis (Robil et al., 2015) identified higher levels of expression of several genes related to Ca^{2+}, which were collectively referred to as the Ca^{2+} toolbox, in cancer cells. This toolbox contains several tens of genes, some of which could be involved in helping GBM cells to sustain higher levels of $[Ca^{2+}]_i$ than those in other cells: a gene that is highly expressed in GBM cell lines but expressed at lower levels in normal brain tissues is *MCU*. In addition, some proteins of the S100 family of Ca^{2+}-binding proteins are overexpressed in brain tumours; namely, S100A2, S100A4, S100A8 and S100A11, and have been reported as markers of tumorigenicity (Rand et al., 2008). Therefore, we used western blotting and immunofluorescence to verify whether the overexpression of MCU could be responsible for the resistance and tolerance of GBM cells to unusual elevation of $[Ca^{2+}]_i$ (Fig. 6).

Journal of Cell Science (2020) 133, jcs237503. doi:10.1242/jcs.237503

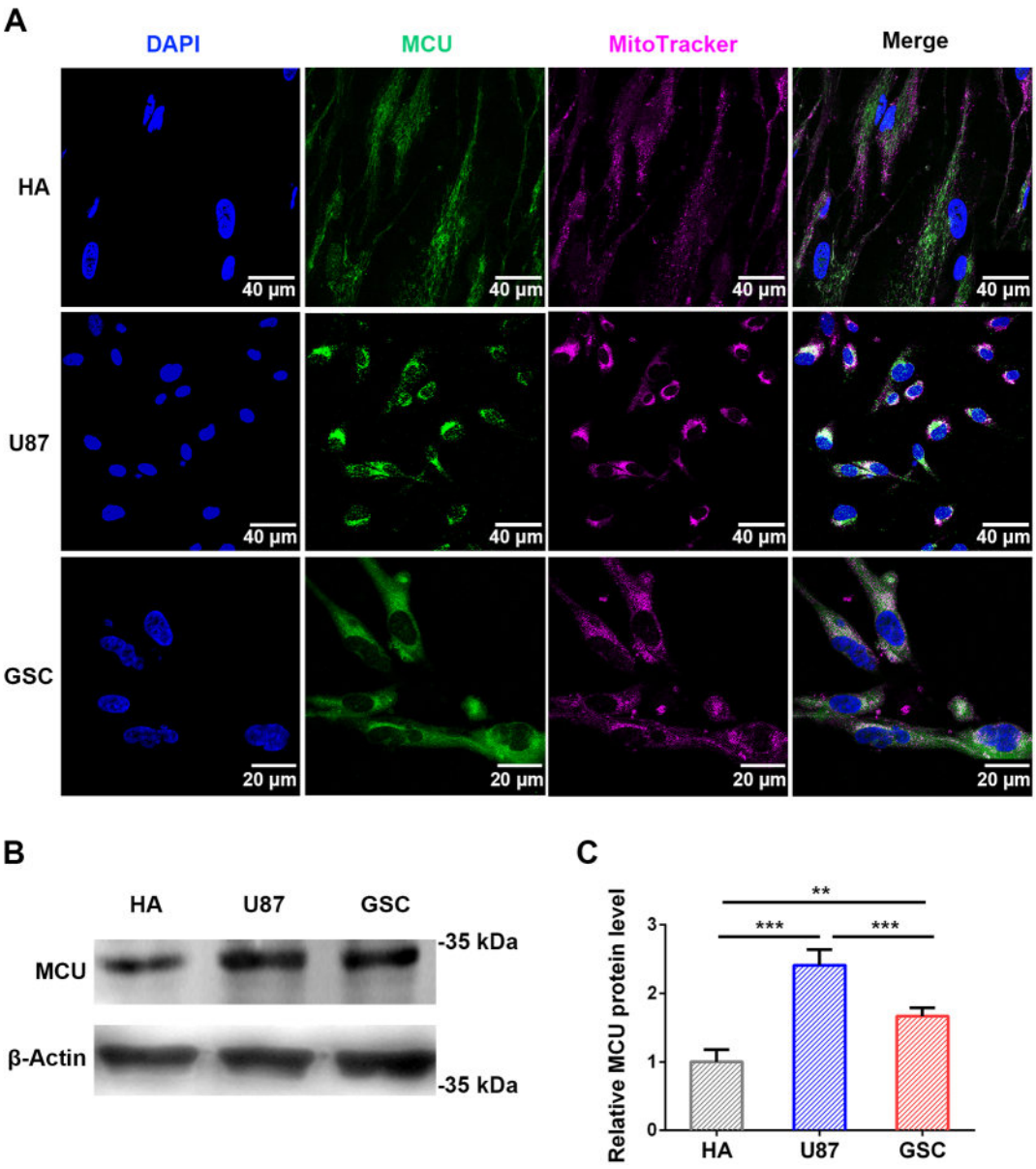

Fig. 6. The mitochondrial Ca^{2+} uniporter (MCU) in HAs, U87 GBM cells and GSCs from patients. (A) Representative confocal images showing the expression of MCU in HAs, U87 GBM cells and GSCs from patients; MitoTracker Red was used to identify mitochondria. (B) Western blot showing MCU expression in HAs, U87 GBM cells and GSCs. (C) MCU quantification using β-actin as a housekeeping protein. The data are from three distinct experimental sessions and represent the mean±s.d. ***P*<0.01, ****P*<0.001.

Immunofluorescence analysis showed vigorous staining for MCU in HAs, U87 GBM cells and GSCs from patients (Fig. 6A). Co-staining with the mitochondrial marker MitoTracker Red indicated a strong colocalization, confirming MCU localization in the mitochondria. Moreover, western blot analysis showed that the relative expression level of MCU in U87 cells was approximately twice that observed in HAs (Fig. 6B,C). In GSCs from patients, the expression level of MCU was also higher than that in HAs, but to a lesser extent.

MCU expression level influences $[Ca^{2+}]_i$ and cell proliferation

A key question is the source of the observed Ca^{2+} transients: does the rise in $[Ca^{2+}]_i$ originate from the extracellular medium or is it released from internal stores, such as mitochondria? Therefore, we analysed Ca^{2+} waves in U87 GBM and HA cells following the removal of extracellular Ca^{2+}. The cells were treated with a Ca^{2+}-free Dulbecco's modified Eagle medium (DMEM) and ratiometric Ca^{2+} imaging was performed at different time points. In U87 GBM cells, following 1 h of Ca^{2+}-free treatment, the Ca^{2+} waves started to decrease in frequency (compare Fig. 7A and B), while the basal level of R decreased from a mean value of ∼1 to 0.6 (Fig. 7G), corresponding to a drop in $[Ca^{2+}]_i$ from 100 nM to 10 nM. After 4 h, only occasional Ca^{2+} waves could be seen (Fig. 7C), and the basal level of $[Ca^{2+}]_i$ dropped to less than 10 nM. In HAs, the trend was consistent: following Ca^{2+}-free treatment the frequency of Ca^{2+} waves (Fig. 7D–F) and the basal level of R decreased (Fig. 7H). These observations suggest that internal Ca^{2+} stores are very efficient, and for several hours, they are an alternative source to the extracellular medium as a Ca^{2+} reservoir.

Next, we analysed the effects of *MCU* silencing on U87 GBM cells, and *MCU* overexpression on HAs, after transfection with short hairpin RNA (shRNA) for MCU (sh-MCU) and pDEST40-MCU-

Journal of Cell Science (2020) 133, jcs237503. doi:10.1242/jcs.237503

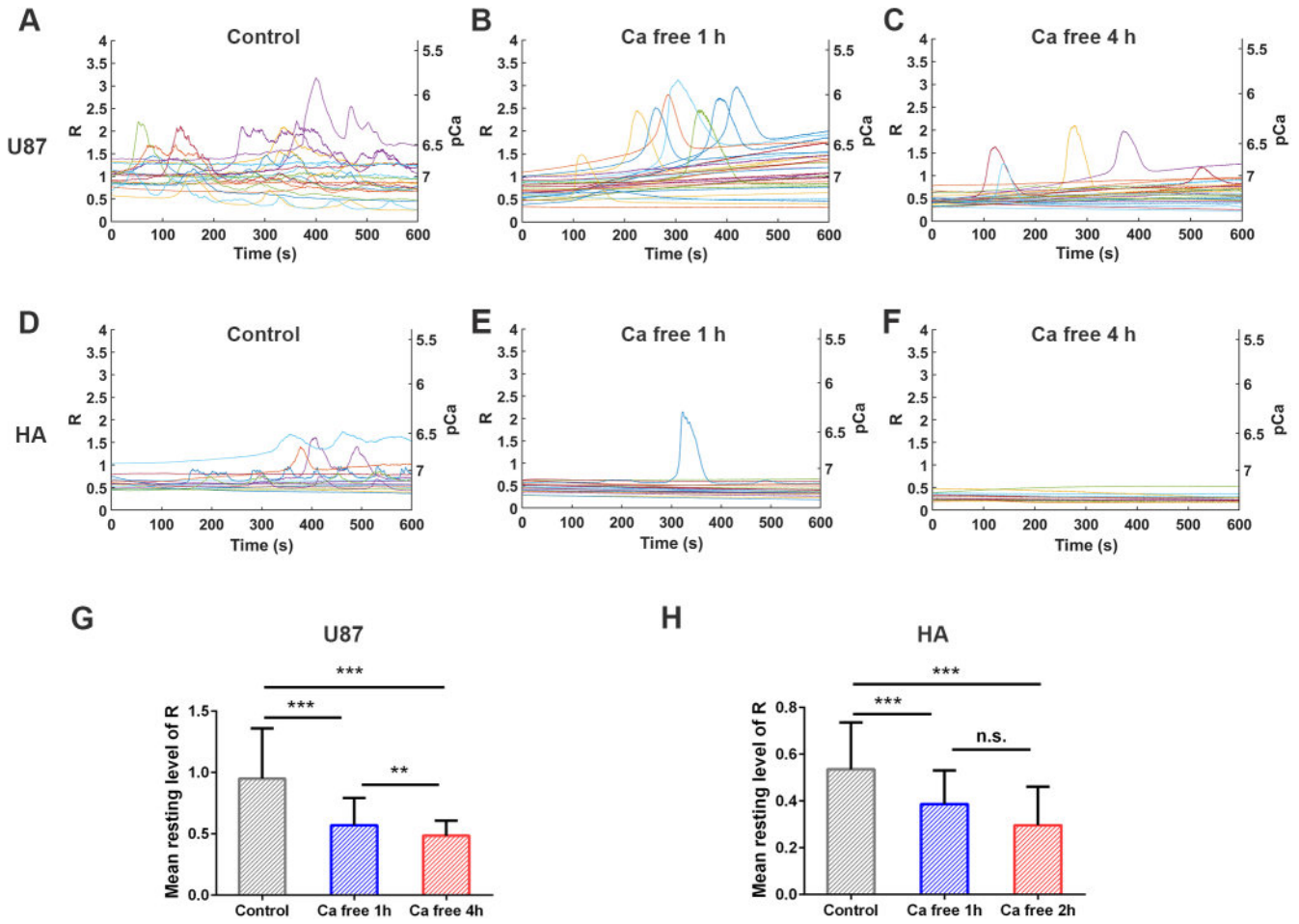

Fig. 7. The removal of extracellular Ca^{2+} reduced Ca^{2+} transients and $[Ca^{2+}]_i$ in U87 GBM and HA cells. (A–F) Representative spontaneous intracellular Ca^{2+} waves measured with ratiometric Ca^{2+} imaging in U87 GBM and HA cells in the control (A,D) or Ca^{2+}-free (B,C,E,F) medium. (G,H) Average basal values of R in U87 GBM (G) and HA (H) cells. The data in G and H are from three distinct experimental sessions and represent the mean±s.d. ***P*<0.01, ****P*<0.001. n.s., not significant.

V5-HIS, respectively. We observed that, 48 h after transfection, MCU expression in U87 GBM cells was reduced by 70% in the sh-MCU group (Fig. 8A) compared to what was measured in the non-target shRNA vector as a negative control (sh-NC) group, whereas it increased by 90% in HAs (Fig. 8B) compared to what was measured in the control cells.

Since MCU level influences the dynamics of spontaneous Ca^{2+} waves, we performed ratiometric Ca^{2+} measurements and compared the data obtained from U87 GBM to those obtained from HAs under control conditions, and to those from cells after silencing or overexpression of *MCU*. After these treatments, spontaneous Ca^{2+} waves were still present in HAs and U87 GBM cells. Following *MCU* silencing or overexpression, the mean basal level of R was not influenced in U87 GBM cells or in HAs (Fig. 8C). *MCU* silencing caused a decrease in the mean peak R in U87 GBM from a value of ∼2.5 to 2 (Fig. 8D), corresponding to a decrease in $[Ca^{2+}]_i$ from 700 nM to 400 nM. The mean peak R in HAs increased from a value of ∼1 to 1.5 after *MCU* overexpression (Fig. 8D). Previously, it was reported that cytoplasmic Ca^{2+} peaks were reduced or enhanced by *MCU* overexpression and silencing in cardiomyocytes, respectively (Drago et al., 2012), whereas the opposite occurs within the mitochondrial matrix. Differences between Drago et al.'s findings and our results are likely caused by the fact that our ratiometric Ca^{2+}-imaging experiments were based on measuring the fluorescence emitted from the whole GBM, without distinguishing among the different intracellular compartments. Therefore, we performed ratiometric Ca^{2+}-imaging experiments with U87 GBM cells stained with Fluo-4 AM, Fura Red AM and MitoTracker Red (Fig. S2A), and analysed Ca^{2+} waves in nucleus, mitochondria and cytoplasm, as described in Fig. S2. After *MCU* silencing in U87 GBM, during Ca^{2+} waves the peak R in mitochondria decreased significantly (Fig. S2B), which is consistent with Drago et al.'s conclusion, and the peak R was slightly decreased in the nucleus and slightly increased in the cytoplasm. In HAs we did not observe any significant difference in the compartments following *MCU* overexpression (Fig. S2C).

To test the effect of MCU on proliferation, we plated the same numbers of HAs and U87 cells in 96-well plates and analysed the proliferation rate using the alamarBlue® cell viability assay (see Materials and Methods). Two days after transfection, the proliferation rate was reduced by 15% in U87 GBM cells, and by 20% in HAs (Fig. 8E). These results show that both *MCU* silencing in U87 GBM cells and *MCU* overexpression in HAs significantly reduce cell proliferation. In order to understand if the reduced proliferation is associated with cell death, we carried out fluorescence-activated cell sorting (FACS) analysis. In particular, we used co-staining with Annexin V and propidium iodide (PI) to quantify live, early apoptotic, late apoptotic and necrotic cells (Fig. 8F). The percentage of dead cells and types of cell death were

Journal of Cell Science (2020) 133, jcs237503. doi:10.1242/jcs.237503

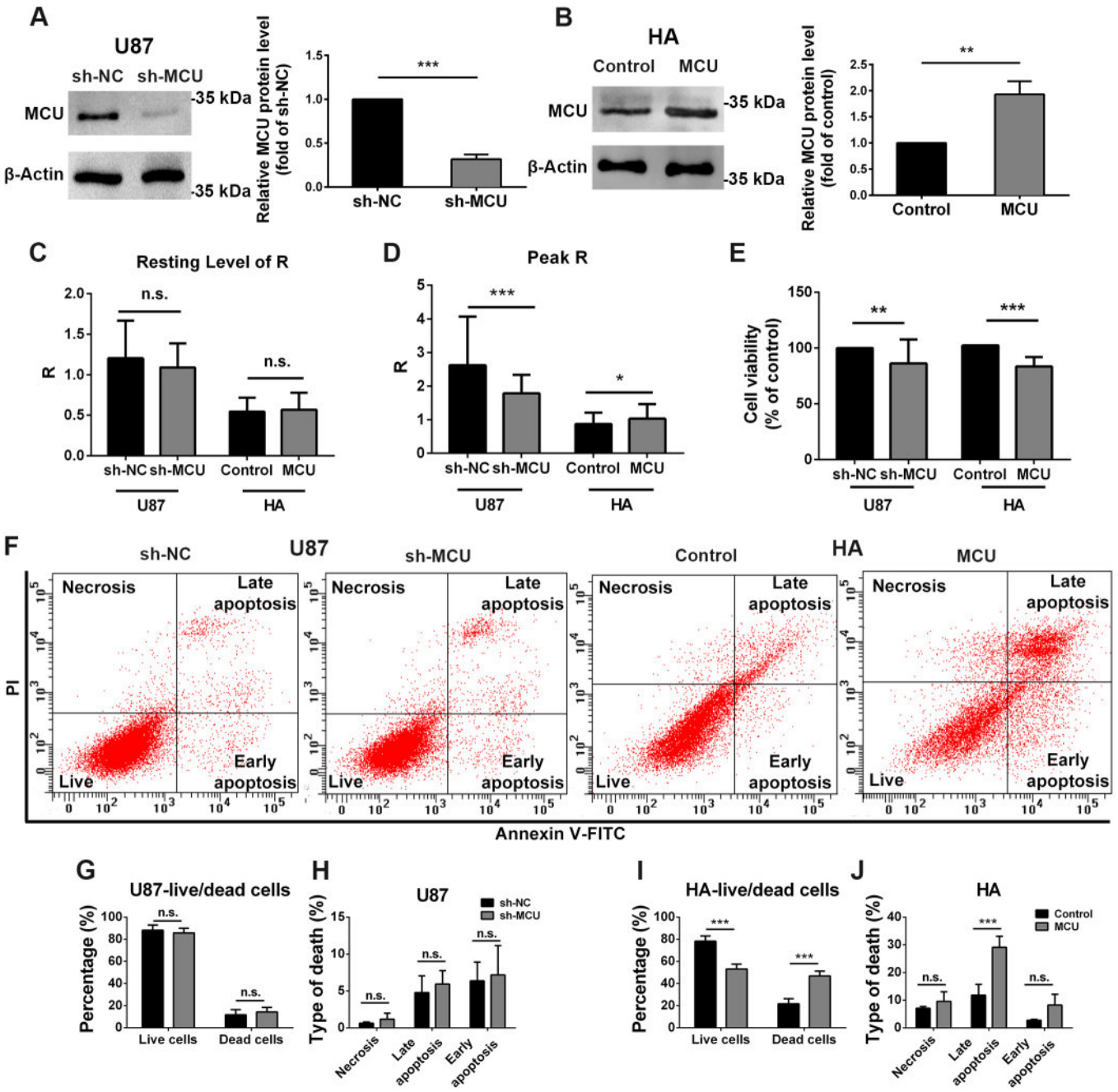

Fig. 8. The effects of the MCU expression level on U87 GBM and HA cells. (A,B) MCU expression was detected by western blotting (left) and relative protein levels were quantified (right) in U87 GBM cells after *MCU* silencing (A) and in HAs after *MCU* overexpression (B). (C,D) Average basal values of R (C) and peak R (D) in U87 GBM cells and HAs after transfection for 48 h. (E) Results from alamarBlue® cell viability assay in U87 GBM cells and HAs after transfection. (F) Representative dot plots of U87 GBM cells and HAs after transfection and staining for Annexin V and PI. (G,H) Fraction of live and dead cells in U87 GBM (G) and HA (H) cells. (I,J) Fraction of cells in necrosis, late apoptosis and early apoptosis in U87 GBM (I) and HA (J) cells. The data are from three distinct experimental sessions and represent the mean±s.d. *P<0.05, **P<0.01, ***P<0.001. Control, empty vector control; MCU, vector-expressing MCU; n.s., not significant; sh-MCU, shRNA targeting MCU; sh-NC, shRNA negative control.

not significantly different between the sh-MCU group of U87 GBM cells after *MCU* silencing and the sh-NC group (Fig. 8G,H). Interestingly, dead cells increased instead from 20% to 45% in HAs following *MCU* overexpression, and the cell death was mainly due to late apoptosis (Fig. 8I,J).

Taken together, these results suggest that *MCU* silencing in U87 GBM decreases spontaneous Ca^{2+} oscillations and cell proliferation without triggering cell death. Conversely, *MCU* overexpression in HAs slightly increases Ca^{2+} levels but causes cell death, suggesting that HAs cannot tolerate high MCU levels.

DISCUSSION

Ca^{2+} is an intracellular second messenger controlling fundamental cellular processes, such as gene transcription, cell cycle regulation and cell proliferation, and an overload of $[Ca^{2+}]_i$ triggers cell death (Zhivotovsky and Orrenius, 2011). The present investigation

illustrates three novel observations regarding Ca^{2+} regulation in GBM cells: first, Ca^{2+} waves were propagated in networks of cells connected by TMs in a complex way with variable directions and modes; second, in the U87 GBM cell line and in GSCs from patients, the basal level of $[Ca^{2+}]_i$ was ∼100 nM, but, during spontaneous waves, $[Ca^{2+}]_i$ reached an unusual high level above 1 µM for long periods without triggering cell death; and third, the levels of a protein involved in mitochondrial Ca^{2+} regulation, MCU, was altered in GBM cells compared to healthy HAs. Moreover, our analysis shows that *MCU* silencing decreases cell proliferation and alters $[Ca^{2+}]_i$ dynamics in U87 GBM cells, and *MCU* overexpression in HAs increases $[Ca^{2+}]_i$, inducing also cell death. Our findings delineate an interplay between the high level of MCU, large unusual $[Ca^{2+}]_i$ and proliferation ability, which is a potential factor in GBM malignancy, possibly caused by activation of the Ca^{2+}-calmodulin complex, CaMKII and specific transcription factors regulated by $[Ca^{2+}]_i$, such as the CREB family members (Shanmughapriya et al., 2015). Indeed, a sustained activation of CaMKII and CREB have been demonstrated to promote proliferation (Steven and Seliger, 2016).

Ca^{2+} signalling and propagation along TMs

Ca^{2+} propagation along TMs connecting different GBM cells is characterized by the occurrence of hotspots, where spontaneous increases in $[Ca^{2+}]_i$ remain localized and do not propagate (Fig. 4). These hotspots were observed with the common Ca^{2+} dye Fluo-4 AM (Fig. 4A,B) and were confirmed by ratiometric Ca^{2+} imaging (Fig. 4C,D). Similar Ca^{2+} hotspots have also been observed in fine neurites of healthy astrocytes (Bindocci et al., 2017), and the existence of these hotspots requires the existence of functional barriers at their borders. These barriers are likely to be composed of buffering organelles, such as mitochondria and/or Ca^{2+} buffers, i.e. proteins acting as local Ca^{2+} sinks (Schwaller, 2010). These buffers can be quickly saturated, and, under these circumstances, the barriers do not operate and will allow Ca^{2+} waves to propagate freely. Mobile mitochondria are the most likely candidates for this role (Agarwal et al., 2017; Jackson and Robinson, 2015), and their presence (see Fig. 4F) in TMs explains the observed behaviour. A propagating large Ca^{2+} wave will saturate the Ca^{2+}-buffering capacity of mitochondria and be likely to diffuse (Fig. 4B,D), while a small Ca^{2+} hotspot originating in the middle of a TM will remain confined in the TM because the diffusing Ca^{2+} will be completely absorbed by the mitochondria.

It is important to observe that propagation of Ca^{2+} transients in the soma and along TMs is different: Ca^{2+} transients within the soma of GBM propagate easily while Ca^{2+} transients can be blocked along TMs and fine GBM neurites. This different behaviour is a consequence of the presence of buffering organelles in TMs (Fig. 4F), where mobile mitochondria can block Ca^{2+} transients, which does not occur in GBM soma because of their larger size.

Assemblages of GBM cells appear to function as groups of elements with variable coupling, leading to an intermittent behaviour in which synchronous Ca^{2+} waves are interspersed with asynchronous Ca^{2+} waves. This intermittent behaviour can be seen within different compartments present in the same cell or in networks of cells.

Unusual elevation of $[Ca^{2+}]_i$ during spontaneous waves

Changes in $[Ca^{2+}]_i$ can be quantified by using ratiometric Ca^{2+} dyes such as Fura-2 (Harley et al., 2010; Shin et al., 2018) or using two dyes with different emission wavelengths, such as Fluo-4 AM and Fura Red AM (Assinger et al., 2015). These procedures enable quantitative determination of $[Ca^{2+}]_i$, but a caveat must be recognized: the calibration procedure to transform the measured ratio into absolute $[Ca^{2+}]_i$ could be affected by the presence of intracellular compartments and is less accurate for $[Ca^{2+}]_i$ exceeding ∼1 µM than for lower levels. Therefore, we did not determine the exact highest $[Ca^{2+}]_i$ reached during the spontaneous waves but estimated it to be in the order of 3–5 µM.

It is commonly accepted that, at steady state, the basal level of $[Ca^{2+}]_i$ is determined by Ca^{2+} influx and extrusion through the plasma membrane and is independent of the intracellular buffering capacity, i.e. the capacity of mitochondria and other organelles able to sequester and release Ca^{2+}. However, a large buffering capacity prolongs the time taken to reach the steady state and introduces unexpected dynamics. In U87 GBM and HA cells, large Ca^{2+} waves were observed for 1–2 h after removal of extracellular Ca^{2+}, indicating that, in cells, mitochondria and other organelles are excellent sources and sinks of Ca^{2+}.

These observations suggest a complex origin and control of Ca^{2+} transients: indeed the observation that large Ca^{2+} transients are observed even following removal of extracellular Ca^{2+} for 1 h (Fig. 7B,E) indicates that the release of Ca^{2+} from intracellular stores contribute to the large Ca^{2+} transients. Prolonged removal of extracellular Ca^{2+} – for more than 4 h – abolishes most of these transients (Fig. 7C,F), suggesting that extracellular Ca^{2+} plays an important role. Therefore, these transients have a dual and complex origin, i.e. release form intracellular stores and entry from the extracellular medium likely through Ca^{2+}-permeable ionic channels.

There is agreement that basal $[Ca^{2+}]_i$ varies between 100 nM and 300 nM in different cells and that changes in $[Ca^{2+}]_i$ underlie fundamental biological processes. For example, during phototransduction in vertebrate photoreceptors, $[Ca^{2+}]_i$ decreases, and this drop is responsible for light adaptation (Krizaj and Copenhagen, 2002); in addition, local increases in $[Ca^{2+}]_i$ are required for transmitter release at synapses (Koch and Dell'orco, 2013). Relatively small increases in $[Ca^{2+}]_i$ can be beneficial to cells by promoting the mitochondrial Ca^{2+} uptake machinery and thus making it more efficient (Basso et al., 2018). When $[Ca^{2+}]_i$ increases above the micromolar level, cell death can be initiated (Tombal et al., 2002). The precise dangerous level of $[Ca^{2+}]_i$ varies in different cell types, and the mechanisms through which elevation of $[Ca^{2+}]_i$ promotes cell death include activation of Ca^{2+}-dependent proteases, nitric oxide synthases, the CREB family of Ca^{2+}-dependent transcription factors, caspases and calpain proteins (Caro and Cederbaum, 2002; Teich et al., 2015). The Ca^{2+} sensitivity of many of these proteins is in the micromolar range (Caro and Cederbaum, 2002); for this reason, to avoid triggering cell death, it is important to limit sustained increases in $[Ca^{2+}]_i$ to below 1 µM.

As shown in Fig. 5, in U87 GBM cells and in GSCs from patients, $[Ca^{2+}]_i$ increased above 1 µM without leading to cell death. Conversely, overexpression of *MCU* in HAs increased $[Ca^{2+}]_i$ and led to cell death (Fig. 8I). These results suggest that GBM cells might have molecular mechanisms that enable them to accommodate large increases in $[Ca^{2+}]_i$, implying the existence of a larger pool of intracellular buffering organelles or Ca^{2+}-buffering proteins in GBM cells than in normal cells. These mechanisms could be complemented by an efficient mechanism of Ca^{2+} extrusion, and the overexpression of key anti-apoptotic signals (Ziegler et al., 2008), such as members of the BCL2 family (Belmar and Fesik, 2015), that inhibit the activity of caspase-3, caspase-7 and caspase-9.

The role of MCU in Ca^{2+} transients

Greater mitochondrial buffering capacity caused by higher levels of MCU could have contributed to the presence of Ca^{2+} hotspots along TMs and the unusual levels of $[Ca^{2+}]_i$ observed in GBM cells compared to normal cells during the spontaneous Ca^{2+} waves. One way to rapidly neutralize transient elevations in $[Ca^{2+}]_i$ is by sequestering the Ca^{2+} into various intracellular stores of Ca^{2+}, such as those in the endoplasmic reticulum (ER) and the Ca^{2+} matrix inside the mitochondria. MCU plays a key role in sequestering $[Ca^{2+}]_i$ by promoting $[Ca^{2+}]_i$ accumulation in the mitochondrial matrix, and mitochondrial Ca^{2+} elevation favours drug resistance and tumour maintenance in cancer cells (Vultur et al., 2018). MCU is characterized by a low Ca^{2+} affinity [dissociation constant (KD)=20–30 µM] and is normally closed. However, when surrounding Ca^{2+} levels are high enough to form high-$[Ca^{2+}]_i$ (∼10 µM) microdomains in close proximity to the mouth of the ER, MCU can be activated to take up Ca^{2+} into mitochondria (Arruda and Hotamisligil, 2015; Villalobos et al., 2017). Upregulation of MCU has been demonstrated in different cancers, such as breast cancer (Hall et al., 2014) and hepatocellular carcinoma (Ren et al., 2018), and *MCU* silencing can reduce mitochondrial Ca^{2+} uptake and metastatic cell motility and potentiate cell death, suggesting that *MCU* overexpression protects cancer cells from apoptosis (Curry et al., 2013; Tosatto et al., 2016).

An elevated level of $[Ca^{2+}]_i$ is expected to activate several transcription factors involved in the regulation of cell division and proliferation, such as the CREB family (Shanmughapriya et al., 2015). In GBM cells, the spontaneous Ca^{2+} waves started from a basal level of ∼100 nM and reached a peak at 1–3 µM or higher. Following *MCU* silencing, spontaneous Ca^{2+} waves were still present and GBM cells had reduced proliferation. These findings indicate that the spontaneous Ca^{2+} waves from 100 nM to 1–3 µM or higher could be responsible for the high proliferation in GBM cells. Therefore, the key hallmark of GBM malignancy, abnormal rate of proliferation, is caused – to some extent – by the observed high MCU level and unusual elevation of $[Ca^{2+}]_i$.

In addition, *MCU* transcription is controlled by the CREB transcription factors and CREB binding to the *MCU* promoter, which is regulated by $[Ca^{2+}]_i$. Therefore, we can deduce that, in GBM, there is also a positive feedback between the level of MCU and spontaneous Ca^{2+} transients.

Conclusions

In conclusion, our study elucidates how high MCU level and large Ca^{2+} transients are linked to malignancy in GBM. Indeed, an unusual elevation of Ca^{2+} transients is expected to activate biochemical pathways involved in cell proliferation, the key hallmark of GBM malignancy. Since cell proliferation is reduced when MCU is silenced, targeting the MCU complex and intracellular Ca^{2+} regulation could be a new unexplored strategy for the treatment of GBM.

MATERIALS AND METHODS

Cell culture

HAs (#N7805100, Thermo Fisher Scientific) and U87 GBM cells (#89081402, Sigma-Aldrich) were cultured in DMEM supplemented with 10% fetal bovine serum (FBS; Invitrogen, Life Technologies, Gaithersburg, MD), 1% PenStrep (100 U/ml penicillin and 100 µg/ml streptomycin; Invitrogen). For HAs, 1% N-2 Supplement (Thermo Fisher Scientific) was added to the culture medium and all plates used to culture HAs were covered with Geltrex™ matrix (Thermo Fisher Scientific). The mCherry-labelled U87 GBM cells were kindly provided by Prof. Antonello Mallamaci (Neurobiology Sector, International School for Advanced Studies, Trieste, Italy). U87 GBM cells were acutely infected at a concentration of 500 cells/µl by a mix containing lentiviral vector, LV_Pgk1p-mCherry, at a multiplicity of infection of 6.

To obtain human GSCs, human GBM samples were collected by the Neurosurgery Department of the Azienda Ospedaliera Universitaria of Udine, after informed consent was obtained, in accordance with the Declaration of Helsinki, and with approval by the Independent Ethics Committee of the University Hospital of Udine (Approval 196/2014Em). Human GSCs were expanded in adherent culture following the protocol optimized by Dirk's group to maintain undifferentiated GSCs in adherent condition (Andolfi et al., 2014; Bourkoula et al., 2014; Pollard et al., 2009). Briefly, tissue samples were mechanically enzymatically dissociated and single-cell suspensions were cultured with adhesion on laminin-coated dishes in a growing medium composed of the following: Neurobasal™-A Medium (#10888, Gibco by Invitrogen) supplemented with 2 mM L-glutamine (#G7513, Sigma-Aldrich), 1× N2 supplement [7.5% bovine serum albumin (BSA), 0.63 µg/ml progesterone, 1.6 mg/ml putrescine dihydrochloride, 0.52 µg/ml sodium selenite], 25 µg/ml insulin (#I2643, Sigma-Aldrich), 1× penicillin-streptomycin (#15140122, Gibco by Invitrogen), 100 µg/ml h-apo-transferrin (#P4333, Sigma-Aldrich), 1× B-27 supplement (#17504-044, Gibco by Invitrogen), 20 ng/ml h-FGF-basic (#100-18B, Peprotech), 20 ng/ml h-EGF (#AF-100-15, Peprotech).

All the cells were cultured in an incubator at 37°C, 5%O_2/5% CO_2, 95% relative humidity and medium was replaced every 3 days. Once 70–80% of confluence had been reached, the cells were re-plated at a density of $2.5\times10^3/cm^2$.

Transfection

pDEST40-MCU-V5-HIS was Addgene plasmid #31731, deposited by Vamsi Mootha, and sh-MCU was obtained from Sigma-Aldrich (#SHCLNG-NM_138357). Twenty-four hours after plating the cells, HA cells were transfected with pDEST40-MCU-V5-HIS using the empty vector as a control; U87 GBM cells were transfected with sh-MCU using non-target shRNA vector as a negative control (sh-NC). Lipofectamine 3000® transfection reagent (Invitrogen) was used following the manufacturer's protocol. Forty-eight hours after transfection, the following tests were carried out.

Live-cell imaging

Cells were plated at a density of 8.0×10^4 cells into 35-mm dishes with a glass bottom and cultured for 2 days. Before optical recording, cells were stained with 5 µl/ml Vybrant™ DiD Cell-Labelling Solution (Thermo Fisher Scientific) for 20 min and then washed with a warm medium. In specific experiments, cells were stained with 25 nM mitochondrion-selective probe MitoTracker® Red FM (Thermo Fisher Scientific) for 30 min and then washed with warm medium. Live-cell imaging experiments were performed on an epi-fluorescence microscope (Olympus IX-83, Olympus) equipped with a chamber incubator (Okolab, Pozzuoli, Italy) and light-emitting diode (LED) illumination (λ=590 nm for mCherry and MitoTracker; λ=660 nm for Vybrant™ DiD). During all imaging experiments, cells were kept at 37°C, 5% CO_2 and 95% humidity. Time-lapse images were taken with 500 ms of exposure time and one image was taken every 1 or 2 min. Images were acquired with a charge-coupled device (CCD) sensor at 12-bit depth (ORCA-D2, Hamamatsu) using a 20× air objective (Olympus, NA=0.75) or a 40× oil objective (Olympus, NA=1.3) with a spatial resolution of 1280×960 pixels.

Ca^{2+} imaging

In Ca^{2+}-imaging experiments, 2.0×10^4 cells were plated on a flat coverslip and cultured for 1–6 days, and subsequently were loaded with the membrane-permeable Ca^{2+} dye Fluo-4 AM (Life Technologies) by incubation with 4 µM Fluo-4 AM (dissolved in anhydrous DMSO, 4 mM stock solution) and Pluronic F-127 20% solution in DMSO (Life Technologies) at a ratio of 1:1 in Ringer's solution (145 mM NaCl, 3 mM KCl, 1.5 mM $CaCl_2$, 1 mM $MgCl_2$, 10 mM glucose and 10 mM Hepes, pH 7.4) at 37°C for 30 min. After incubation, the cultures were washed with Ringer's solution for 20 min and then transferred to the stage of a Nikon Eclipse Ti-U inverted microscope equipped with a piezoelectric table (Nano-ZI Series 500 µm range, Mad City Labs), an HBO 103 W/2 mercury

short arc lamp (Osram, Munich, Germany), a mirror unit (465–495 nm excitation bandpass filter, 505 nm dichroic, 515–555 nm emission bandpass filter) and an Electron Multiplier CCD Camera C9100-13 (Hamamatsu Photonics, Japan). Ca^{2+}-imaging recordings were performed at room temperature and images were acquired using the NIS Element software (Nikon, Japan) with an S-Fluor 20×/0.75 NA objective, at a sampling rate of 3–10 Hz, with a spatial resolution of 256×256 pixels for 15 min. To avoid saturation of the signals, excitation light intensity was attenuated by ND4 and ND8 neutral density filters (Nikon, Tokyo, Japan).

For ratiometric Ca^{2+}-imaging experiments, cells were loaded with 1.5 µM Fluo-4 AM [dissolved in anhydrous DMSO (Sigma-Aldrich), 1.5 mM stock solution], 2.5 µM Fura Red AM [dissolved in anhydrous DMSO (Sigma-Aldrich), 2.5 mM stock solution] and 1 µl Pluronic F-127 20% solution in DMSO (Life Technologies) in 1 ml Ringer's solution for 30 min. After incubation, the cultures were washed with Ringer's solution for 20 min and then transferred to the stage of an epi-fluorescence microscope (Olympus IX-83, Olympus) equipped with a chamber incubator (Okolab, Pozzuoli, Italy), LED illumination (λ=490 nm for both Fluo-4 AM and Fura Red AM) and a CCD camera (ORCA-D2, Hamamatsu) with a dual sensor to record the fluorescence images from Fluo-4 AM (520±17.5 nm) and Fura Red AM (640±37.5 nm) simultaneously. During all imaging experiments, cells were kept at 37°C, 5% CO_2 and 95% humidity. Time-lapse images were taken with 300 ms of exposure time. All acquisitions were operated with a 20× air objective (Olympus, NA=0.75) or a 40× oil objective (Olympus, NA=1.3).

Immunofluorescence

Cells were grown on coverslips for 2 days and subsequently washed with ice-cold PBS, then fixed with 4% paraformaldehyde for 10 min at room temperature, followed by permeabilization with PBS plus 0.1% Triton X-100, blocked with 3% BSA and incubated overnight with primary antibody anti-MCU mouse monoclonal (1:100; ab219827, Abcam, Cambridge, UK). The cells were then washed with PBS three times for 5 min each, and incubated with Alexa Fluor 488-labelled goat anti-mouse secondary antibody (1:400; Life Technologies) at room temperature for 1 h. The cells were examined with a confocal microscope (Nikon A1R).

Western blotting

Cells were lysed in RIPA buffer (50 mM Tris-HCl, pH 7.4, 150 mM, NaCl, 5 mM EDTA, pH 8.0, 30 mM NaF, 1 mM Na_3VO_4, 40 mM β-glycerophosphate, 0.1 mM PMSF, protease inhibitors, 10% glycerol and 1% Nonidet-P40). Whole-cell extracts were fractionated by SDS-PAGE and transferred to a nitrocellulose membrane using a transfer apparatus according to the manufacturer's protocols (Bio-Rad). After incubation with 3% in TBST (10 mM Tris-HCl, pH 8.0, 150 mM NaCl, 0.5% Tween 20) for 1 h, the membrane was washed once with TBST and incubated with antibodies against MCU (1:500) at 4°C overnight and horseradish peroxidase (HRP)-conjugated actin (1:3000) at room temperature for 15 min. Membranes were washed three times for 10 min and incubated with a 1:3000 dilution of HRP-conjugated anti-mouse for 2 h. Blots were washed with TBST three times and developed with an ECL system (Amersham Biosciences) according to the manufacturer's protocols.

Quantification of cell viability

The alamarBlue® (Thermo Fisher Scientific) assay was performed to evaluate the metabolic activity of U87 cells with and without MCU silencing, and HA cells with and without MCU overexpression. After transfection for 48 h, cells were washed in PBS pre-warmed at 37°C, after which 10% alamarBlue® in growth medium was added. After 4 h of incubation at 37°C, absorbance was measured at 570/600 nm wavelengths and percentage cell viability compared with the control group was calculated following the manufacturer's instructions.

Analysis of cell death was performed using the Annexin V-FITC Apoptosis Detection Kit (BioLegend) following the manufacturer's instructions. Briefly, cells, resuspended in Binding Buffer at a cell density of 2-5×10^5/ml were first stained with Annexin V-FITC (A-V) and, after washing, with PI (1 µg/ml). Cells were then analysed by FACSCanto III (BD Biosciences), using FACSDiva software. On the basis of PI and A-V staining, cells were considered live cells (PI^-/A-V^-), cells in early apoptosis (PI^-/A-V^+), cells in late apoptosis (PI^+/A-V^+) or necrotic cells (PI^+/A-V^-).

Quantification and analysis of Ca^{2+}-imaging data

Acquired images were processed with the ImageJ software. The somas or sections of TMs were localized in a specific region of interest (ROI; see red outlined area in Fig. 1A), and a dark region in which no cells were visible was selected to compute the background, which was then subtracted from the whole image. Ca^{2+} transients of each cell signal were extracted by setting a threshold equal to three times the s.d. of the baseline. The decay of $I_f(t)$ was fitted to a cubic spline $Y(t)$ interpolating $I_f(t)$ at 10 or 20 points. $Y(t)$ was then added to the original optical signal to compensate for dye bleaching, and the fractional optical signal was calculated as follows:

$$\frac{DF}{F_0} = \frac{Y(t) + I_f(t)}{I_f(0)}, \quad (1)$$

where $I_f(0)$ is the fluorescence intensity at the beginning of the recording.

For ratiometric Ca^{2+} imaging, image sequences from Fluo-4 AM and Fura Red AM labelling were separated by ImageJ. A ROI for subtracting the background and ROIs around the cell bodies were then selected. Mean grey values from two channels were measured over time as shown in Fig. 1B and the amplitude of optical signals from the two dyes decayed because of bleaching. After background subtraction, $F1$ (cellular green emission by Fluo-4 AM) and $F2$ (cellular red emission by Fura Red AM) were used to calculate the fluorescence ratio R as follows:

$$R = F1/F2. \quad (2)$$

The time course of R was less affected by dye bleaching (Fig. 1C) because bleaching had almost the same time constant for Fluo-4 AM and Fura Red AM. When $F1$ increased and concomitantly $F2$ decreased, as in Fig. 1B, there is a genuine increase in $[Ca^{2+}]_i$. If $F1$ and $F2$ do not have changes with a similar time course with opposite polarity, fluorescent changes are usually caused by artefacts most commonly by the motion of visualized cells. GBM cells usually move significantly and in order to observe genuine changes of $[Ca^{2+}]_i$ it is necessary to use ratiometric Ca^{2+} imaging

$[Ca^{2+}]_i$ measurements were performed as previously described (Assinger et al., 2015). Briefly, fluorescent cells were treated with ionomycin (5 µM) and R was measured with free Ca^{2+} ranging from 0 to 28,000 nM by mixing Calcium Calibration Buffer 10 mM CaEGTA and Calcium Calibration Buffer zero (10 mM K_2EGTA) (Life Technologies) at different ratios. The following equation was used to determine $[Ca^{2+}]_i$ (Assinger et al., 2015):

$$[Ca^{2+}]_i = K_d \times (R - R_{min})/(R_{max} - R), \quad (3)$$

where K_d, R_{min} and R_{max} were obtained during Ca^{2+} calibration experiments. In the calibration experiment illustrated in Fig. 1D, the obtained values of K_d, R_{min} and R_{max} were 810.3 nM, 0.56 and 4.60, respectively, which were obtained from averaging data of 32 GBM cells from three distinct experimental sessions.

Statistical analysis

Data are shown as the mean±s.d. from at least three culture preparations. The quantified data were analysed with one-way analysis of variance (ANOVA) or two-way ANOVA, followed by Bonferroni post-hoc comparisons, using GraphPad Prism version 6.01. The number of replicas and statistical tests used for each experiment is specified in the figure legends or in the Results section. Significance was set to $*P<0.05$, $**P<0.01$ and $***P<0.001$.

Acknowledgements

We thank Prof. Antonello Mallamaci for his helpful suggestions on RNA interference experiments, and Diletta Pozzi, Nicola Galvanetto and Simone Mortal for help with data analysis and useful discussions.

Competing interests

The authors declare no competing or financial interests.

Author contributions

Conceptualization: M.S., Y.Y., V.T.; Methodology: X.L., R.S., A.B., D.C., F.C., I.M., V.T.; Formal analysis: X.L.; Data curation: X.L., R.S.; Writing - original draft: X.L.,

V.T.; Writing - review & editing: X.L., R.S., A.B., D.C., T.I., M.S., F.C., I.M., Y.Y., V.T.; Supervision: V.T.; Project administration: V.T.; Funding acquisition: D.C., V.T.

Funding
This work was supported by funds from Regione Autonoma Friuli Venezia Giulia for the projects 'Infiltrazione nei gliomi: nuovo target terapeutico – Glioblastoma' [No. 605/SPS] and 'ARES – Against brain cancer: finding personalized therapies with *in silico* and *in vitro* strategies' [No. 738/LAVFORU].

Supplementary information
Supplementary information available online at
http://jcs.biologists.org/lookup/doi/10.1242/jcs.237503.supplemental

Peer review history
The peer review history is available online at
https://jcs.biologists.org/lookup/doi/10.1242/jcs.236503.reviewer-comments.pdf

References

Agarwal, A., Wu, P.-H., Hughes, E. G., Fukaya, M., Tischfield, M. A., Langseth, A. J., Wirtz, D. and Bergles, D. E. (2017). Transient opening of the mitochondrial permeability transition pore induces microdomain calcium transients in astrocyte processes. *Neuron* **93**, 587-605.e7. doi:10.1016/j.neuron.2016.12.034

Andolfi, L., Bourkoula, E., Migliorini, E., Palma, A., Pucer, A., Skrap, M., Scoles, G., Beltrami, A. P., Cesselli, D. and Lazzarino, M. (2014). Investigation of adhesion and mechanical properties of human glioma cells by single cell force spectroscopy and atomic force microscopy. *PLoS ONE* **9**, e112582. doi:10.1371/journal.pone.0112582

Arruda, A. P. and Hotamisligil, G. S. (2015). Calcium homeostasis and organelle function in the pathogenesis of obesity and diabetes. *Cell Metab.* **22**, 381-397. doi:10.1016/j.cmet.2015.06.010

Assinger, A., Volf, I. and Schmid, D. (2015). A novel, rapid method to quantify intraplatelet calcium dynamics by ratiometric flow cytometry. *PLoS ONE* **10**, e0122527. doi:10.1371/journal.pone.0122527

Basso, E., Rigotto, G., Zucchetti, A. E. and Pozzan, T. (2018). Slow activation of fast mitochondrial Ca^{2+} uptake by cytosolic Ca^{2+}. *J. Biol. Chem.* **293**, 17081-17094. doi:10.1074/jbc.RA118.002332

Belmar, J. and Fesik, S. W. (2015). Small molecule Mcl-1 inhibitors for the treatment of cancer. *Pharmacol. Ther.* **145**, 76-84. doi:10.1016/j.pharmthera.2014.08.003

Bindocci, E., Savtchouk, I., Liaudet, N., Becker, D., Carriero, G. and Volterra, A. (2017). Three-dimensional Ca^{2+} imaging advances understanding of astrocyte biology. *Science* **356**, eaai8185. doi:10.1126/science.aai8185

Bourkoula, E., Mangoni, D., Ius, T., Pucer, A., Isola, M., Musiello, D., Marzinotto, S., Toffoletto, B., Sorrentino, M., Palma, A. et al. (2014). Glioma-associated stem cells: a novel class of tumor-supporting cells able to predict prognosis of human low-grade gliomas. *Stem Cells* **32**, 1239-1253. doi:10.1002/stem.1605

Caro, A. A. and Cederbaum, A. I. (2002). Role of calcium and calcium-activated proteases in CYP2E1-dependent toxicity in HEPG2 cells. *J. Biol. Chem.* **277**, 104-113. doi:10.1074/jbc.M107864200

Curry, M. C., Peters, A. A., Kenny, P. A., Roberts-Thomson, S. J. and Monteith, G. R. (2013). Mitochondrial calcium uniporter silencing potentiates caspase-independent cell death in MDA-MB-231 breast cancer cells. *Biochem. Biophys. Res. Commun.* **434**, 695-700. doi:10.1016/j.bbrc.2013.04.015

Dong, Z., Shanmughapriya, S., Tomar, D., Siddiqui, N., Lynch, S., Nemani, N., Breves, S. L., Zhang, X., Tripathi, A., Palaniappan, P. et al. (2017). Mitochondrial Ca(2+) uniporter is a mitochondrial luminal redox sensor that augments MCU channel activity. *Mol. Cell* **65**, 1014-1028 e1017. doi:10.1016/j.molcel.2017.01.032

Drago, I., De Stefani, D., Rizzuto, R. and Pozzan, T. (2012). Mitochondrial Ca2+ uptake contributes to buffering cytoplasmic Ca2+ peaks in cardiomyocytes. *Proc. Natl. Acad. Sci. USA* **109**, 12986-12991. doi:10.1073/pnas.1210718109

Farfariello, V., Iamshanova, O., Germain, E., Fliniaux, I. and Prevarskaya, N. (2015). Calcium homeostasis in cancer: a focus on senescence. *Biochim. Biophys. Acta* **1853**, 1974-1979. doi:10.1016/j.bbamcr.2015.03.005

Fischer, T. H., Herting, J., Tirilomis, T., Renner, A., Neef, S., Toischer, K., Ellenberger, D., Forster, A., Schmitto, J. D., Gummert, J. et al. (2013). Ca^{2+}/calmodulin-dependent protein kinase II and protein kinase A differentially regulate sarcoplasmic reticulum Ca^{2+} leak in human cardiac pathology. *Circulation* **128**, 970-981. doi:10.1161/CIRCULATIONAHA.113.001746

Foskett, J. K. and Philipson, B. (2015). The mitochondrial Ca^{2+} uniporter complex. *J. Mol. Cell. Cardiol.* **78**, 3-8. doi:10.1016/j.yjmcc.2014.11.015

Hall, D. D., Wu, Y., Domann, F. E., Spitz, D. R. and Anderson, M. E. (2014). Mitochondrial calcium uniporter activity is dispensable for MDA-MB-231 breast carcinoma cell survival. *PLoS ONE* **9**, e96866. doi:10.1371/journal.pone.0096866

Hamilton, J., Brustovetsky, T., Rysted, J. E., Lin, Z., Usachev, Y. M. and Brustovetsky, N. (2018). Deletion of mitochondrial calcium uniporter incompletely inhibits calcium uptake and induction of the permeability transition pore in brain mitochondria. *J. Biol. Chem.* **293**, 15652-15663. doi:10.1074/jbc.RA118.002926

Harley, W., Floyd, C., Dunn, T., Zhang, X. D., Chen, T. Y., Hegde, M., Palandoken, H., Nantz, M. H., Leon, L., Carraway, K. L.Jr et al. (2010). Dual inhibition of sodium-mediated proton and calcium efflux triggers non-apoptotic cell death in malignant gliomas. *Brain Res.* **1363**, 159-169. doi:10.1016/j.brainres.2010.09.059

Jackson, J. G. and Robinson, M. B. (2015). Reciprocal regulation of mitochondrial dynamics and calcium signaling in astrocyte processes. *J. Neurosci.* **35**, 15199-15213. doi:10.1523/jneurosci.2049-15.2015

Koch, K. W. and Dell'orco, D. (2013). A calcium-relay mechanism in vertebrate phototransduction. *ACS Chem. Neurosci.* **4**, 909-917. doi:10.1021/cn400027z

Krizaj, D. and Copenhagen, D. R. (2002). Calcium regulation in photoreceptors. *Front. Biosci.* **7**, d2023-d2044. doi:10.2741/A896

Leclerc, C., Haeich, J., Aulestia, F. J., Kilhoffer, M. C., Miller, A. L., Neant, I., Webb, S. E., Schaeffer, E., Junier, M. P., Chneiweiss, H. et al. (2016). Calcium signaling orchestrates glioblastoma development: facts and conjunctures. *Biochim. Biophys. Acta* **1863**, 1447-1459. doi:10.1016/j.bbamcr.2016.01.018

Liu, K. H., Yang, S. T., Lin, Y. K., Lin, J. W., Lee, Y. H., Wang, J. Y., Hu, C. J., Lin, E. Y., Chen, S. M., Then, C. K. et al. (2015). Fluoxetine, an antidepressant, suppresses glioblastoma by evoking AMPAR-mediated calcium-dependent apoptosis. *Oncotarget* **6**, 5088-5101. doi:10.18632/oncotarget.3243

Mammucari, C., Gherardi, G. and Rizzuto, R. (2017). Structure, activity regulation, and role of the mitochondrial calcium uniporter in health and disease. *Front. Oncol.* **7**, 139. doi:10.3389/fonc.2017.00139

Marchi, S. and Pinton, P. (2016). Alterations of calcium homeostasis in cancer cells. *Curr. Opin. Pharmacol.* **29**, 1-6. doi:10.1016/j.coph.2016.03.002

McFerrin, M. B., Turner, K. L., Cuddapah, V. A. and Sontheimer, H. (2012). Differential role of IK and BK potassium channels as mediators of intrinsic and extrinsic apoptotic cell death. *Am. J. Physiol. Cell Physiol.* **303**, C1070-C1078. doi:10.1152/ajpcell.00040.2012

Osswald, M., Jung, E., Sahm, F., Solecki, G., Venkataramani, V., Blaes, J., Weil, S., Horstmann, H., Wiestler, B., Syed, M. et al. (2015). Brain tumour cells interconnect to a functional and resistant network. *Nature* **528**, 93-98. doi:10.1038/nature16071

Osuka, S. and Van Meir, E. G. (2017). Overcoming therapeutic resistance in glioblastoma: the way forward. *J. Clin. Investig.* **127**, 415-426. doi:10.1172/JCI89587

Pollard, S. M., Yoshikawa, K., Clarke, I. D., Danovi, D., Stricker, S., Russell, R., Bayani, J., Head, R., Lee, M., Bernstein, M. et al. (2009). Glioma stem cell lines expanded in adherent culture have tumor-specific phenotypes and are suitable for chemical and genetic screens. *Cell Stem Cell* **4**, 568-580. doi:10.1016/j.stem.2009.03.014

Rand, V., Prebble, E., Ridley, L., Howard, M., Wei, W., Brundler, M. A., Fee, B. E., Riggins, G. J., Coyle, B., Grundy, R. G. et al. (2008). Investigation of chromosome 1q reveals differential expression of members of the S100 family in clinical subgroups of intracranial paediatric ependymoma. *Br. J. Cancer* **99**, 1136-1143. doi:10.1038/sj.bjc.6604651

Ren, T., Wang, J., Zhang, H., Yuan, P., Zhu, J., Wu, Y., Huang, Q., Guo, X., Zhang, J., Ji, L. et al. (2018). MCUR1-mediated mitochondrial calcium signaling facilitates cell survival of hepatocellular carcinoma via reactive oxygen species-dependent P53 degradation. *Antioxid Redox Signal.* **28**, 1120-1136. doi:10.1089/ars.2017.6990

Robil, N., Petel, F., Kilhoffer, M. C. and Haiech, J. (2015). Glioblastoma and calcium signaling - analysis of calcium toolbox expression. *Int. J. Dev. Biol.* **59**, 407-415. doi:10.1387/ijdb.150200jh

Schwaller, B. (2010). Cytosolic Ca2+ buffers. *Cold Spring Harb. Perspect. Biol.* **2**, a004051. doi:10.1101/cshperspect.a004051

Shanmughapriya, S., Rajan, S., Hoffman, N. E., Zhang, X., Guo, S., Kolesar, J. E., Hines, K. J., Ragheb, J., Jog, N. R., Caricchio, R. et al. (2015). Ca^{2+} signals regulate mitochondrial metabolism by stimulating CREB-mediated expression of the mitochondrial Ca^{2+} uniporter gene MCU. *Sci. Signal.* **8**, ra23. doi:10.1126/scisignal.2005673

Shin, D. H., Leem, D. G., Shin, J. S., Kim, J. I., Kim, K. T., Choi, S. Y., Lee, M. H., Choi, J. H. and Lee, K. T. (2018). Compound K induced apoptosis via endoplasmic reticulum Ca^{2+} release through ryanodine receptor in human lung cancer cells. *J. Ginseng Res.* **42**, 165-174. doi:10.1016/j.jgr.2017.01.015

Steven, A. and Seliger, B. (2016). Control of CREB expression in tumors: from molecular mechanisms and signal transduction pathways to therapeutic target. *Oncotarget* **7**, 35454-35465. doi:10.18632/oncotarget.7721

Teich, A. F., Nicholls, R. E., Puzzo, D., Fiorito, J., Purgatorio, R., Fa', M. and Arancio, O. (2015). Synaptic therapy in Alzheimer's disease: a CREB-centric approach. *Neurotherapeutics* **12**, 29-41. doi:10.1007/s13311-014-0327-5

Tombal, B., Denmeade, S. R., Gillis, J. M. and Isaacs, J. T. (2002). A supramicromolar elevation of intracellular free calcium ($[Ca^{2+}]_i$) is consistently required to induce the execution phase of apoptosis. *Cell Death Differ.* **9**, 561-573. doi:10.1038/sj.cdd.4400999

Tosatto, A., Sommaggio, R., Kummerow, C., Bentham, R. B., Blacker, T. S., Berecz, T., Duchen, M. R., Rosato, A., Bogeski, I., Szabadkai, G. et al. (2016).

The mitochondrial calcium uniporter regulates breast cancer progression via HIF-1alpha. *EMBO Mol. Med.* **8**, 569-585. doi:10.15252/emmm.201606255

Villalobos, C., Sobradillo, D., Hernández-Morales, M. and Núñez, L. (2017). Calcium remodeling in colorectal cancer. *Biochim. Biophys. Acta Mol. Cell Res.* **1864**, 843-849. doi:10.1016/j.bbamcr.2017.01.005

Vultur, A., Gibhardt, C. S., Stanisz, H. and Bogeski, I. (2018). The role of the mitochondrial calcium uniporter (MCU) complex in cancer. *Pflugers Arch.* **470**, 1149-1163. doi:10.1007/s00424-018-2162-8

Zhivotovsky, B. and Orrenius, S. (2011). Calcium and cell death mechanisms: a perspective from the cell death community. *Cell Calcium* **50**, 211-221. doi:10.1016/j.ceca.2011.03.003

Ziegler, D. S., Wright, R. D., Kesari, S., Lemieux, M. E., Tran, M. A., Jain, M., Zawel, L. and Kung, A. L. (2008). Resistance of human glioblastoma multiforme cells to growth factor inhibitors is overcome by blockade of inhibitor of apoptosis proteins. *J. Clin. Investig.* **118**, 3109-3122. doi:10.1172/JCI34120

Supplementary Information

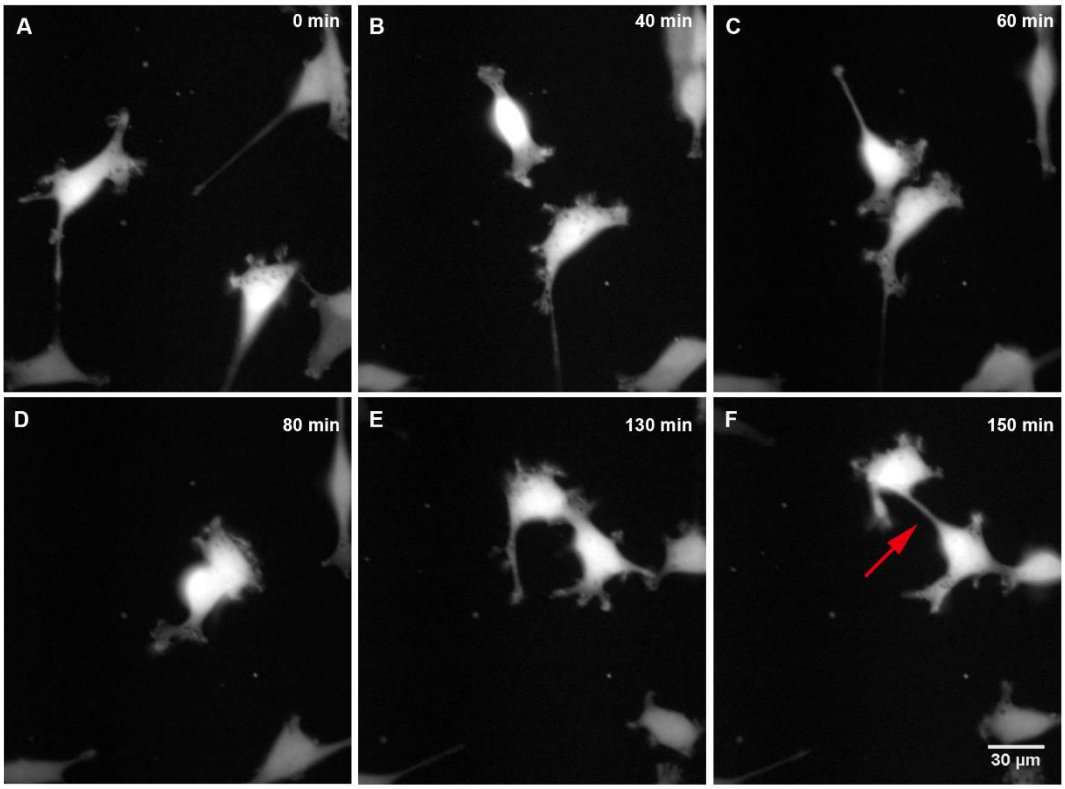

Figure S1. Frames of the formation of TMs following encounter of two GBM. *(A-F) A sequence of fluorescence images of U87 GBM cells labelled with mCherry forming TM. The red arrows in F point to a TM.*

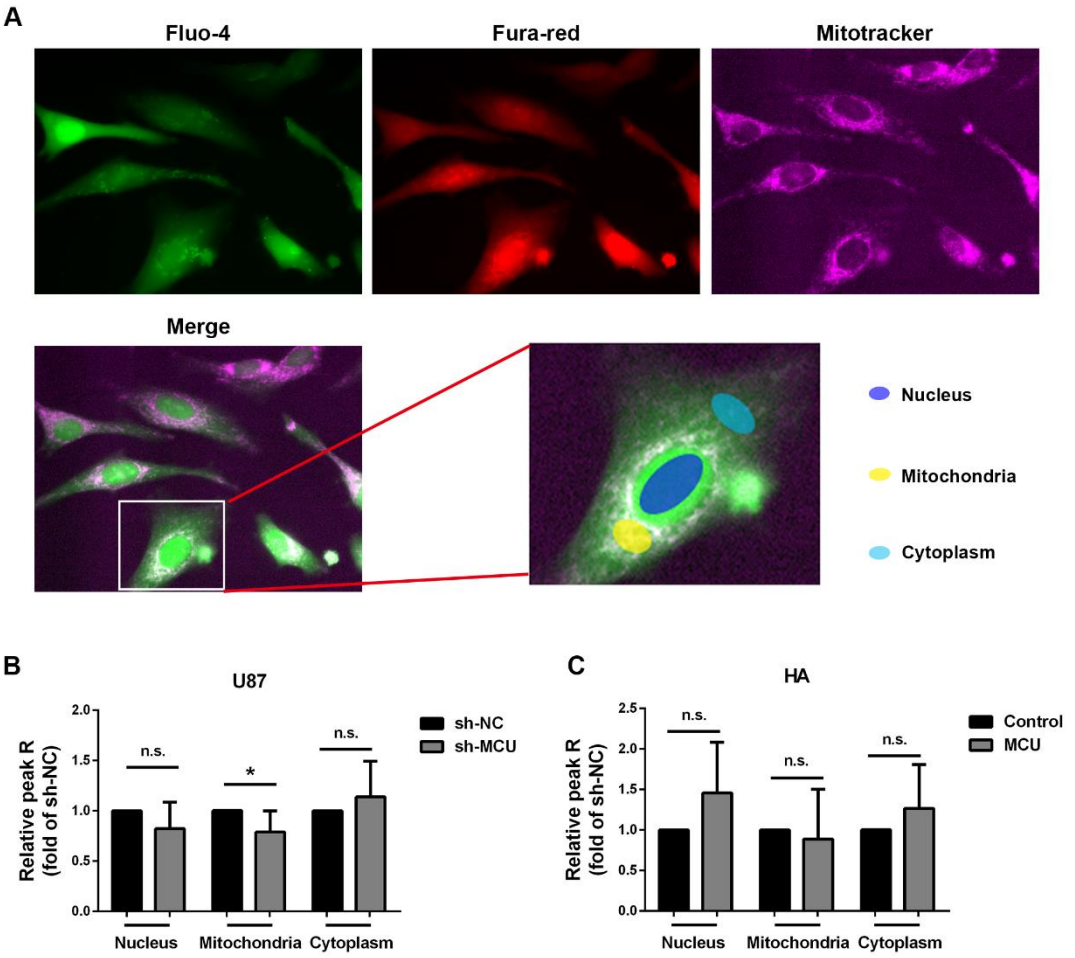

Figure S2. The effects of the MCU level on calcium levels of nucleus, mitochondria and cytoplasm in U87 GBM and HA cells. *(A) Cells were co-stained by Fluo-4, Fura-red and Mitotracker. Relative peak R from nucleus, mitochondria and cytoplasm in U87 GBM (B) and HA (C) after transfection for 48 hours. The nucleus was identified as the region corresponding to the dark hole visible following Mitotracker staining, mitocondria were identified as the bright regions following Mitotracker staining and the cytoplasm as the regions stained by Fluo-4 and Fura-red but with a low or absent staining of Mitotracker. The data are from three distinct experimental sessions and represent the mean ± SD. *p<0.05.*

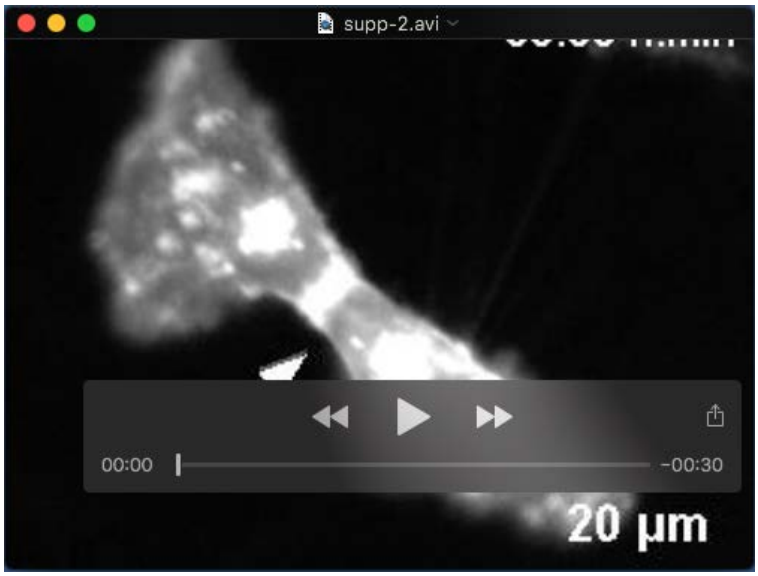

Movie 1. The formation of TMs following mitosis of Vybrant™ DiD labelled U87 GBM cells. *Images were acquired at 1 min interval and played at 10 frames per second. Scale bar = 20 µm, time shown in h:min. This video corresponds to Figure 2D.*

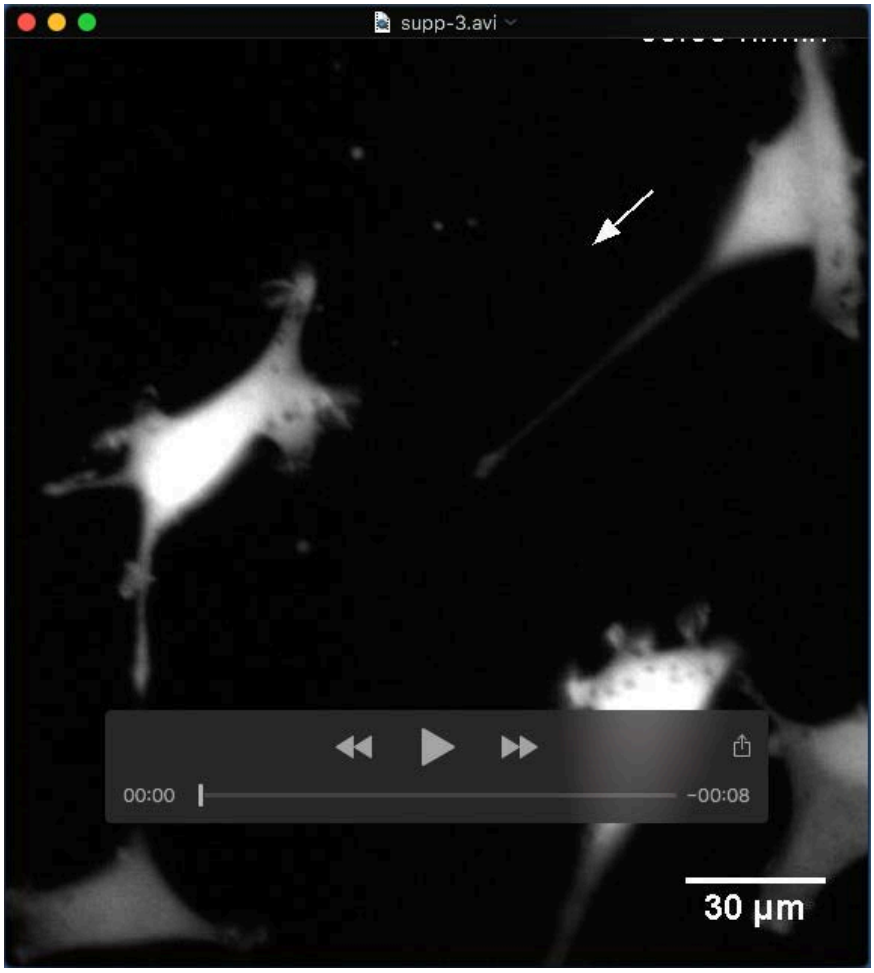

Movie 2. The formation of TMs following encounter of two U87 GBM cells labeled with mCherry by infecting with LV_Pgk1p-mCherry. *Images were acquired at 1 min interval and played at 20 frames per second. Scale bar = 30 µm, time shown in h:min. This video corresponds to Figure S1.*

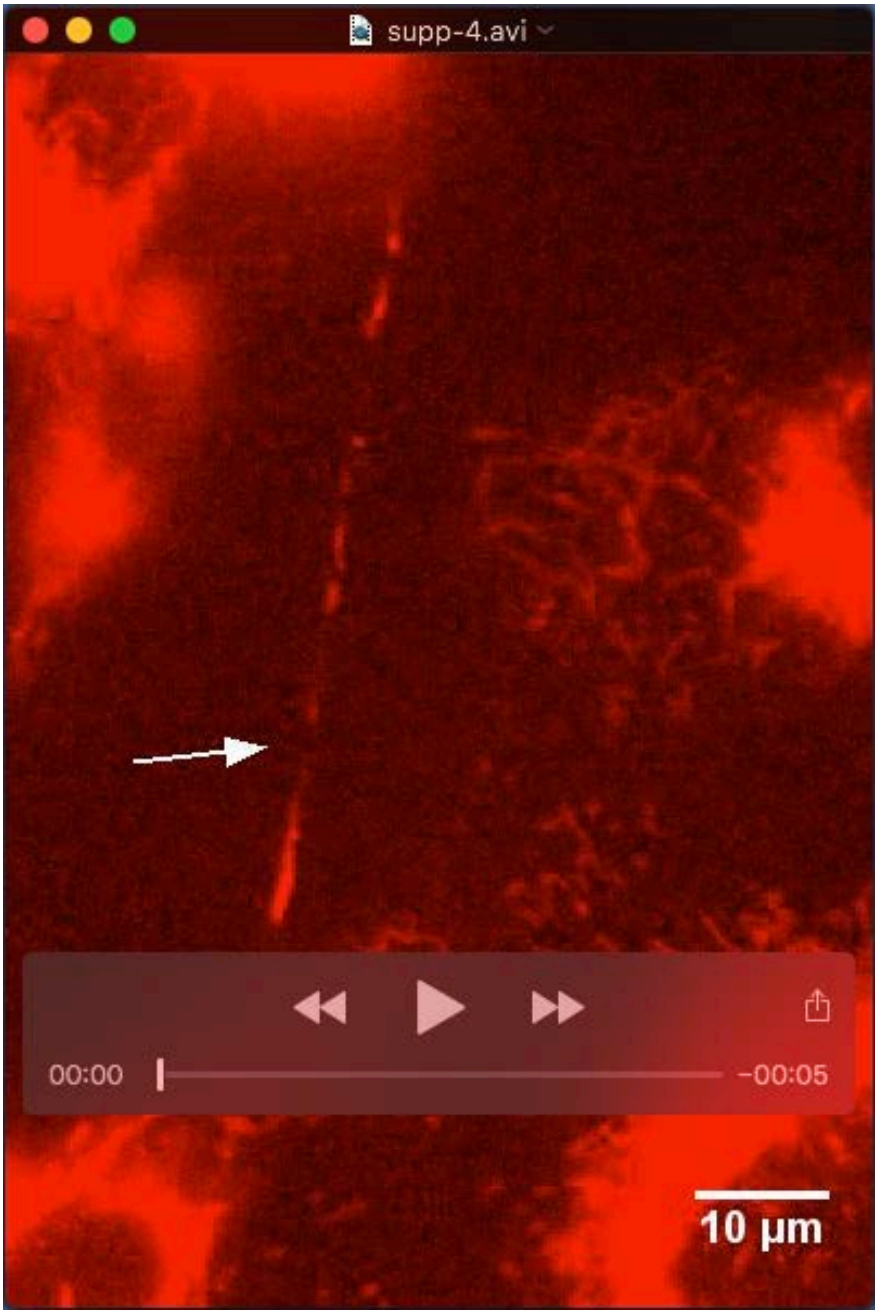

Movie 3. The motion of mitochondria in U87 GBM cells stained with MitoTracker. *Images were acquired at 30 s interval and played at 10 frames per second. This video corresponds to Figure 4F.*

Supplementary material

MCU silencing suppresses cell proliferation by arresting cell cycle progression

In our research published in Journal of Cell Science, MCU knockdown by shRNA in U87 GBM cells decreases calcium signal level (Fig. 8D) and proliferation (Fig. 8E) after 48 h treatment. In order to determine how MCU deletion affects cell proliferation via cell cycle progression, we carried out FACS analysis to detect DNA content in U87 GBM cells with and without MCU silencing. Simply, U87 GBM cells were transfected by a mix of lentiviral vector and pLKO.5-puro sh-MCU/pLKO.5-puro Non-Target shRNA. Cells were grown to confluence and maintained in a post-confluent state for 24 h, then split and plated in 6-well plates with a density of 10^6 cells per well. After cultured in growth medium (DMEM with 10% FBS) for the indicated times, the cells were harvested, fixed with 75% ice-cold ethanol overnight, stained with propidium iodide (PI, stock solution 50 μg/mL) and analysed in a Flow Cytometer (Thermofisher). At 0 h, the fractions of U87 GBM cells in G1 phase were similar no matter with or without MCU knockdown (Figure S3 A and B). 24 h after plated, 10% of MCU knockdown U87 GBM cells entered S phase compared to 17 % of U87 GBM cells without MCU knockdown (Figure S3 C and D). All these results suggest that MCU silencing impaired S phase entry of U87 GBM cells, and cells were arrested at the G1/S transition.

According to previous researches, mitochondria convert from isolated, fragmented elements into a hyper fused, giant network at G1/S transition [1], and progression to S phase is correlated with greater mitochondrial ATP production than any other cell cycle stage [1, 2]. Koval [3] and co-workers demonstrated that wild type fibroblasts showed cytosolic Ca^{2+} concentrations and mitochondrial Ca^{2+} uptake increased after release from growth arrest in parallel with a rise in oxygen consumption rate, but these changes did not occur in $MCU^{-/-}$ cells, which suggesting that MCU is required to adapt mitochondrial ATP production to energy demands during the cell cycle. In our research, MCU silencing induced mitochondrial Ca^{2+} decrease and cytosolic Ca^{2+} increase (as shown in Figure S2

B), which is consistent to Koval's results [3], suggesting that MCU knockdown decreases U87 GBM cells proliferation, one major hallmark of GBM malignancy, by reducing mitochondrial Ca^{2+} uptake, suppressing ATP production and arresting cell cycle progression.

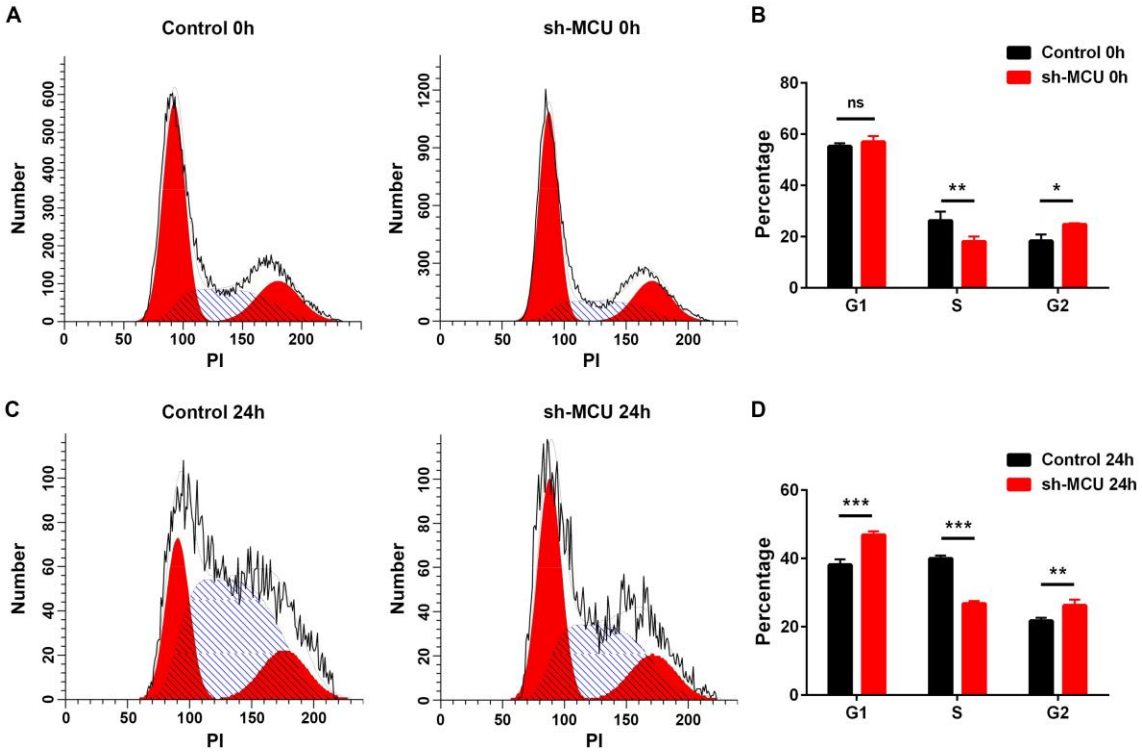

Figure S3. Downregulation of MCU in U87 GBM cells obstructs cell cycle progression by suppressing the G1/S transition. Representative FACS analysis for DNA content in U87 GBM cells at 0 h (A) and 24 h (C) post-plating. B and D, Cell cycle phase distribution of U87 GBM cells. The data are from three distinct experimental sessions and represent the mean±s.d., *P<0.05, **P<0.01, ***P<0.001 compared with control group.

Cyclin D1 is one of the members of cell cycle proteins whose characteristic is that the protein level changes dramatically throughout the cell cycle and is an essential regulator of the G1/S transition. Cyclin D1 forms an active complex with its interacting partner cyclin-dependent kinase 4 (CDK4), and this cyclin D1/CDK4 complex can phosphorylate the retinoblastoma protein (Rb) to disable

their function as transcriptional suppressors and allow activation of E2F-dependent transcription to promote S phase entry and transcriptional activation of genes that control cell cycle progression [4, 5]. Moreover, the cyclin E1 / CDK2 complex plays a similar role [6]. To determine whether cyclin D1 and cyclin E1 were involved in regulating the cell progression,leading to the decrease of cell proliferation in U87 GBM cells after MCU knockdown, we used qRT-PCR to quantify their mRNA expression levels, and the primer sequences were shown in Supplementary Table 1. Target gene expression was normalized to GAPDH expression as an internal standard and calculated as fold induction compared to controls.

Supplementary Table 1. Primer sequences used for qRT-PCR.

Gene	Forward primer (5′ to 3′)	Reverse primer (5′ to 3′)
MCU	TGTGCCCTCTGATGATGTTACAG	GTTCACGCCGGGATGGT
Cyclin D1	GCCCTCTGTGCCACAGATGT	GAAGCGTGTGAGGCGGTAGT
Cyclin E1	CCAGGAAGAGGAAGGCAAAC	CCTGTCGATTTTGGCCATTT
Cdc42	CGACCGCTGAGTTATCCACAA	TCTCAGGCACCCACTTTTCTTT
Rac1	AAGCTGACTCCCATCACCTATCCG	CGAGGGGCTGAGACATTTACAACA
GAPDH	GGGAAGGTGAAGGTCGGAGT	GGGGTCATTGATGGCAACA

After MCU silencing, the expression level of cyclin D1 decreased significantly (Figure S6 A), while cyclin E1 was not influenced too much (Figure S6 A), which suggests that cyclin D1 plays a role in MCU knockdown induced cell proliferation

reduction in U87 GBM cells. Previous researches proved silencing of cyclin D1 sensitized ovarian cancer cells to olaparib and induced cell cycle G1 arrest [7], which confirms the role cyclin D1 plays in cancer and inspires us new ideas in tumour treatment.

MCU silencing reduces cell migration

Another main hallmark of brain tumour malignancy is the high motility capacity of GBM cells, which facilitates metastasis and development of brain tumours, and increases the difficulty of complete surgical resection. We used the transwell assay to analyse the effect of MCU silencing on U87 GBM cell migration. Specifically, 5×10^5 U87 GBM cells in DMEM medium (without FBS) were seeded to the top chambers of 12-well transwell plates (Millipore; 8 μm pore size), and 10% FBS DMEM medium was added to the well. After 24 h of incubation, cells in the top of the chamber (non-migrating cells) were removed from the chambers, and cells in the bottom of the chamber (migrating cells) were fixed with 4% PFA for 20 min and stained with 5% crystal violet for 30 min in room temperature. The migrated cells were counted with a microscope, as shown in Figure S4 A and B, and the migrated cells reduced from 340 cells per field to 180 cells per field after MCU silencing in U87 GBM cells, with almost 50% reduction. According to our previous research, 24 h after MCU knockdown would not significantly suppress U87 GBM cell proliferation, but 48 h did. These results suggest that the reduction of migrated cells in 24 h is due to the repress of cell migration, but not due to cell proliferation inhibition.

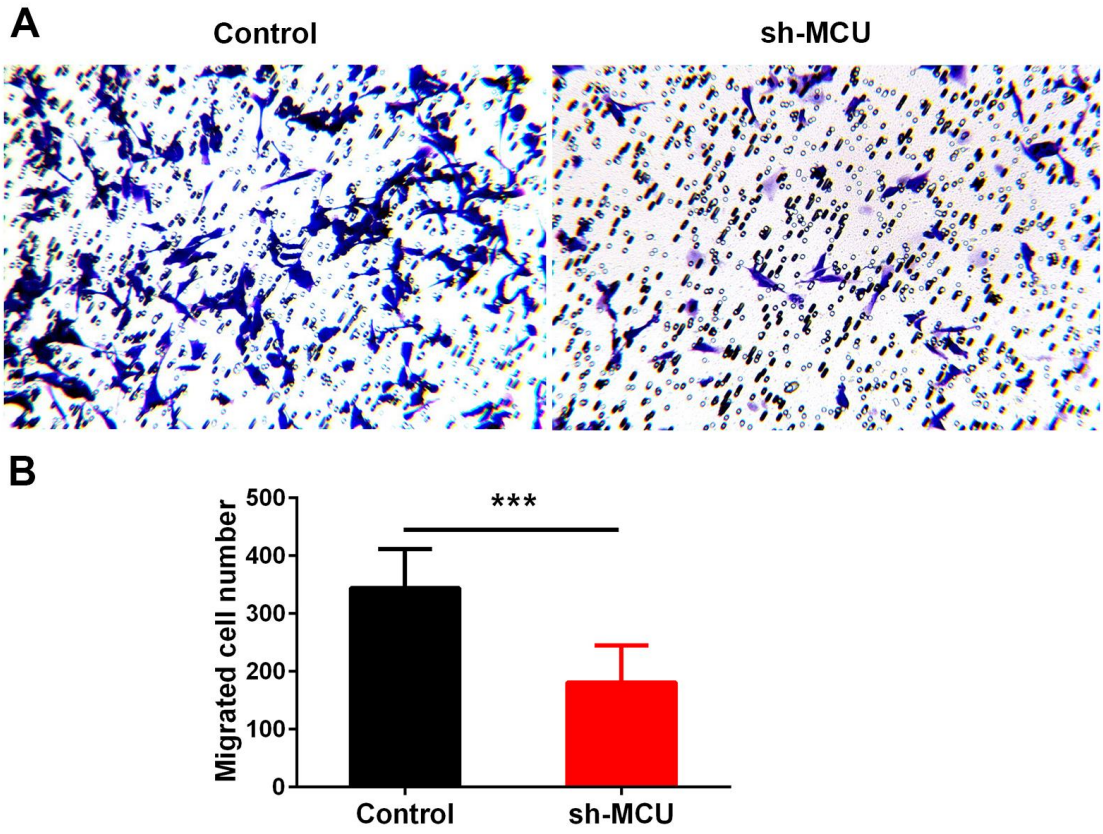

Figure S4. MCU silencing reduces transwell migration of U87 GBM cells. A, Representative images of transwell migration assay of U87 GBM cells with or without MCU silencing 24 h after seeding the cells. B, Graphical representation of migrated U87 GBM cells with or without MCU silencing, MCU silencing cells show reduction in transwell migration, compared to shRNA negative control. The data are from three distinct experimental sessions and represent the mean±s.d., ***P<0.001 compared with control group.

We also analysed cell motility with live-cell imaging setup. Simply, mCherry-labelled U87 GBM cells were transfected with sh-MCU/Non-Target shRNA. Live-cell imaging experiments were performed on an epi-fluorescence microscope (Olympus IX-83, Olympus) equipped with an imaging chamber incubator (Okolab, Pozzuoli, Italy) and LED illumination (λ=590 nm for mCherry). During all imaging

experiments, cells were kept at 37°C, 5.0% CO_2 and 95% humidity. Time-lapse images were taken with 500 ms of exposure time and one image per minute. The videos were analysed using the Fiji plugin TrackMate, which allows the selection of regions of interest (ROIs) for every cell and obtain the average velocities for each cell. We calculated shape descriptor circularity:

Circularity = 4π*area/perimeter^2;

For circularity, a value of 1.0 indicates a perfect circle. As the value approaches 0.0, it indicates an increasingly elongated shape.

The velocity of random motility of U87 GBM cells recorded with live-cell imaging was not significantly influenced after MCU knockdown (Figure S5A). The average cell areas for two groups of cells were similar, approximately 1300 um^2 (Figure S5B). However, circularity in wild type U87 GBM cells can reach a lower value compared with the cells with MCU knockdown (Figure S5C). This indicates U87 GBM cells tend to be rounder after MCU knockdown, sharp and fine structures degraded. In our transwell assay, the capacity of going through transwell chamber for U87 GBM cells decreased after MCU knockdown. The pore size is 8 μm, so if the cells want to pass, they need to squeeze the cell body. As shown in Figure S5D, wild type U87GBM cell can change its shape and squeeze its width from 20 μm (left panel) to 10 μm (right panel). When GBM cells invade surrounding tissues, invasive glioma cells alter the cell shape and volume in order to move through differently sized spaces, including the extremely small spaces in the normal brain [8]. So the capacity of changing the shape is beneficial to their invasion.

In situ studies of human glioma cells demonstrate that when injected into the brain, the vast majority (>85%) of glioma cells move into contact with a blood vessel even though the space is small [9]. And the recruitment of glioma cells to blood vessels occurs through bradykinin, which can bind to bradykinin two receptors (B2Rs), activates these G protein-coupled receptors (GPCRs) and causes inositol-1,4,5-trisphosphate receptor 3 (IP3R3)-dependent increases in

$[Ca^{2+}]_i$ in glioma cells [10]. The changes in $[Ca^{2+}]_i$ activate downstream ion channels that support cell shape and volume changes that are necessary for cell invasion.

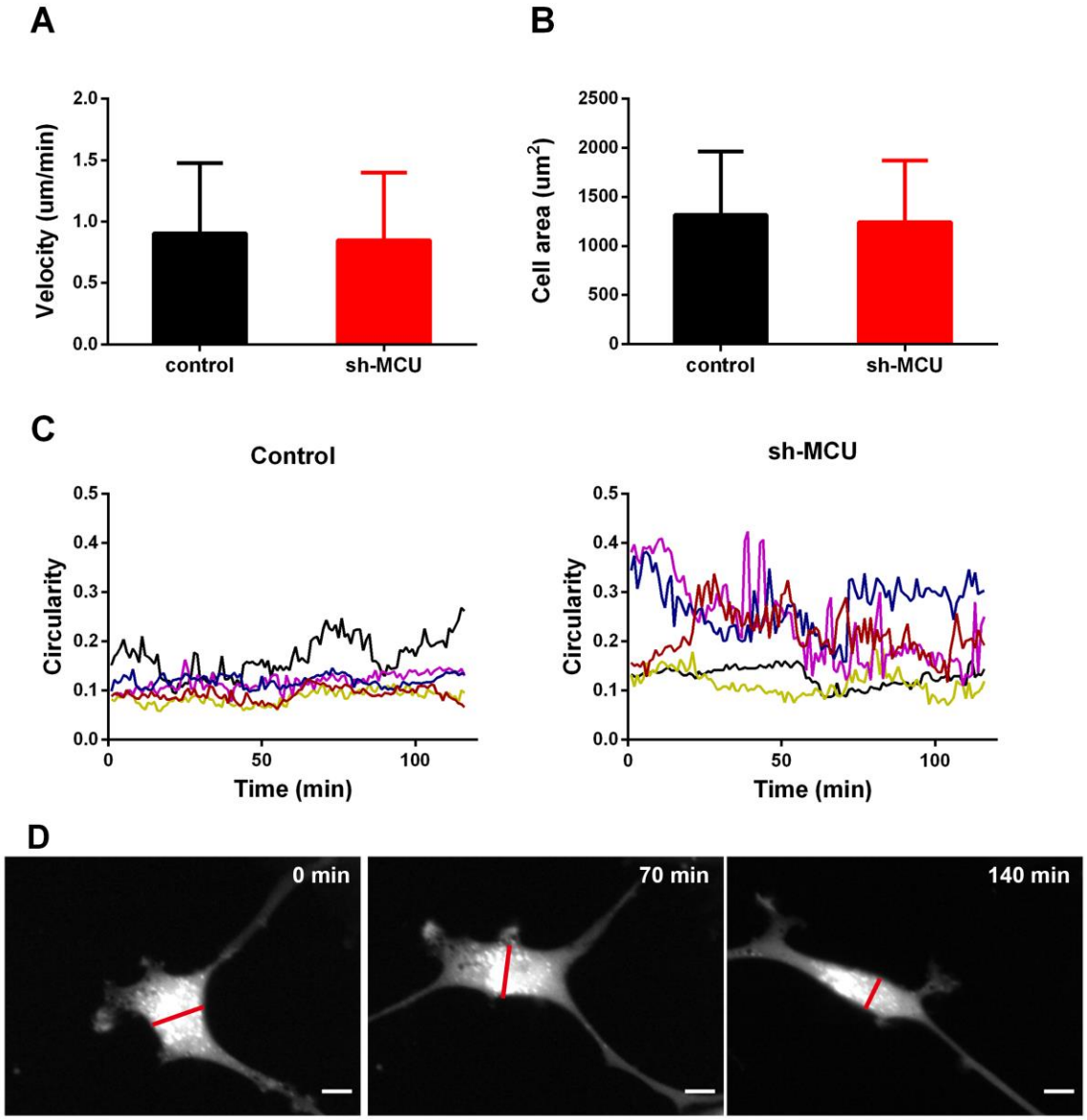

Figure S5. Effects of MCU silencing on velocity and shape of U87 GBM cells were analyzed with live-cell imaging. Velocity (A) and cell area (B) of U87 GBM cells were not significantly influenced. The data were from three distinct experimental sessions and represented the mean±s.d. C, Circularity can reach a lower value in U87 GBM cells without MCU

knockdown compared with that in sh-MCU cells. D, Cell shape changes over time. Scale bar: 10 μm.

Rho-family (Ras homolog) GTPases [11] are primary regulators of dynamic actin cytoskeletal assembly and rearrangement that are the basis for normal cell-cell adhesion, cell migration and even transformation. Ras-related C3 botulinum toxin substrate 1 (Rac1) and cell division control protein 42 (Cdc42) as the best-studied Rho family members have been proved to control cytoskeletal remodelling, including the formation and retraction of lamellipodia and filopodia, and regulate cell shape and cell mobility [12].

We hypothesized that MCU might play a role in regulating these two Rho GTPases and analysed gene expression levels of Rac1 and Cdc42 by qRT-PCR. As we discussed in Figure S4 A and B, for MCU downregulated U87 GBM cells, the transwell migration rate decreased significantly. Meanwhile, the mRNA expression level of Rac1 was reduced (Figure S6 B). It has been demonstrated that Rac1 depletion/inhibition in GBM cells disrupted the disassembly of cell adhesion concomitant with defects in the actin web and switched the proportion of stable cell adhesion complex, thus reduced cell motility [13]. However, the gene expression level of Cdc42 was not significantly influenced in our research (Figure S6 B).

In previous research, Prudent's group [14] silenced MCU in the highly migrating breast cancer cell line and abolished the intact mitochondrial Ca^{2+} uptake, which deactivated Rac1 and RhoA, as a consequence, induced cytoskeleton stiffness, focal adhesion dynamics and cell migration defects, which is consistent to what we have observed in U87 GBM cells. On the other hand, mitochondrial Ca^{2+} entry through MCU can stimulate increased ATP production. Wu and colleagues [15] demonstrated that MCU was essential for rapidly increasing mitochondrial Ca^{2+} in pacemaker cells, and MCU enhanced ATP production was required in a specific subcellular compartment prior to each heartbeat. In these cases, site-

specific productions of ATP may be required for Actin cytoskeleton remodelling during cell migration.

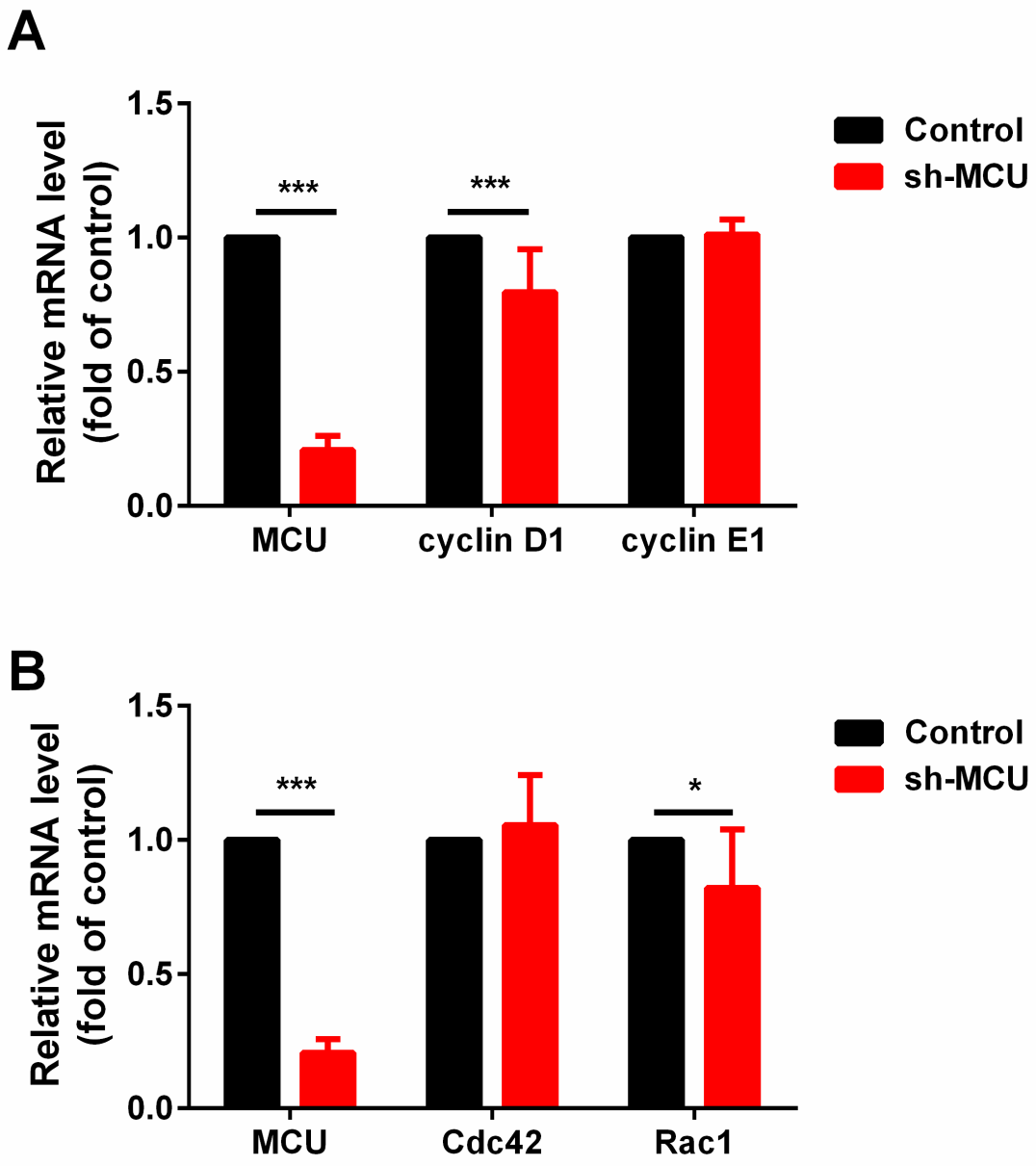

Figure S6. Effect of MCU silencing on cell proliferation and migration-related pathways in U87 GBM cells. A, qRT-PCR was used to detect mRNA expression levels of cell proliferation-related pathways cyclin D1 and cyclin E1. B, qRT-PCR was used to detect mRNA expression levels of cell

migration-related pathways Cdc42 and Rac1. The data are from three distinct experimental sessions and represent the mean±s.d., *P<0.05, ***P<0.001 compared with control group.

These results indicate that MCU silencing decreased mitochondrial Ca^{2+} uptake in U87 GBM cells and repressed the two main GBM malignancy hallmarks: cell proliferation and migration. In conclusion, MCU silencing decreased U87 GBM cell proliferation by arresting cells in the G1 phase with cyclin D1 downregulated and reduced the capacity of cell motility by influencing Rac1. MCU showed an increased expression level in GBM cells compared with that in healthy human astrocyte, to develop reagents and gene treatment methods targeting on MCU may supply a new direction in the overcoming the lethal brain tumours.

Reference

1. K. Mitra, C. Wunder, B. Roysam, et al., *A hyperfused mitochondrial state achieved at G1-S regulates cyclin E buildup and entry into S phase.* Proc Natl Acad Sci U S A, 2009. **106**(29): p. 11960-11965.

2. C. Montemurro, S. Vadrevu, T. Gurlo, et al., *Cell cycle-related metabolism and mitochondrial dynamics in a replication-competent pancreatic beta-cell line.* Cell Cycle, 2017. **16**(21): p. 2086-2099.

3. O.M. Koval, E.K. Nguyen, V. Santhana, et al., *Loss of MCU prevents mitochondrial fusion in G1-S phase and blocks cell cycle progression and proliferation.* Sci Signal, 2019. **12**(579).

4. C.J. Sherr and J.M. Roberts, *CDK inhibitors: positive and negative regulators of G1-phase progression.* Genes Dev, 1999. **13**(12): p. 1501-1512.

5. J.Y. Kato and C.J. Sherr, *Inhibition of granulocyte differentiation by G1 cyclins D2 and D3 but not D1.* Proc Natl Acad Sci U S A, 1993. **90**(24): p. 11513-11517.

6. R. Sonntag, N. Giebeler, Y.A. Nevzorova, et al., *Cyclin E1 and cyclin-dependent kinase 2 are critical for initiation, but not for progression of hepatocellular carcinoma.* Proc Natl Acad Sci U S A, 2018. **115**(37): p. 9282-9287.

7. Q. Zhong, Z. Hu, Q. Li, et al., *Cyclin D1 silencing impairs DNA double strand break repair, sensitizes BRCA1 wildtype ovarian cancer cells to olaparib.* Gynecol Oncol, 2019. **152**(1): p. 157-165.

8. V.A. Cuddapah, S. Robel, S. Watkins, et al., *A neurocentric perspective on glioma invasion.* Nat Rev Neurosci, 2014. **15**(7): p. 455-465.

9. V. Montana and H. Sontheimer, *Bradykinin promotes the chemotactic invasion of primary brain tumors.* J Neurosci, 2011. **31**(13): p. 4858-4867.

10. S.S. Kang, K.S. Han, B.M. Ku, et al., *Caffeine-mediated inhibition of calcium release channel inositol 1,4,5-trisphosphate receptor subtype 3 blocks glioblastoma invasion and extends survival.* Cancer Res, 2010. **70**(3): p. 1173-1183.

11. Y. Guo, S.R. Kenney, C.Y. Muller, et al., *R-Ketorolac Targets Cdc42 and Rac1 and Alters Ovarian Cancer Cell Behaviors Critical for Invasion and Metastasis.* Mol Cancer Ther, 2015. **14**(10): p. 2215-2227.

12. X. Chi, S. Wang, Y. Huang, et al., *Roles of rho GTPases in intracellular transport and cellular transformation.* Int J Mol Sci, 2013. **14**(4): p. 7089-7108.

13. J. Xu, N. Galvanetto, J. Nie, et al., *Rac1 Promotes Cell Motility by Controlling Cell Mechanics in Human Glioblastoma.* Cancers (Basel), 2020. **12**(6).

14. J. Prudent, N. Popgeorgiev, R. Gadet, et al., *Mitochondrial Ca(2+) uptake controls actin cytoskeleton dynamics during cell migration.* Sci Rep, 2016. **6**: p. 36570.

15. Y. Wu, T.P. Rasmussen, O.M. Koval, et al., *The mitochondrial uniporter controls fight or flight heart rate increases.* Nat Commun, 2015. **6**: p. 6081.

3.2 A Fully 3D Interconnected Graphene–Carbon Nanotube Web Allows the Study of Glioma Infiltration in Bioengineered 3D Cortex-Like Networks

Miao Xiao[#], Xiaoyun Li[#], Qin Song, Qi Zhang, Marco Lazzarino, Guosheng Cheng,* Francesco Paolo Ulloa Severino,* and Vincent Torre*

Advanced Materials

ADVANCED MATERIALS
www.advmat.de

A Fully 3D Interconnected Graphene–Carbon Nanotube Web Allows the Study of Glioma Infiltration in Bioengineered 3D Cortex-Like Networks

Miao Xiao, Xiaoyun Li, Qin Song, Qi Zhang, Marco Lazzarino, Guosheng Cheng, Francesco Paolo Ulloa Severino,* and Vincent Torre**

Currently available 3D assemblies based on carbon nanotubes (CNTs) lag far behind their 2D CNT-based bricks and require major improvements for biological applications. By using Fe nanoparticles confined to the interlamination of graphite as catalyst, a fully 3D interconnected CNT web is obtained through the pores of graphene foam (GCNT web) by in situ chemical vapor deposition. This 3D GCNT web has a thickness up to 1.5 mm and a completely geometric, mechanical and electrical interconnectivity. Dissociated cortical cells cultured inside the GCNT web form a functional 3D cortex-like network exhibiting a spontaneous electrical activity that is closer to what is observed in vivo. By coculturing and fluorescently labeling glioma and healthy cortical cells with different colors, a new in vitro model is obtained to investigate malignant glioma infiltration. This model allows the 3D trajectories and velocity distribution of individual infiltrating glioma to be reconstructed with an unprecedented precision. The model is cost effective and allows a quantitative and rigorous screening of anticancer drugs. The fully 3D interconnected GCNT web is biocompatible and is an ideal tool to study 3D biological processes in vitro representing a pivotal step toward precise and personalized medicine.

The brain is formed by an intricate assembly of cellular networks, where neurons are embedded in an extracellular matrix (ECM) consisting of a dense 3D mesh of proteins that provides complex chemical, electrical, and mechanical signaling.[1] Given this complexity as well as the limitations of in vivo studies,[2] it is important to develop in vitro models able to recapitulate the brain connectivity at various levels and, ultimately, provide a mimic of the human brain suitable for preclinical applications.[3] Toward this goal, several 3D supporting materials or scaffolds have been developed, tested, and applied.[4] But further progress is needed: the combination of new materials with biotechnology can provide 3D tissue engineering with the tools to make a major step toward precise and personalized medicine.[5] Biomaterials from natural components,[6] such as collagen hyaluronic acid and Matrigel, have been widely used for 3D cultures. However, scaffolds made of synthetic materials, such as poly(lactic-*co*-glycolic acid) and others, exhibit better long-term performance.[7] Emerging carbon-based materials, especially carbon nanotubes (CNTs)[8] have been widely utilized to produce scaffolds with improved mechanical strength and conductivity.[9] CNTs with their 1D hollow structure and good

Dr. M. Xiao, Dr. X. Li, Dr. Q. Song, Prof. V. Torre
International School for Advanced Studies (SISSA)
via Bonomea 265, Trieste 34136, Italy
E-mail: torre@sissa.it
Dr. M. Xiao, Prof. V. Torre
Joint Laboratory of Biophysics and Translational Medicine
ISM-SISSA
Suzhou Industrial Park, Jiangsu 215123, China
Dr. Q. Song, Prof. V. Torre
Cixi Institute of Biomedical Engineering
Ningbo Institute of Materials Technology and Engineering
Chinese Academy of Sciences
Zhejiang 315201, China
Dr. Q. Song
School of Pharmaceutical Engineering
Zhejiang Pharmaceutical College
Ningbo, Zhejiang 315100, China
The ORCID identification number(s) for the author(s) of this article can be found under https://doi.org/10.1002/adma.201806132.

DOI: 10.1002/adma.201806132

Prof. Q. Zhang
School for Radiological and Interdisciplinary Sciences (RAD-X)
and Collaborative Innovation Center of Radiation Medicine of Jiangsu
Higher Education Institutions
Medical College of Soochow University
Suzhou Industrial Park, Suzhou, Jiangsu 215123, China
Dr. M. Lazzarino
IOM-CNR
Area Science Park, Basovizza, Trieste 34149, Italy
Prof. G. Cheng
CAS Key Laboratory of Nano-Bio Interface
Suzhou Institute of Nano-Tech and Nano-Bionics
Chinese Academy of Sciences
398 Ruoshui Road, Suzhou Industrial Park, Jiangsu 215123, China
E-mail: gscheng2006@sinano.ac.cn
Dr. F. P. Ulloa Severino
Cell Biology Department
Duke University Medical Center
335 Nanaline Duke Building Duke University Medical Center
Durham, NC 27710, USA
E-mail: francesco.ulloa@duke.edu

electrical properties allow intensive interactions with and among cells, which boost electrical signaling,[10] modulate neuronal growth,[11] and guide the functional reconnection of segregated spinal cord slices.[4c] Different kinds of assemblies based on CNTs have been realized for a variety of applications (Figure S1a–c, Supporting Information). In terms of biological applications, 2D CNT-based bricks such as forests of vertically aligned CNTs,[12] films of CNT building blocks,[9b] and extended 2D meshes of CNT[13] have been deposited on different substrates to form dense blocks useful for several applications, but cells could not migrate into the deep layers of these CNT assemblies. On the other hand, CNTs embedded in hydrogel or porous organic structures[14] can host 3D cellular assemblies but do not have well-defined mechanical or electrical connections. Genuine 3D networks of CNTs have been produced by chemical infiltrating aqueous CNT dispersion into porous ceramic.[15] However, there is no additional crosslinking existing between the individual CNTs so that the electrical and mechanical connectivity is random and not fully controlled. Therefore, the first motivation of the present work is the development of a 3D web of CNTs with a fully geometric, electrical, and mechanical interconnectivity allowing the reconstruction of in vitro neuronal networks mimicking the in vivo brain connectivity which could be used for the screening of drugs against a variety of diseases,[16] such as malignant glioma infiltration.

Malignant glioma is composed of mutated glia cells that generate brain tumors.[17] The motility and ability of malignant glioma to migrate is at the basis of metastases in healthy brain regions. In terms of malignancy, malignant glioma kills 94.5% of patients within 5 years after diagnosis.[18] Malignant glioma uses different roots to infiltrate the brain,[17,19] and its malignancy also stems from its ability to recover from surgical resection and its resistance to chemo and radio therapies.[20] At the moment, orthotopic models based on xenografts of malignant glioma cells on the whole brain of rats or mice are thought to be the best way to quantify malignant glioma infiltration. However, orthotopic models suffer from the use of immune-compromised animals and the obtained results could be affected also by species-differences.[21] Therefore, the second motivation of the present work is the development of in vitro models able to recapitulate the complex biology of malignant glioma infiltration.[22]

Graphene foams (GFs) have high mechanical rigidity, can reach more than one millimeter in height, and are biocompatible, promoting the differentiation of neural stem cells in neurons[23] and the synchronization of neuronal network activity.[4b] However, GFs have large pores ranging from 100 to 300 µm in diameter.[24] Consequently, the cellular assemblies that grow inside them are not dense.[24] To combine the advantages of both GF and CNTs, we constructed a hybrid scaffold made by graphene foam in situ growing carbon nanotubes to fill the pores.

A summary of the process for the fabrication of 3D CNT web through the pores of graphene foam (GCNT web) is illustrated in **Figure 1**a. Commercial 3D porous nickel foam[25] was used to prepare 3D GFs with a chemical vapor deposition (CVD) system. CH_4 molecules was heated to 950 °C diffused into the Ni lattice and released carbon atoms that subsequently precipitated as graphene on the Ni surface during the cooling process.[26] Then, the 3D graphene/nickel foam was used to support the in situ growth of CNTs. Iron nanoparticles were confined to the interlamination of graphite using the intercalated $FeCl_3$–graphite compound[27] as a catalyst during CNT growth. The catalyst was loaded upstream of the vapor flow, beside the graphene/nickel foam (Figure 1a, left panel). The CVD chamber was first heated to 1050 °C and was protected with a stream of Ar so that $FeCl_3$ evaporated and the Fe atoms were captured by the GF. Afterward, the CNTs grew in situ on

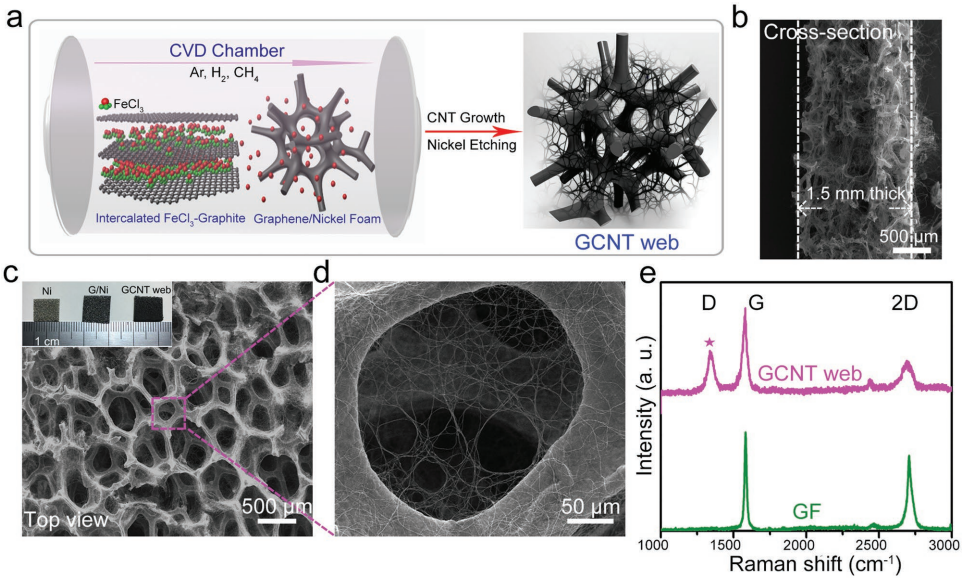

Figure 1. The fabrication and physical properties of GCNT web. a) Schematic illustration of the procedure for the in situ growth of CNTs inside GF scaffold. b) Representative SEM image of the GCNT web from the cross-section. c,d) Representative SEM images of the GCNT web with low- and high-magnification of the CNT web from the top view (inset: the optical images of porous nickel, graphene/nickel foam, and GCNT web). e) Typical Raman spectra acquired on the GF (green) and the GCNT web (magenta).

the surface of the graphene skeleton under an appropriate ratio of CH_4 and H_2, which formed a monolithic graphene–CNT hybrid with microscale graphene skeletons and a 3D nanoscale CNT web inside. The GCNT web was finally obtained after wet etching of the Ni template (Figure 1a, right). The CNTs adhered well onto the GF even after having been exposed to ultrasound at 150 W for 30 min. The optical images of porous nickel, graphene/nickel foam, and GCNT web (Figure 1c, inset) indicated highly functional structures. Scanning electron microscopy (SEM) images showed that the GCNT web presented a fully interconnected structure, where the CNTs filled up the pores of the GF, creating a web (Figure 1c) with a variable pore size distribution, ranging from hundreds of nanometers to tens of micrometers (Figure 1d). Moreover, the SEM image from the cross-section of the GCNT web presented a genuine 3D CNT interconnectivity along the *z*-direction and the GCNT web thickness could reach 1.5 mm according to the Ni template (Figure 1b). Compared to the previous GF scaffolds, these new GCNT web have a higher modulus of elasticity and conductivity (Figure S2a,b, Supporting Information), which are beneficial for neuronal proliferation, migration, and differentiation.[28] Raman spectra (Figure 1e) acquired on GF (green trace) and GCNT web (magenta trace) presented few-layer graphene and CNTs features identified as three characteristic peaks.[29] Besides, the spectrum of GF showed a strongly suppressed defect-related D band, indicating an overall high quality of graphene. The D peak (≈1348 cm^{-1}) associated with sp^3-hybridized carbon atoms showed disordered carbon atoms and was attributed to the presence of CNTs.[30] To the best of our knowledge, this is the first time that GFs with CNTs filling the pores have been successfully realized. Reported graphene–CNT hybrids either have a dense CNT mesh grown coaxially around the GF skeleton[31] or have thin nanoneedles on the surface of the GF skeleton.[32] These processes improve the surface area-to-volume ratio and enrich the skeleton surface topology, but they do not provide a strong interconnectivity between CNTs. If compared to the previous assemblies based on CNTs (Figure S1a–c, Supporting Information), the GCNT web represents for the first time a genuine 3D monolithic CNT web with a fully interconnected structure leaving inner spaces between CNTs from hundreds of nanometers to tens of micrometers, which match the biological dimensions. The productive growth of CNTs allows highly crosslinked nanotubes to form fully geometric and mechanical interconnectivity. Because of the interconnected graphene skeleton and the in situ growth of CNTs, the CNT web also has a strong electrical connectivity.

The 3D GCNT web offers neuronal culture compatibility, where the dense CNT web provides the physical support to guide neuronal growth in a genuine 3D manner that is not restricted to a 2D flat culture. Confocal images of cortical cultures stained with phalloidin, an actin marker, and Hoechst, a nuclear marker, show that neurons grew primarily on the skeleton of GF (Figure S3c, Supporting Information) and developed in 3D following the skeleton's topology. In contrast, neurons grown inside the GCNT web formed a denser network (**Figure 2**b), extending along the CNT web and filling the GF pores. SEM imaging of these cultures show that neurons pervaded the CNTs and that neurite outgrowth was guided by the overall CNT orientation (Figure 2c). The staining of neuronal axons and dendrites using SMI_312 and MAP2 as markers shows that neurons extended both axons and dendrites in all directions, developing a dense 3D network reminiscent of a native neural tissue (Figure 2a and Movie S1, Supporting Information).

The staining of axons with SMI_312 from a cross-section of the GCNT web shows the formation of a neuronal network (Figure 2f) extending up to 635 micrometers indicating that neurons penetrate through the entire 3D GCNT web. In addition, the almost uniform staining along the *z*-axis for several hundred of micrometers (Figure 2g) proves that we have a 3D neuronal network with a homogeneous density and there is no major difference between shallow and deeper layers. The same conclusion is obtained by SEM cross-section views of GCNT web (Figure 2h) showing cortical cells embedded over the entire *z*-axis. More interesting, the cortical cells could not only grow along the CNTs but also twine around the CNTs (Figure 2h, inset). The lower porosity of the GCNT web enables the retention of a larger number of neurons and glia inside the GCNT web, better mimicking the in vivo situation. After 8 d in culture (DIV 8), the nuclei count showed a fourfold increase in cell density in GCNT web compared to GFs (Figure 2d). A morphometric analysis using confocal microscopy indicated that the average volume occupied by every single cell on the GCNT web was 50% higher than that observed on GFs (Figure 2e).

Calcium plays a critical role in regulating neuronal network activities by participating in the synaptic transmission between neurons, controlling vesicle release.[33] To investigate whether neurons grown in the 3D GCNT web are alive and functionally active, we performed calcium imaging experiments using the calcium indicator Fluo-4 AM as previously described.[4b] Fluorescent images showed clear bright spots associated with the cell body of neurons and glia (Figure S4a, Supporting Information), which were located on the graphene skeleton but were also seen as suspended inside CNT web pores. Spontaneous calcium transients (DF/F) associated with the electrical firing of neurons were obtained by acquiring images at 3–5 Hz for 10–20 min (Movie S2, Supporting Information). At DIV 8, synchronous calcium transients with an amplitude of up to 1.5 DF/F were observed (Figure 2i); they had a sharp rising phase and a relatively slower decline, similar to the transients obtained from spiking neurons but not those from glial cell bodies (Figure S4b, Supporting Information). At DIV 15 (Figure 2j), calcium transients had a lower degree of synchrony, as shown by the raster plots (Figure 2m) and crosscorrelation matrices (Figure 2n). Similar results were also observed on GF scaffolds[4] (Figure S5, Supporting Information). During the early stages of development, specifically from DIV 2 to 4, the neuronal networks had a very low level of activity on both the GF and GCNT web. At DIV 6, the frequency and mean correlation coefficient (Figure S5f,g, Supporting Information) had a threefold increase and further increased over time. The bursting rate of neuronal growth inside the GCNT web was always higher than that of the growth on GF (Figure S5f, Supporting Information), even after DIV 15. A significant increase in burst frequency could be seen after DIV 15 inside the GCNT web (Figure 2k). Cortical networks grown inside the GCNT web at DIV 8 also showed a higher degree of synchrony than those grown inside the GF. As expected from the dynamics of the cortical network in vivo,[34]

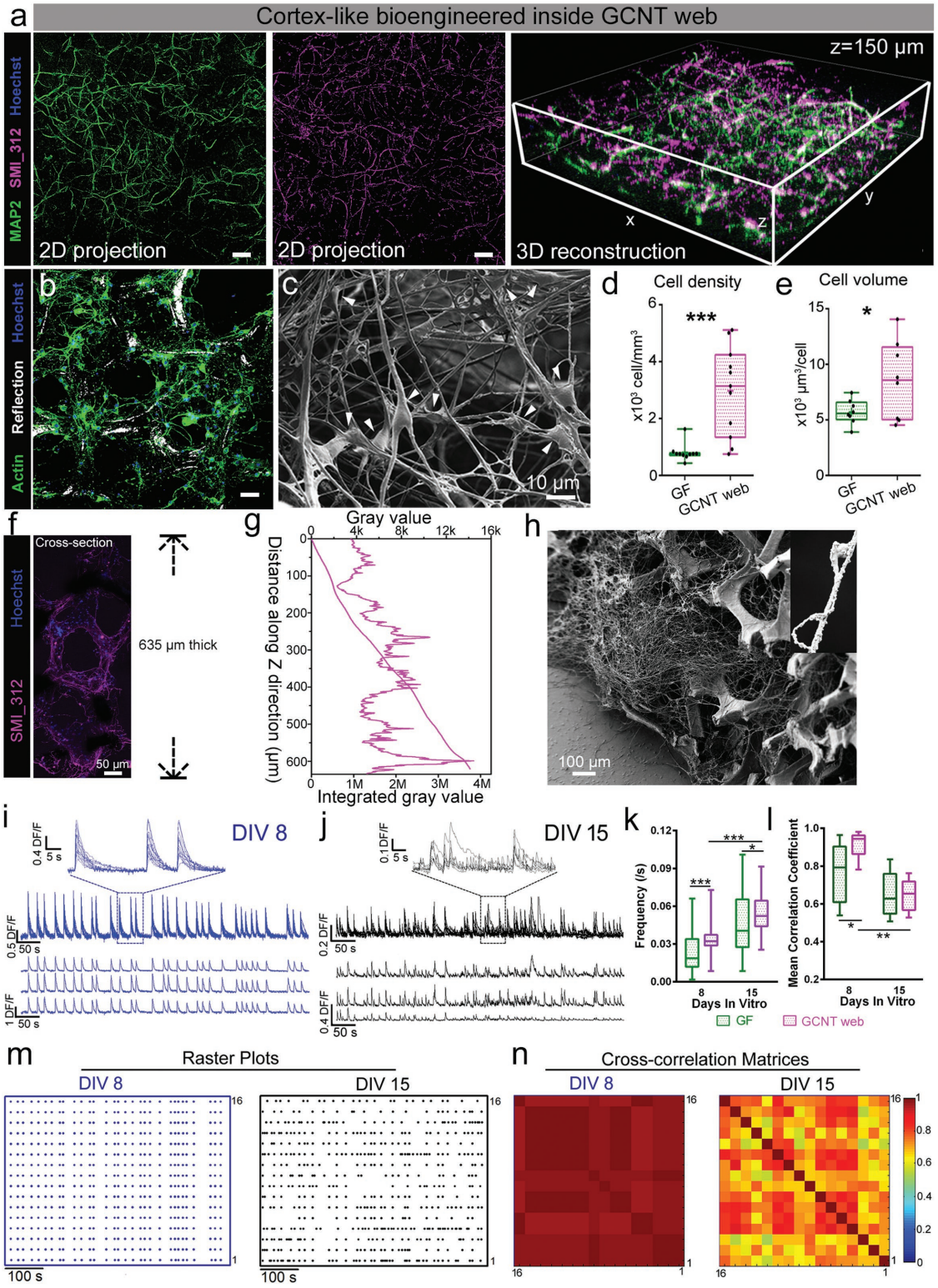

Figure 2. 3D functional cortex-like network is bioengineered inside 3D GCNT web. a) Representative staining for neurites (with MAP2, left) and axons (with SMI_312, middle) inside GCNT web after 8 d of culture and 3D reconstruction of the neuronal network (right). b) Actin staining of cortical cells after 8 d of culture inside the GCNT web. c) SEM images of cortical cells (white arrow heads) trapped into CNTs web. d) Box plot of cell density for cortical cultures grown inside the GCNT web and GF scaffolds (Unpaired t-test; $n = 10$ and $n = 11$, respectively). e) Box plot of occupied volume by cortical cells grown inside the GCNT web and GF scaffolds (Unpaired t-test; $n = 8$ for both the GF and GCNT web). f) Staining of axons (with SMI_312) acquired from a cross-section of the GCNT web along the *z*-direction. Scale bar = 50 µm. g) The overall intensity distribution of the axon staining along the *z*-axis. h) SEM image of the GCNT web embedded with cortical cells acquired from the cross-section (inset: a cortical cell twined around a CNT).

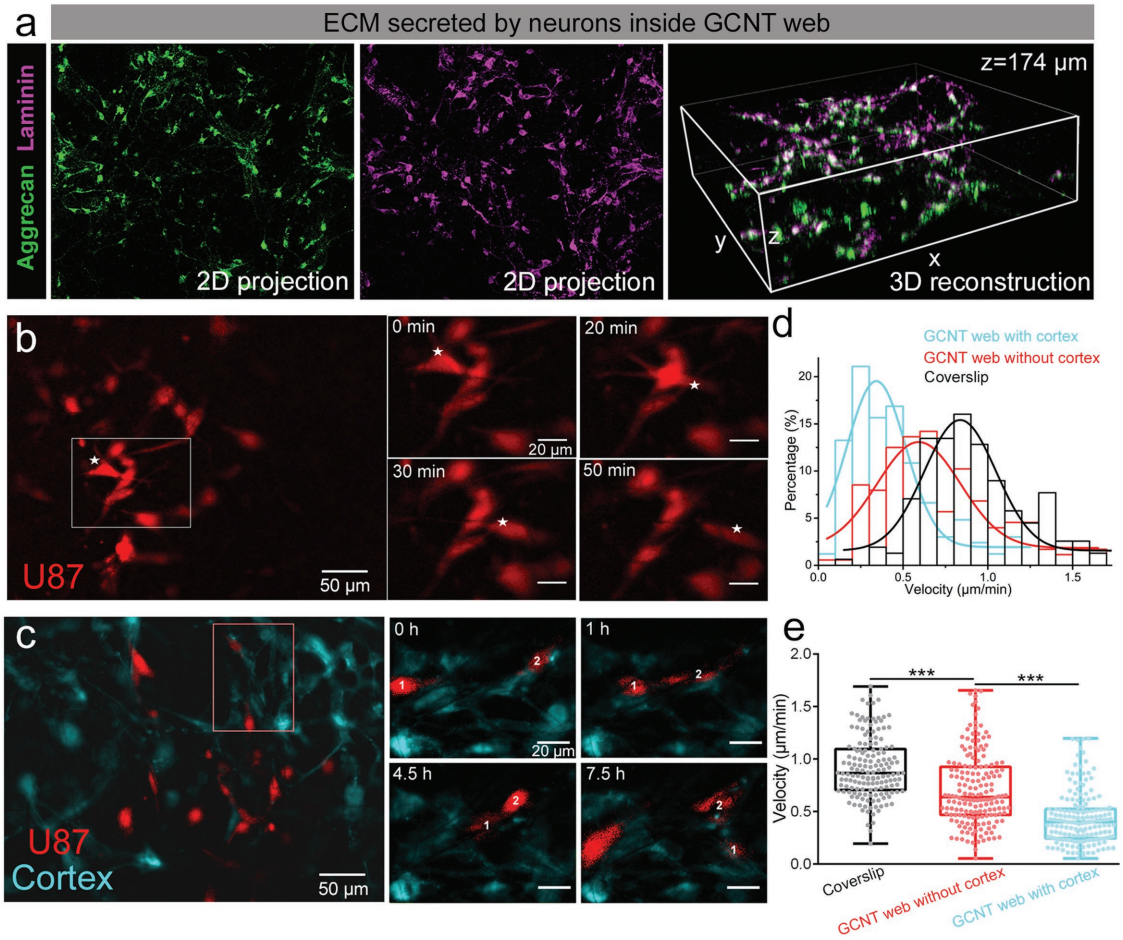

Figure 3. a) Staining for aggrecan and laminin proteins secreted by neurons cultured inside 3D GCNT web. b) An example of fluorescently labeled U87MG cells seeded inside the GCNT web. c) A representative live cell imaging experiment with fluorescently labeled U87MG cells (in red) and cortical cells (in cyan) obtained at different times. d,e) Cell velocity distribution and average velocities of malignant glioma cultured on coverslip ($n = 156$ cells), the GCNT web ($n = 176$ cells), and the cortex-like network ($n = 171$ cells, unpaired t-test).

after 15 DIV, the degree of synchrony decreased in networks cultured inside the GF and GCNT web (Figure 2l). Therefore, cortical cells inside the GCNT web grow in all directions to form through-space connectivity and functional properties that resemble the synchronized dynamical activity of in vivo networks.[34] In contrast to conventional GF and CNT scaffolds, the 3D GCNT web provides an appropriate microenvironment for neuronal network formation, such as neuron anchoring, cellular compartments, and cortical mechanical properties. Considering the brain complexity, our fully 3D interconnected GCNT web presents a major improvement for the study of the physiological and pathological processes in the brain.

An essential component of all 3D cellular assemblies is the ECM, which has the role of orchestrating the interactions between individual cells and the surrounding microenvironment.[35] The ECM is formed by different kinds of secreted molecules arranged in a 3D mesh and is not easily revealed in in vitro investigations with typical flat dishes. ECM proteins are important for retaining the network connectivity of a mature neuronal network[36] and constitute the matrix through which brain tumors, such as malignant glioma, travel to invade brain regions.[37] To verify whether cortical cells cultured on GCNT web secrete and produce the proteins forming the ECM, we stained the 3D coculture with standard markers for aggrecan and laminin. Aggrecan is an important protein specifically secreted by neurons that forms the perineuronal net,[38] whereas laminin is a key component of the basal lamina, which influences adhesion, migration, differentiation and survival.[39] Confocal images of neurons stained with specific antibodies against aggrecan and laminin (**Figure 3**a and Figure S6a, Supporting Information)

i,j) Superimposed optical traces (three of them are shown separately at the bottom) obtained from neuronal cultures grown inside the GCNT web at DIV 8 and 15. k) Comparison of the frequency inside the GF and GCNT web at DIV 8 and 15 ($n = 8$ for GF, $n = 10$ for GCNT web at DIV 8; $n = 6$ for GF, $n = 6$ for GCNT web at DIV 15). l) Comparison of the crosscorrelation at DIV 8 and 15 ($n = 8$ for GF and GCNT web at DIV 8; $n = 6$ for GF and $n = 5$ for GCNT web at DIV 15; two-way analysis of variance (ANOVA), Sidak's test). m) Representative raster plot of the peaks of calcium transients from cortical cultures grown inside the GCNT web at DIV 8 obtained from 16 different neurons. n) Representative crosscorrelation matrices of calcium transients from neuronal networks cultured inside the GCNT web at DIV 8 and 15.

show a rich presence of the two proteins inside the GF and GCNT web, but the ratio between aggrecan and laminin on the GCNT web (73.5 ± 4.2%) is lower than that on GF (97.0 ± 5.5%) (Figure S6c, Supporting Information). A 3D reconstruction from serial images taken with confocal microscope allows us to visualize the 3D organization of the ECM (Figure 3a and Figure S6b, Supporting Information). We found that the degree of colocalization of aggrecan and laminin was higher inside the GCNT web than inside the GF (Figure S6d, Supporting Information), indicating that colocalization in 2D and 3D is different. The 3D GCNT web can provide an exact 3D visualization of the ECM secreted by different cells, particularly by brain cancer cells, and can resolve the fine mechanical details of cell motility. In this way, it will be possible to link the mechanical and chemical abnormalities of the ECM to brain cancer invasion.

The basic mechanisms of cell motion on 2D flat culture are generally understood, and several methods have been developed to visualize and analyze cell migration in 2D. Nevertheless, in vivo cells grown in a 3D environment can follow different migration strategies, and 2D cultures cannot adequately replicate the complex in vivo tumor microenvironment; therefore, 2D cultures are poor predictors of tumor cell behavior in vivo.[40] To gain detailed insights into glioma cells infiltration in an intact brain, experimental models that recapitulate the highly complex 3D in vivo environment are needed, and therefore, we cultured U87MG cells inside the GCNT web. U87MG cells were genetically labeled with the red fluorophore mCherry, and their 3D motion was investigated with 3D time-lapse imaging. In these experiments, we acquired a stack of 20 images with z-steps of 3 µm every 3 min. Glioma grown inside the GCNT web (Figure 3b and Movie S3, Supporting Information) moved rapidly, and in a time window of just 10 min, they could move over several micrometers. During their motion, they squeezed, modifying their shape (see the U87MG cells indicated by asterisks). From the acquired stack of images, we recovered the 3D trajectories (**Figure 4**a, left panel, and Figure S7a, Supporting Information) using the Fiji plugin TrackMate as previously described[41] over periods of time of up to 6–24 h. From these trajectories, the velocity of the movements along the x-, y-, and z-axes distribution and the velocity of the cells during this period were computed. A comparison of the velocity of glioma in 2D and in 3D (Figure 3d,e) showed that glioma moved with a lower velocity inside the GCNT web than on 2D flat dishes. Our 3D trajectories are very similar to those obtained with a recently proposed method based on label-free 3D single cell tracking.[42] Similarly to what we observed in human primary macrophages in 3D biometric matrices,[42] the migration velocity of U87MG cells along the z-axis is lower than the lateral velocity along the x and y-axes (Figure 4b,c).

Brain cancer infiltration occurs in a 3D environment composed of healthy cortical tissue, i.e., neurons, glia cells, blood vessels, and the ECM. Therefore, U87MG cells were cocultured with rat cortical cells, comprising both neurons and glia cells. Having verified that cortical cells grown inside the GCNT web produce ECM proteins, we compared glioma motility in the GCNT web and the GCNT-web-based cortex-like network. Before seeding inside the GCNT web, cortical cells were labeled with the fluorescent probe DiD, which intercalates in the lipid membranes. In this way, it was possible to distinguish red fluorescent U87MG cells from healthy cyan cortical cells (Figure 3c). Their motions were investigated by 3D time-lapse imaging, lasting from several hours up to 2 d. U87MG infiltrated the 3D network formed by neurons and glia cells, often sliding along the thin CNTs in a way reminiscent of what they do along blood vessels[17] in the intact brain (Movie S4, Supporting Information). U87MG moved much more than neurons and glia cells, which appeared to be stable. The presence of cortical cells significantly slows down the motion of glioma (Figure 3d,e).

Our data show that the migration velocity of malignant glioma cells depends on the environment where they are cultured; this velocity decreases inside the GCNT web, and it decreases even more when glioma cells are cocultured with cortical cells. The obvious question, therefore, is how different is the action of drugs on glioma migration inside the GCNT web and in the presence of cortical cells? We compared the effect of the metabolic inhibitor blebbistatin on the migration of glioma cells in these three environments. Blebbistatin is a small molecule that inhibits both nonmuscle myosin II and smooth muscle myosin II,[43] and it has already been used as a blocker for brain cancer infiltration.[44] The effect of blebbistatin on the migration of fluorescently labeled U87MG on the flat 2D dish was observed with conventional live cell imaging (Figure 4f and Figure S7b, Supporting Information). The 3D trajectories of U87MG (Figure 4a) were obtained over a 4 h period before the application of 50×10^{-6} M blebbistatin and over another 4 h period after the addition of the drug. From the 3D trajectories, we derived the mean velocity (averaged on time and among all cells) before and after the addition of 50×10^{-6} M blebbistatin (Figure 4f). Upon application of 50×10^{-6} M blebbistatin, the mean velocity of U87MG decreased by almost 34% inside the GCNT web and to a lower extent (approximately 23%) in our cortex-like network.

From the 3D trajectories, we also computed the velocity of the movement along the three axes (x, y, and z) with the aim of determining the existence of differences in the velocity in the lateral (x- and y-axes) and axial direction (z-axis). In the absence of coculture with cortical cells, the addition of blebbistatin decreased the velocity in all three directions (Figure 4b). On the other hand, when U87MG cells were cocultured inside the GCNT web with cortical cells (Figure 4c), we observed a significant difference in the velocity only along the x- and y-axes ($p < 0.001$, Kolmogorov–Smirnov test) but not on the z-axis ($p = 0.9467$, Kolmogorov–Smirnov test), indicating that blebbistatin reduces primarily the lateral velocity. Therefore, our results suggest an involvement of the extracellular environment in malignant glioma motility, and in turn, a reduced effect of blebbistatin in the presence of cortical cells compared to the GCNT web alone (Figure 4d,e).

The recent advances in in vitro 3D culture technologies including organoids, spheroid cultures and primary cells grafted directly into biologically relevant matrix preparations and appropriate cortical slices[45] have opened new avenues for the development of more physiological cancer models.[46] The ability of these models to accurately replicate the complex microenvironmental and extracellular conditions prevailing in the brain allows us to visualize brain cancer infiltration, such as in an arthotopic xenograph of malignant glioma in the mouse brain.[47] Nevertheless, none of these approaches allow

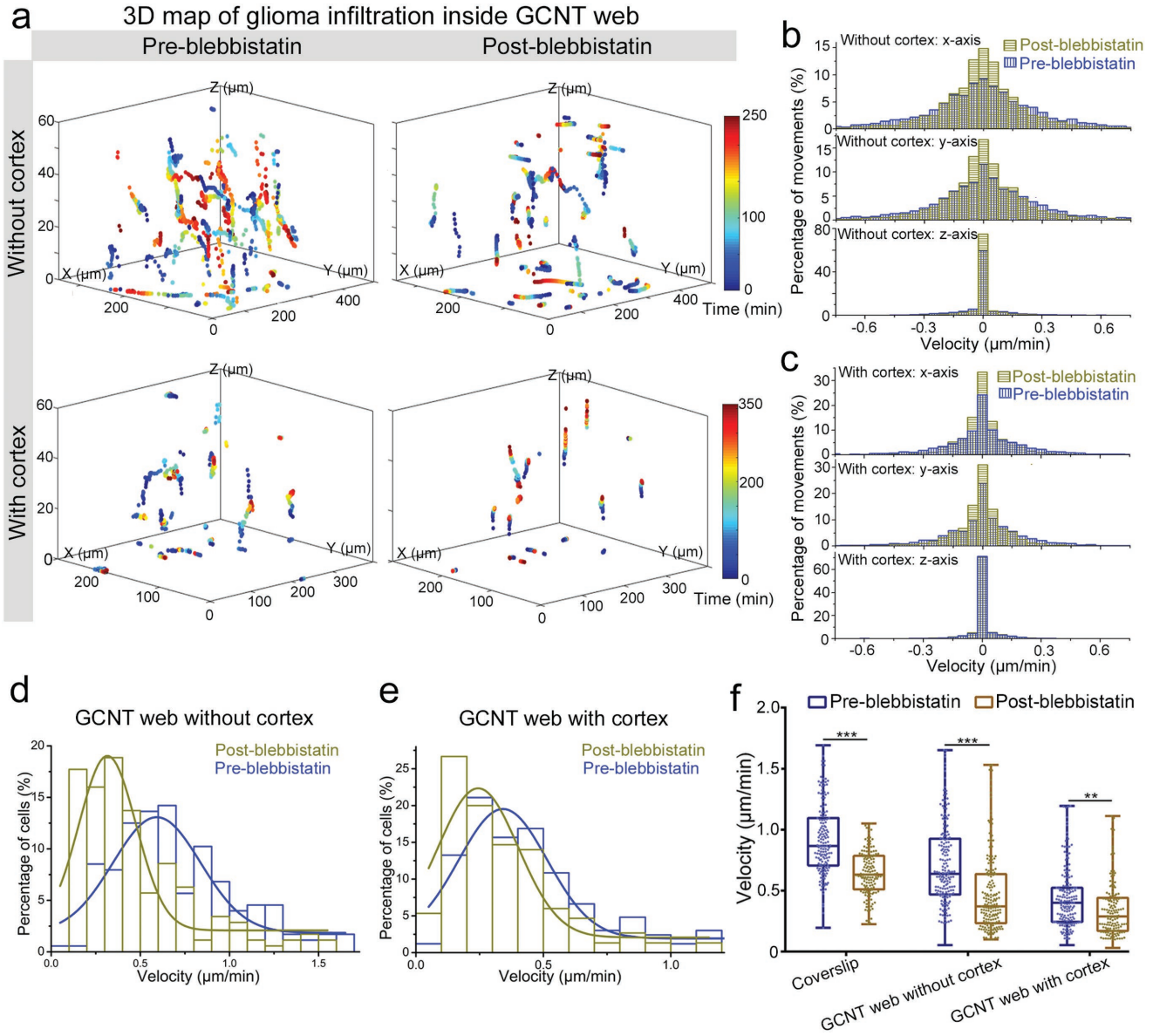

Figure 4. Blebbistatin performed properly on the glioma infiltration model constructed by the cortex-like network. a) 3D map for reconstructing trajectories of glioma infiltration during almost 6 h of live cell imaging pre- and postblebbistatin inside the single GCNT web and the cortex-like network. b,c) Cell movement velocity distribution along *x*, *y*, and *z* inside the single GCNT web and the cortex-like network preblebbistatin (blue) and postblebbistatin (yellow). d) Distribution of absolute cell velocities of glioma preblebbistatin (blue) and postblebbistatin (yellow). e) The same as in (d) but inside the cortex-like network. f) Comparison of the effect of blebbistatin on the absolute glioma velocity grown on a flat coverslip, GCNT web and the cortex-like network (preblebbistatin: coverslip $n = 156$ cells; GCNT web without cortex $n = 176$; with cortex $n = 171$ cells, postblebbistatin: coverslip $n = 144$ cells; GCNT web without cortex $n = 179$ cells; with cortex $n = 149$ cells, two-way ANOVA, Sidak's test).

the recovery of the 3D motion of individual glioma which could provide a 3D map of overall invasion. The combination of our 3D GCNT web with live cell imaging of fluorescently labeled glioma cells and cortical cells allows exact recovery of the 3D trajectories of individual malignant glioma infiltration and quantification of the effect of drugs.

In summary, we have fabricated a 3D monolithic porous GCNT web with fully geometric, mechanical and electrical interconnectivity by in situ CVD growth of interconnected CNT web into the GF pores. The 3D GCNT web provides a novel biomaterial to construct a 3D cortex-like network which responds to dense neuronal network and functional activity closer to the in vivo conditions. The cortex-like network allows to study brain connectivity and neuronal dysfunction and, further, to construct an ideal glioma infiltration model to map the 3D overall invasion, which could be an additional and more visible technology for preclinical therapeutic approaches screening. Future developments already in process include the analysis of the 3D motion of malignant glioma from patients in our model and the comparison of ECM secreted by different kinds of malignant glioma cells. The application of 3D GCNT web in cancer model construction also represents an important step

toward precise and personalized medicine. Indeed, it is possible to derive cortical cells from the stem cells of a patient and to screen drugs that can block the infiltration of brain cancer cells obtained from the same patient. Therefore, our system is not only a novel platform for live cell imaging achievement but also a new route toward the findings of improved methods to eradicate tumors without affecting the host's cells.

Supporting Information

Supporting Information is available from the Wiley Online Library or from the author.

Acknowledgements

M.X. and X.L. contributed equally to this work. This work was supported by the funds from National Key Basic Research Program of China (973 Program Grant No. 2014CB965003), Key Research and Development Program of Jiangsu Province (BE2017665), Regione friuli–venezia giulia (FVG) (Italy) for the project "GLIOBLASTOMA—Infiltrazione nei gliomi: nuovo target terapeutico," the 3315 Innovative Teams Program of Ningbo—China, Zhejiang Provincial Natural Science Foundation of China under Grant No. LQ17C100001, Natural Science Foundation of Ningbo City under Grant No. 2017A610256. The authors thank Beatrice Pastore for technical assistance, Jing Xu and Jiaxin Wang for useful discussions, and Manuela Schipizza Lough for carefully reading the paper. M.X. and G.C. fabricated and characterized the GCNT web. M.X. and F.P.U.S. prepared the cultures and M.L. performed the SEM experiment. M.X. performed calcium imaging experiments with F.P.U.S. and analyzed the data. F.P.U.S., Q.S., and M.X. performed immunofluorescence experiments. V.T. performed the ECM analysis. X.L. performed living cell imaging and analyzed the data with F.P.U.S. and M.X. M.X, F.P.U.S., and X.L. made the figures. V.T. designed the experiments and wrote the paper with M.X., F.P.U.S., X.L., and Q.Z. All the authors read and revised the paper. The authors thank Beatrice Pastore for technical assistance, Jing Xu and Jiaxin Wang for useful discussions and Manuela Schipizza Lough for carefully reading the manuscript. Cortical neurons from Wistar rats (P1–P3) were prepared in accordance with the guidelines of the Italian Animal Welfare Act, and their use was approved by the Local Veterinary Service, the SISSA Ethics Committee board and the National Ministry of Health (Permit Number: 630-III/14) in accordance with the European Union guidelines for animal care (d.1.116/92; 86/609/C.E.).

Conflict of Interest

The authors declare no conflict of interest.

Keywords

3D GCNT web, cancer models, cortex-like, malignant glioma infiltration, neuronal networks

Received: September 20, 2018
Published online: November 2, 2018

[1] K. Watanabe, D. Kamiya, A. Nishiyama, T. Katayama, S. Nozaki, H. Kawasaki, Y. Watanabe, K. Mizuseki, Y. Sasai, *Nat. Neurosci.* **2005**, *8*, 288.
[2] B. Derby, *Science* **2012**, *338*, 921.
[3] B. B. Biswal, M. Mennes, X. N. Zuo, S. Gohel, C. Kelly, S. M. Smith, C. F. Beckmann, J. S. Adelstein, R. L. Buckner, S. Colcombe, A. M. Dogonowski, M. Ernst, D. Fair, M. Hampson, M. J. Hoptman, J. S. Hyde, V. J. Kiviniemi, R. Kotter, S. J. Li, C. P. Lin, M. J. Lowe, C. Mackay, D. J. Madden, K. H. Madsen, D. S. Margulies, H. S. Mayberg, K. McMahon, C. S. Monk, S. H. Mostofsky, B. J. Nagel, J. J. Pekar, S. J. Peltier, S. E. Petersen, V. Riedl, S. A. R. B. Rombouts, B. Rypma, B. L. Schlaggar, S. Schmidt, R. D. Seidler, G. J. Siegle, C. Sorg, G. J. Teng, J. Veijola, A. Villringer, M. Walter, L. H. Wang, X. C. Weng, S. Whitfield-Gabrieli, P. Williamson, C. Windischberger, Y. F. Zang, H. Y. Zhang, F. X. Castellanos, M. P. Milham, *Proc. Natl. Acad. Sci. USA* **2010**, *107*, 4734.
[4] a) M. D. Tang-Schomer, J. D. White, L. W. Tien, L. I. Schmitt, T. M. Valentin, D. J. Graziano, A. M. Hopkins, F. G. Omenetto, P. G. Haydon, D. L. Kaplan, *Proc. Natl. Acad. Sci. USA* **2014**, *111*, 13811; b) F. P. Ulloa Severino, J. Ban, Q. Song, M. Tang, G. Bianconi, G. Cheng, V. Torre, *Sci. Rep.* **2016**, *6*, 29640; c) S. Usmani, E. R. Aurand, M. Medelin, A. Fabbro, D. Scaini, J. Laishram, F. B. Rosselli, A. Ansuini, D. Zoccolan, M. Scarselli, *Sci. Adv.* **2016**, *2*, e1600087; d) P. Soman, J. A. Kelber, J. W. Lee, T. N. Wright, K. S. Vecchio, R. L. Klemke, S. Chen, *Biomaterials* **2012**, *33*, 7064.
[5] L. G. Griffith, M. A. Swartz, *Nat. Rev. Mol. Cell Biol.* **2006**, *7*, 211.
[6] A. Ray, Z. M. Slama, R. K. Morford, S. A. Madden, P. P. Provenzano, *Biophys. J.* **2017**, *112*, 1023.
[7] Y. Mu, F. Wu, Y. R. Lu, L. M. Wei, W. E. Yuan, *Nanomedicine* **2014**, *9*, 1869.
[8] M. C. Serrano, S. Nardecchia, C. Garcia-Rama, M. L. Ferrer, J. E. Collazos-Castro, F. del Monte, M. C. Gutierrez, *Biomaterials* **2014**, *35*, 1543.
[9] a) S. R. Shin, R. Farzad, A. Tamayol, V. Manoharan, P. Mostafalu, Y. S. Zhang, M. Akbari, S. M. Jung, D. Kim, M. Comotto, N. Annabi, F. E. Al-Hazmi, M. R. Dokmeci, A. Khademhosseini, *Adv. Mater.* **2016**, *28*, 3280; b) J. Ren, Q. Xu, X. Chen, W. Li, K. Guo, Y. Zhao, Q. Wang, Z. Zhang, H. Peng, Y. G. Li, *Adv. Mater.* **2017**, *29*, 1702713.
[10] V. Lovat, D. Pantarotto, L. Lagostena, B. Cacciari, M. Grandolfo, M. Righi, G. Spalluto, M. Prato, L. Ballerini, *Nano Lett.* **2005**, *5*, 1107.
[11] E. B. Malarkey, K. A. Fisher, E. Bekyarova, W. Liu, R. C. Haddon, V. Parpura, *Nano Lett.* **2009**, *9*, 264.
[12] S. R. Shin, C. Shin, A. Memic, S. Shadmehr, M. Miscuglio, H. Y. Jung, S. M. Jung, H. Bae, A. Khademhosseini, X. S. Tang, M. R. Dokmeci, *Adv. Funct. Mater.* **2015**, *25*, 4486.
[13] S. Usmani, E. R. Aurand, M. Medelin, A. Fabbro, D. Scaini, J. Laishram, F. B. Rosselli, A. Ansuini, D. Zoccolan, M. Scarselli, M. De Crescenzi, S. Bosi, M. Prato, L. Ballerini, *Sci. Adv.* **2016**, *2*, e1600087.
[14] a) S. R. Shin, S. M. Jung, M. Zalabany, K. Kim, P. Zorlutuna, S. B. Kim, M. Nikkhah, M. Khabiry, M. Azize, J. Kong, K. T. Wan, T. Palacios, M. R. Dokmeci, H. Bae, X. W. Tang, A. Khademhosseini, *ACS Nano* **2013**, *7*, 2369; b) E. R. Aurand, S. Usmani, M. Medelin, D. Scaini, S. Bosi, F. B. Rosselli, S. Donato, G. Tromba, M. Prato, L. Ballerini, *Adv. Funct. Mater.* **2018**, *28*, 1700550.
[15] F. Schutt, S. Signetti, H. Kruger, S. Roder, D. Smazna, S. Kaps, S. N. Gorb, Y. K. Mishra, N. M. Pugno, R. Adelung, *Nat. Commun.* **2017**, *8*, 1215.
[16] M. Kato-Negishi, H. Onoe, A. Ito, S. Takeuchi, *Adv. Healthcare Mater.* **2017**, *6*, 1700143.
[17] V. A. Cuddapah, S. Robel, S. Watkins, H. Sontheimer, *Nat. Rev. Neurosci.* **2014**, *15*, 455.
[18] Q. T. Ostrom, H. Gittleman, P. Liao, T. Vecchione-Koval, Y. Wolinsky, C. Kruchko, J. S. Barnholtz-Sloan, *Neuro-Oncology* **2017**, *19*, v1.
[19] R. Poincloux, O. Collin, F. Lizarraga, M. Romao, M. Debray, M. Piel, P. Chavrier, *Proc. Natl. Acad. Sci. USA* **2011**, *108*, 1943.
[20] B. Auffinger, D. Spencer, P. Pytel, A. U. Ahmed, M. S. Lesniak, *Expert Rev. Neurother.* **2015**, *15*, 741.

[21] D. Hanahan, R. A. Weinberg, *Cell* **2011**, *144*, 646.
[22] L. Gu, D. J. Mooney, *Nat. Rev. Cancer* **2016**, *16*, 56.
[23] X. Zhou, M. Nowicki, H. T. Cui, W. Zhu, X. Q. Fang, S. D. Miao, S. J. Lee, M. Keidar, L. J. G. Zhang, *Carbon* **2017**, *116*, 615.
[24] N. Li, Q. Zhang, S. Gao, Q. Song, R. Huang, L. Wang, L. W. Liu, J. W. Dai, M. L. Tang, G. S. Cheng, *Sci. Rep.* **2013**, *3*, 1604.
[25] Z. P. Chen, W. C. Ren, L. B. Gao, B. L. Liu, S. F. Pei, H. M. Cheng, *Nat. Mater.* **2011**, *10*, 424.
[26] Q. K. Yu, J. Lian, S. Siriponglert, H. Li, Y. P. Chen, S. S. Pei, *Appl. Phys. Lett.* **2008**, *93*, 113103.
[27] X. M. Geng, Y. F. Guo, D. F. Li, W. W. Li, C. Zhu, X. F. Wei, M. L. Chen, S. Gao, S. Q. Qiu, Y. P. Gong, L. Q. Wu, M. S. Long, M. T. Sun, G. B. Pan, L. W. Liu, *Sci. Rep.* **2013**, *3*, 1134.
[28] a) G. C. Reilly, A. J. Engler, *J. Biomech.* **2010**, *43*, 55; b) G. Cellot, E. Cilia, S. Cipollone, V. Rancic, A. Sucapane, S. Giordani, L. Gambazzi, H. Markram, M. Grandolfo, D. Scaini, F. Gelain, L. Casalis, M. Prato, M. Giugliano, L. Ballerini, *Nat. Nanotechnol.* **2009**, *4*, 126.
[29] A. C. Ferrari, J. C. Meyer, V. Scardaci, C. Casiraghi, M. Lazzeri, F. Mauri, S. Piscanec, D. Jiang, K. S. Novoselov, S. Roth, A. K. Geim, *Phys. Rev. Lett.* **2006**, *97*, 187401.
[30] G. Y. Zhu, Z. He, J. Chen, J. Zhao, X. M. Feng, Y. W. Ma, Q. L. Fan, L. H. Wang, W. Huang, *Nanoscale* **2014**, *6*, 1079.
[31] W. Liu, C. Lu, X. Wang, K. Liang, B. K. Tay, *J. Mater. Chem. A* **2015**, *3*, 624.
[32] a) D. Kim, S. M. Kim, S. Lee, M. H. Yoon, *Sci. Rep.* **2017**, *7*, 7716; b) J. L. Liu, L. L. Zhang, H. B. Wu, J. Y. Lin, Z. X. Shen, X. W. Lou, *Energy Environ. Sci.* **2014**, *7*, 3709.
[33] T. Bacaj, D. Wu, X. F. Yang, W. Morishita, P. Zhou, W. Xu, R. C. Malenka, T. C. Sudhof, *Neuron* **2013**, *80*, 947.
[34] P. Golshani, J. T. Goncalves, S. Khoshkhoo, R. Mostany, S. Smirnakis, C. Portera-Cailliau, *J. Neurosci.* **2009**, *29*, 10890.
[35] a) C. A. Whittaker, K. F. Bergeron, J. Whittle, B. P. Brandhorst, R. D. Burke, R. O. Hynes, *Dev. Biol.* **2006**, *300*, 252; b) S. Ozbek, P. G. Balasubramanian, R. Chiquet-Ehrismann, R. P. Tucker, J. C. Adams, *Mol. Biol. Cell* **2010**, *21*, 4300; c) P. F. Lu, V. M. Weaver, Z. Werb, *J. Cell Biol.* **2012**, *196*, 395.
[36] A. Bikbaev, R. Frischknecht, M. Heine, *Sci. Rep.* **2015**, *5*, 14527.
[37] a) S. P. Koh, A. C. Wickremesekera, H. D. Brasch, R. Marsh, S. T. Tan, T. Itinteang, *Front. Surg.* **2017**, *4*, 28; b) J. S. Rao, *Nat. Rev. Cancer* **2003**, *3*, 489.
[38] a) K. A. Giamanco, M. Morawski, R. T. Matthews, *Neuroscience* **2010**, *170*, 1314; b) M. Morawski, G. Bruckner, T. Arendt, R. T. Matthews, *Int. J. Biochem. Cell Biol.* **2012**, *44*, 690.
[39] M. Aumailley, *Cell Adhes. Migr.* **2013**, *7*, 48.
[40] a) A. D. Doyle, F. W. Wang, K. Matsumoto, K. M. Yamada, *J. Cell Biol.* **2009**, *184*, 481; b) F. Sabeh, R. Shimizu-Hirota, S. J. Weiss, *J. Cell Biol.* **2009**, *185*, 11.
[41] J. Y. Tinevez, N. Perry, J. Schindelin, G. M. Hoopes, G. D. Reynolds, E. Laplantine, S. Y. Bednarek, S. L. Shorte, K. W. Eliceiri, *Methods* **2017**, *115*, 80.
[42] J. Sapudom, J. Waschke, K. Franke, M. Hlawitschka, T. Pompe, *Sci. Rep.* **2017**, *7*, 14135.
[43] a) J. H. Huang, J. X. Zhang, A. Pathak, J. X. Li, G. A. Stouffer, *J. Pharmacol. Exp. Ther.* **2011**, *336*, 116; b) M. Shutova, C. S. Yang, J. M. Vasiliev, T. Svitkina, *PLoS One* **2012**, *7*, e40814.
[44] S. Ivkovic, C. Beadle, S. Noticewala, S. C. Massey, K. R. Swanson, L. N. Toro, A. R. Bresnick, P. Canoll, S. S. Rosenfeld, *Mol. Biol. Cell* **2012**, *23*, 533.
[45] B. M. Baker, C. S. Chen, *J. Cell Sci.* **2012**, *125*, 3015.
[46] J. Drost, H. Clevers, *Nat. Rev. Cancer* **2018**, *18*, 407.
[47] J. G. Valadez, A. Sarangi, C. J. Lundberg, M. K. Cooper, *JoVE* **2014**, *83*, e50865.

ADVANCED MATERIALS

Supporting Information

for *Adv. Mater.*, DOI: 10.1002/adma.201806132

A Fully 3D Interconnected Graphene–Carbon Nanotube Web Allows the Study of Glioma Infiltration in Bioengineered 3D Cortex-Like Networks

Miao Xiao, Xiaoyun Li, Qin Song, Qi Zhang, Marco Lazzarino, Guosheng Cheng, Francesco Paolo Ulloa Severino,* and Vincent Torre**

Supporting Information

A Fully 3D Interconnected Graphene–Carbon Nanotube Web Allows the Study of Glioma Infiltration in Bioengineered 3D Cortex-Like Networks

Miao Xiao, Xiaoyun Li, Qin Song, Qi Zhang, Marco Lazzarino, Guosheng Cheng, Francesco Paolo Ulloa Severinoe,* and Vincent Torre**

Materials and Methods

Synthesis processes of intercalated $FeCl_3$-graphite. Intercalated $FeCl_3$-graphite was synthesized using a reported two-zone vapour transport method[24]. Graphite flakes (1 g, 99.8%, ABCR Karlsruhe, Germany) and anhydrous $FeCl_3$ powder (5.6 g, Alfa Aesar) were mixed in a two-zone reactive container. Then, the container was heated at 380℃ for 24 hours in a muffle furnace (TM-0912P, China). After having naturally cooled down to room temperature, the as-synthesized compound was used as the catalyst in CNT growth.

Synthesis processes of GCNT web. The GCNT web were fabricated by a two-step chemical vapour deposition (CVD) process in a horizontal tube furnace (Thermcraft, USA), including the growth of GF and GCNT web. The pre-cleaned porous Ni foam (PPI 100±10, Alantum Advanced Technology Materials, China) was placed in a 1-inch-diameter quartz tube that was pre-mounted in the furnace. During the preparation of GF, the Ni foam was first annealed at 950℃ for 10 minutes under H_2 (100 sccm) and Ar (100 sccm) atmosphere to clean their surfaces and eliminate surface oxidation layers. Next, 50 sccm of H_2 and CH_4 was introduced into the CVD system for 30 minutes, following by cooling to room temperature to allow graphene to grow on the Ni scaffold surfaces. The prepared GFs were cut at a width of 1 cm to be the carrier of CNTs. During the growth of CNTs, the as-synthesized intercalated $FeCl_3$-graphite powder was loaded upstream and next to the GF in a rail boat, which was then transferred into the middle of a quartz tube. Approximately 160 sccm of H_2 and 40 sccm of CH_4 was introduced into the CVD system for 15 minutes after the furnace was heated to 1050

℃ under the protection of Ar (200 sccm). The samples were then submerged into a $FeCl_3$ (1 M) solution for 48 hours to chemically etch Ni from the Ni foam. Then, the samples were immersed into hot HNO_3 at 80 ℃ for 2 hours. After complete etching, the GCNT web were washed with deionized water until the pH was 7. The GCNT web samples were finally dried at 60 ℃ in air.

Morphological, structural and physical property characterizations of GCNT web. Morphological and structural characterizations of the 3D-CG samples were investigated by field-emission scanning electron microscopy (SEM) equipped with an energy dispersive spectrometer (EDS) (Quanta 400 FEG, FEI, USA). The crystallinity and number of the layer presented within graphene were examined by a Raman spectrometer (LabRAMHR800, HORIBA, France). In the mechanical property characterization, a compression test was carried out by a high-precision mechanical testing system (Instron 3365, USA). Conductivity was performed using an Agilent B1500A semi-conductor device analyser (Agilent Technologies Inc., USA).

Neuronal network preparation and culture. Cortical neurons from Wistar rats (P1-P3) were prepared in accordance with the guidelines of the Italian Animal Welfare Act, and their use was approved by the Local Veterinary Service, the SISSA Ethics Committee board and the National Ministry of Health (Permit Number: 630-III/14) in accordance with the European Union guidelines for animal care (d.1.116/92; 86/609/C.E.). To minimize the suffering of animals, the rats were anaesthetized with CO_2 and sacrificed by decapitation quickly. During the culture process, substrates, including 3D GFs and 3D GCNT web, were first cleaned with O_2 plasma and sterilized with ultraviolet rays (UV). Then, they were coated with 50 μg mL^{-1} poly-L-ornithine (Sigma-Aldrich, St. Louis, MO, USA) overnight, immersed in culture medium overnight and coated with Matrigel just before cell seeding (Corning, Tewksbury MA, USA). The samples for ECM protein immunocytochemical staining were not coated with Matrigel. Dissociated cells were plated at a concentration of 2.4×10^6 cells Ml^{-1} on 3D

GF and 3D GCNT web in a drop of minimum essential medium (MEM) with GlutaMAXTM supplemented with 10% foetal bovine serum (FBS, all from Invitrogen, Life Technologies, Gaithersburg, MD, USA), 0.6% D-glucose, 15 mM Hepes, 0.1 mg ml^{-1} apo-transferrin, 30 μg ml^{-1} insulin, 0.1 μg ml^{-1} D-biotin, 1 μM vitamin B12 (all from Sigma-Aldrich), and 2.5 μg ml^{-1} gentamycin (Life Technologies). After 1 hour Neurobasal supplemented with 2% of B-27, 10 mM Glutamax (all from ThermoFisher) and 0.5 μM Gentamycin (Sigma) was added as a culture medium. Half of the medium was changed every week. Neuronal cultures were maintained in an incubator at 37 °C, 5% CO_2 and 95% relative humidity.

Morphological and immunocytochemical analysis. Cells were fixed in 4% paraformaldehyde containing 0.15% picric acid in phosphate-buffered saline (PBS), saturated with 0.1 M glycine, permeabilized with 0.1% Triton X-100, saturated with 0.5% BSA (all from Sigma-Aldrich) in PBS and then incubated with phalloidin Alexa Fluor® 488 (Life Technologies) for 30 minutes or o.n. at 4°C with primary antibodies: rabbit polyclonal against MAP2, rabbit polyclonal against aggrecan and mouse monoclonal against laminin (all from Sigma-Aldrich) and SMI 312 mouse monoclonal antibodies (Covance, Berkeley, CA). The secondary antibodies were goat anti-rabbit Alexa Fluor® 488, goat anti-mouse Alexa Fluor® 488, (all from Life Technologies), biotin conjugated goat anti-mouse and goat anti-rabbit (Sigma); the incubation time was 3 hours at room temperature (20–22 °C). When a biotin conjugated secondary antibody was used, another incubation of 1 hour with streptavidin Alexa Fluor® 647 (Life Technology) was performed. Nuclei were stained with 2 μg ml^{-1} PBS Hoechst 33342 (Sigma-Aldrich) for 5 minutes. Samples were mounted in Vectashield (Vector Laboratories) on 1-mm thick coverslips with a homemade adaptor of PDMS to host the 3D samples. The cells were examined using a Nikon C2 confocal microscope to acquire higher quality images. The fluorescence images were collected with a 20X magnification and 0.5 NA objective. Each image was acquired with z-steps of 2 μm. Analysis and 3D reconstruction of

the image stack were accomplished using NIS-Elements AR software (Nikon), Volocity (PerkinElmer), and the open source image-processing package Fiji (http://fiji.sc/Fiji).

Calcium imaging acquisition procedures. The cultured cells at 2, 3, 4, 6, 8, and 15 days *in vitro* (DIV 2, 3, 4, 6, 8, and 15, respectively) were loaded with a membrane-permeable calcium dye Fluo4-AM (Life Technologies) by incubating them with 4 μM Fluo4-AM (dissolved in anhydrous DMSO (Sigma-Aldrich), stock solution 4 mM) and Pluronic F-127 20% solution in DMSO (Life Technologies) at a ratio of 1:1 in Ringer's solution (145 mM NaCl, 3 mM KCl, 1.5 mM $CaCl_2$, 1 mM $MgCl_2$, 10 mM glucose and 10 mM Hepes, pH 7.4) at 37°C for 1 hour. After incubation, the cultures were washed with Ringer's solution for 30 minutes and then transferred to the stage of a Nikon Eclipse Ti-U inverted microscope equipped with a piezoelectric table (Nano-ZI Series 500 μm range, Mad City Labs), an HBO 103 W/2 mercury short arc lamp (Osram, Munich, Germany), a mirror unit (exciter filter BP 465–495 nm, dichroic 505 nm, emission filter BP 515–555) and an Electron Multiplier CCD Camera C9100-13 (Hamamatsu Photonics, Japan). The calcium imaging recordings were performed at RT, and images were acquired using the NIS Element software (Nikon, Japan) with an S-Fluor 20x/0.75 NA objective at a sampling rate of 3–5 Hz with a spatial resolution of 256×256 pixels for 10 minutes. To avoid saturation of the signals, excitation light intensity was attenuated by ND4 and ND8 neutral density filters (Nikon).

Calcium imaging processing and analysis. The initial video was processed with ImageJ (U. S. National Institutes of Health, Bethesda, MA) software. The image sequences were then analysed as previously described. Briefly, neurons were localized, and an appropriate region of interest (ROI) was selected to subtract the background. Appropriate ROIs around the cells bodies were then selected. The time course of the fluorescence intensity, $I_f(t)$, in this ROI was displayed, and any decay, which is a consequence of dye bleaching, was evaluated. The Ca^{2+} transients of each cell signal were extracted in a semi-automatic manner by selecting a threshold for the smallest detectable peak that was equal to three times the standard deviation

of the baseline. Subsequently, the decay of $I_f(t)$ was fitted to a cubic spline (Y(t)) interpolating $I_f(t)$ at 10 or 20 points. Y(t) was then added to the original optical signal to compensate for dye bleaching, and the fractional optical signal was calculated as follows:

$$\Delta F/F = (Y(t) + If(t))/ If(0) \quad (1)$$

where $I_f(0)$ is the fluorescence intensity at the beginning of the recording.

Computation of raster plot and correlation coefficient of Calcium transient occurrence. The times, t_i, at which transient peaks occurred are presented in a conventional raster plot. To isolate the smaller transients from the larger ones, single traces were considered independently. The amplitude distribution of peaks was calculated to separate the two different classes of events. Based on this distribution, a threshold was set to approximately 30% of the maximum amplitude. All peaks under the threshold were considered small transients, whereas all other peaks were considered to be large calcium transients.

The correlation coefficient of the calcium transients for neuron *i* and neuron *j* (σ_{CTij}) was computed as follows. The total recording time, T_{tot}, was divided into *N* intervals (1..,n,…,N) of a duration Δt. Thus, if f_{in} and f_{jn} are the numbers of calcium transients of neuron *i* and neuron *j* in the time interval Δt_n, then we have the following equation:

$$\sigma_{CT_{ij}} = \frac{\Sigma_n f_{in} f_{jn}}{\sqrt{(\Sigma_n f_{in}^2)(\Sigma_n f_{jn}^2)}} \quad (2)$$

where σ_{CTij} depends on Δt and varies between 0 and 1. The range of explored values of Δt was 20 s.

Live cell imaging of U87MG culture and co-culture system. U87MG purchased from SIGMA (#89081402) were cultured in Dulbecco's Modified Eagle Medium (DMEM) supplemented with 10% foetal bovine serum (FBS, all from Invitrogen, Life Technologies, Gaithersburg, MD, USA), 1% PenStrep (100 U mL^{-1} penicillium and 100 µg mL^{-1} streptomycin, Invitrogen) and passaged every 3 days. The mCherry-labelled U87MG cells were kindly provided by the laboratory of Prof. Antonello Mallamaci from the International

School of Advanced Studies. U87MG cells were acutely infected at a concentration of 500 cells μL^{-1} by a mix containing a lentiviral vector, LV_Pgk1p-mCherry, at a multiplicity of infection (m.o.i.)=6. This m.o.i. is sufficient to infect almost all U87MG cells in these conditions.

When required, U87MG cells were treated with 1Xtrypsin-EDTA (0.05% trypsin and 0.02% EDTA, Sigma) and suspended in the culture medium. Approximately $2.0x10^4$ U87MG cells were plated on a flat coverslip, 3D GCNT web and 3D GCNT web with cortex cells that had been cultured for 5 days, and then, the co-culture system was cultured in the incubator at 37°C, 5% CO_2 and 95% relative humidity for two days, and the recording experiments were started. Before seeding U87MG cells, the cortex cells were stained with Vybrant™ DiD Cell-Labeling Solution (5 µL mL^{-1}, Thermo Fisher) for 20 minutes and then washed with a warm medium. During the imaging experiment, blebbistatin (Sigma) was administered to the cells at a final concentration of 50 µM in the culture medium.

Living cell imaging acquisition procedures and analysis. Live cell imaging experiments were performed on an epi-fluorescence microscope (Olympus IX-83, Olympus) equipped with an imaging chamber incubator (Okolab, Pozzuoli, Italy) and LED illumination (λ=590 nm for mCherry, λ=660 nm for Vybrant DiD). During all imaging experiments, cells were kept at 37°C, 5.0% CO_2 and 95% humidity. Time-lapse images were taken with 500 ms of exposure time. When Z-stack images were acquired for 3D motion tracking, we recorded a stack of 20 images with z-steps of 3 µm every 3 minutes. All acquisitions were done with a CCD sensor at 12-bit depth (ORCA-D2, Hamamatsu) and operated with a 20X air objective (Olympus, NA=0.75).

The videos were analysed using the Fiji plugin TrackMate[50], which allows the selection of regions of interest (ROIs) for every cell in 3D. It also allows us to follow the centroid of the 3D ROI over time and obtain the average velocities and 3D coordinates. Once the cell ID, xyz positions and time points were extracted, the trajectories and velocities on the three axes (x, y,

and z) were visualized by plotting the coordinates using Matlab 2015. To calculate and plot the velocities on every single axis (x, y, and z), we established a 5-point numerical differentiation formula (see Matlab code) as follows:

$$f'[x_0] = \frac{f[x_0-2h]-8f[x_0-h]+8f[x_0+h]-f[x_0+2h]}{12h} \quad (4)$$

Using this approach, we could evaluate the different velocities of U87MG cells in the presence and absence of cortical cells and before and after the administration of the drug blebbistatin.

Statistical analysis. Data are shown as the mean ± s.e.m. from at least three neuronal culture preparations from different animals. For the morphological analysis of immunofluorescence images, n refers to the number of images analysed. The quantified activity (IEI and cross-correlation) and morphological data were analysed with the ANOVA test followed by post-hoc comparisons using the software Sygma Plot 10.0. Differences between two groups were evaluated with an unpaired t-test (Statistica 6.0 – StatSoft Italy). The number of replicas and statistical tests used for each experiment is mentioned in the respective figure legends or in the Results section. Significance was set to *$p < 0.05$, **$p < 0.01$ and ***$p < 0.001$.

Supporting Figures

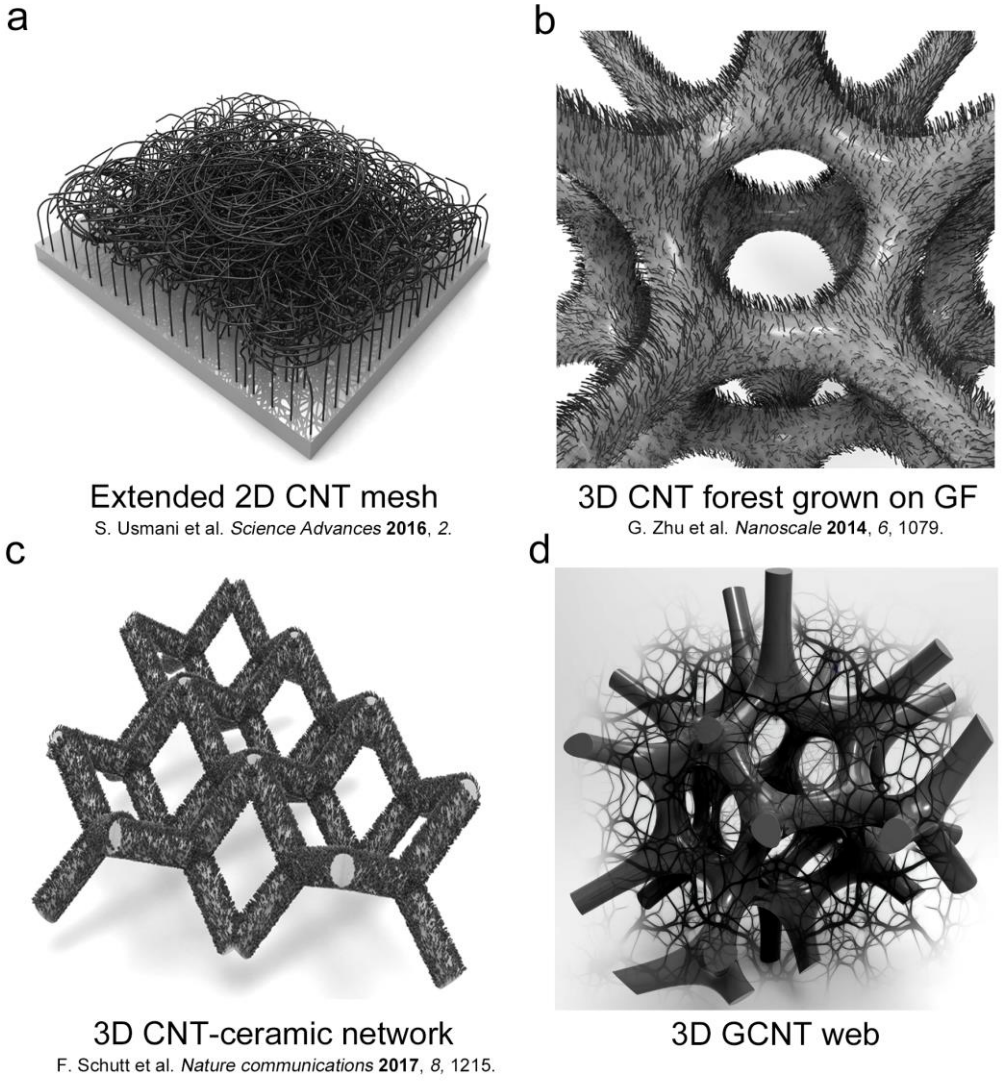

Figure S1. Representative CNT structures reported in the literature.

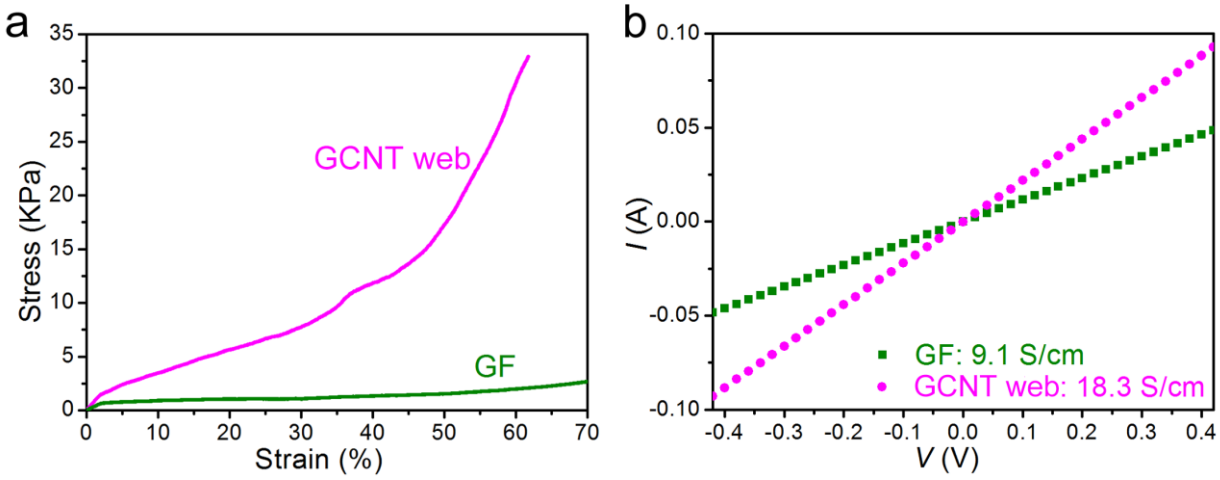

Figure S2. Physical properties of GCNT web. a) Strain-stress curves acquired from compressed test on GCNT web and GF. b) *I-V* curves acquired from four points electrical test on GCNT web and GF.

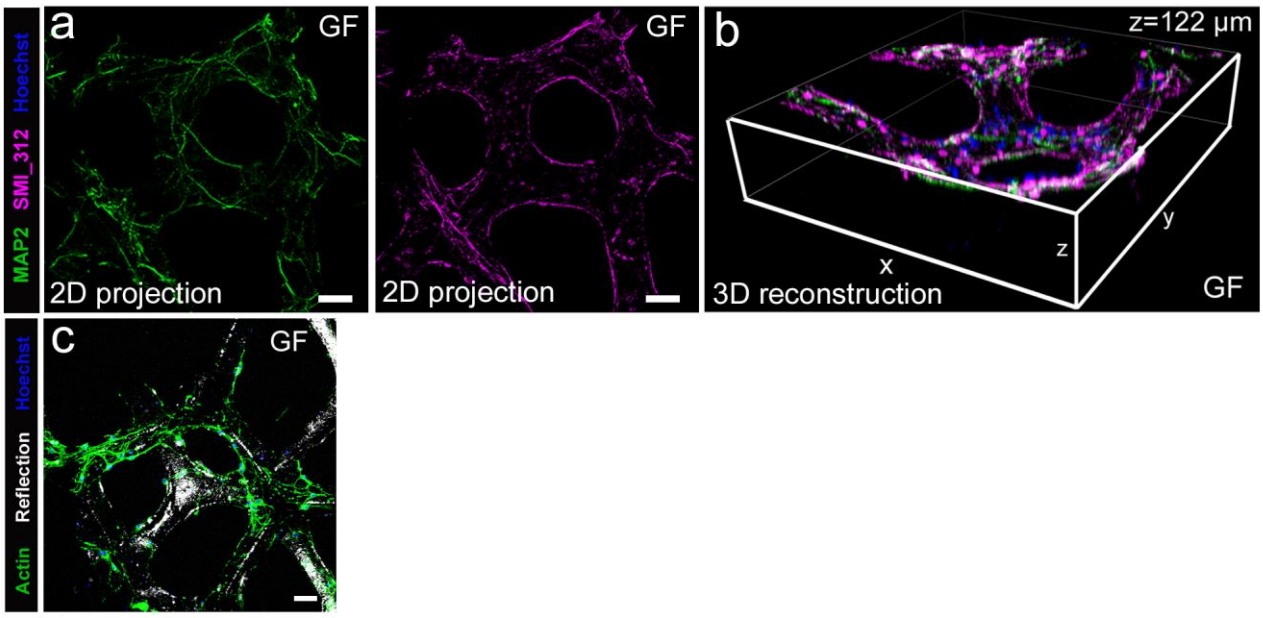

Figure S3. 3D cortical culture embedded into GF scaffolds. a-b) Staining for axons (with SMI_312) and neurites (with MAP2) on GF c) Actin staining of cortical cells after 8 days of culture on GF scaffold. The intricate mesh made by neuronal processes inside the GCNT web is more extended than the network formed on GF.

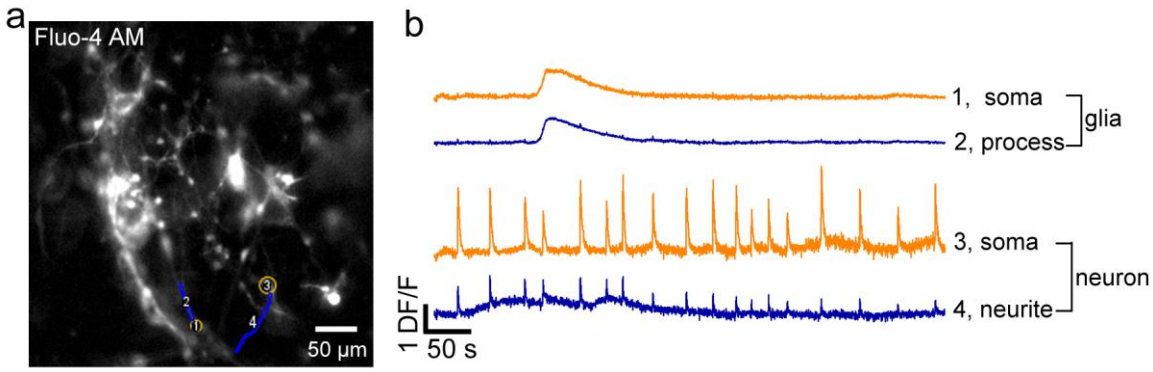

Figure S4. Typical calcium transients from glial cells and neurons. a) Representative fluorescence image of a neuronal culture loaded with Fluo-4 AM grown on a GCNT web. Orange (blue) circles indicate selected regions corresponding to the soma (neurite/process) of both neuron and glia cell. b) Optical transients from glia have a slow time course (upper portion of the panel) and those from neurons (lower portion) have a faster rising phase. Occasionally the neuronal fast transients can be contaminated from slow signals coming from glia cells often positioned below the neurons.

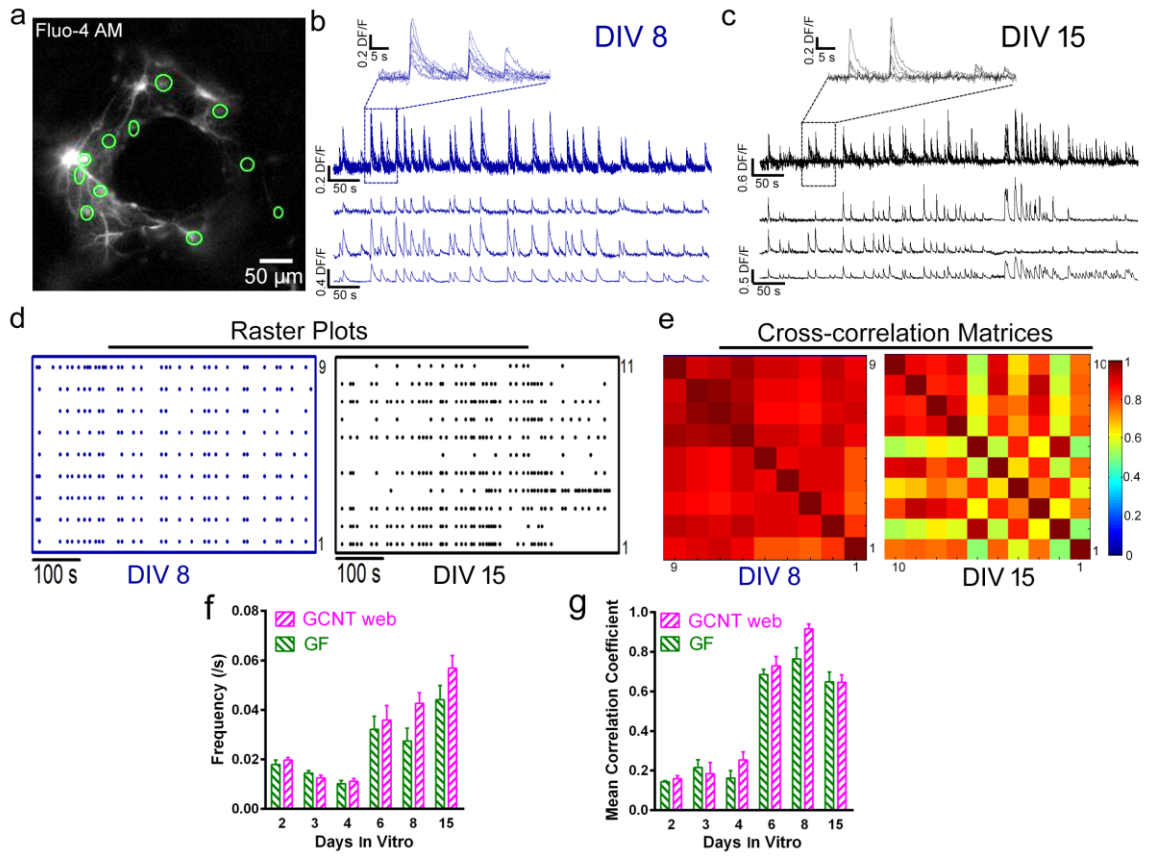

Figure S5. Spontaneous activity dynamics of 3D cortical cultures. a) Representative fluorescent image of a neuronal culture loaded with Fluo-4 AM grown in a GF scaffold. Olive circles indicate regions selected for the recovery of calcium transients. b-c) Representative superimposed optical traces (3 of them are shown separately in the bottom) obtained from the 3D neuronal network cultured on GF at DIV 8 and 15 respectively. The insets in the top portion of both panels show on an expanded time scale the synchronized calcium transients. d) Raster plot of the peaks of optical transients at DIV 8 and 15 for 9 and 11 different neurons respectively. e) Cross-correlation matrices of calcium transients from neuronal networks cultured on GF at DIV 8 and 15 respectively. f) Frequency of calcium transients from cortical cultures grown on GF and GCNT web at different developmental stages. g) Mean correlation coefficient of calcium transients from cortical cultures grown on GF and GCNT web at different developmental stages.

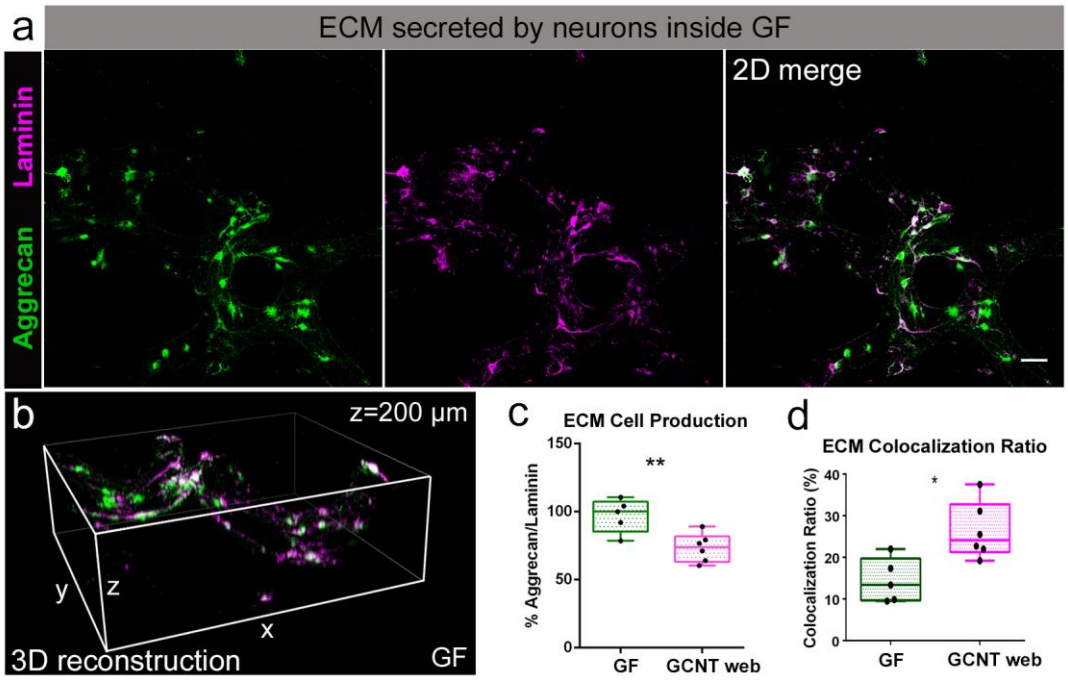

Figure S6. The 3D ECM secreted by cortical cells grown on GF scaffolds. a) Representative staining of aggrecan (left panel) and laminin (middle panel) secreted by cortical cells cultured in 3D GF scaffold. b) 3D reconstruction of laminin and aggrecan, which form the ECM secreted by cortical cells grown on GF. c) Ratio of production of aggrecan versus laminin on

GF and GCNT web. Collected data from 4 and 6 different stains in GF and GCNT web, respectively. d) Colocalization ratio between aggrecan and laminin on GF and GCNT web.

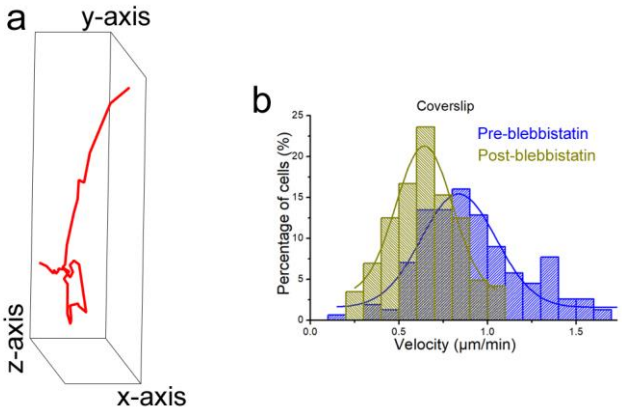

Figure S7. a) Representative trajectory of a U87MG infiltration inside GCNT web. b) Velocity distribution of glioma cultured on coverslip under the treatment of blebbistatin. n=156 cells for pre-blebbistatin and n=144 cells for post-blebbistatin.

Supporting Movies

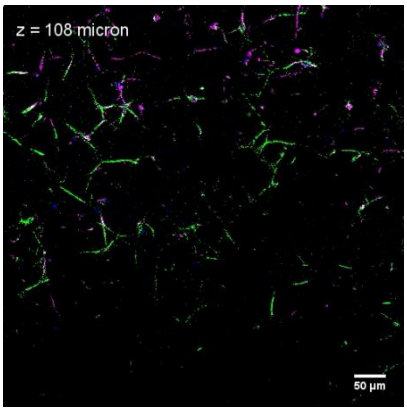

Movie S1. 3D reconstruction of cortical neuronal network embedded in GCNT web at DIV 8. Images were acquired by Nikon C2 confocal microscope with a 20X magnification and 0.5 NA objective. Each image was acquired with z-steps of 2 µm.

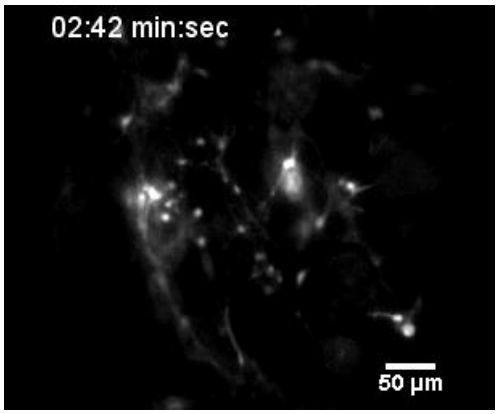

Movie S2. Calcium imaging from neuronal culture loaded with 4 µM Fluo-4-AM calcium indicator in 3D GCNT web at DIV 8. Images were acquired with 20X and 0.75 NA objective, 5 Hz, a spatial resolution of 256 × 256 pixels and for 10 min. The movie reproduction has been made using 100 frames per second.

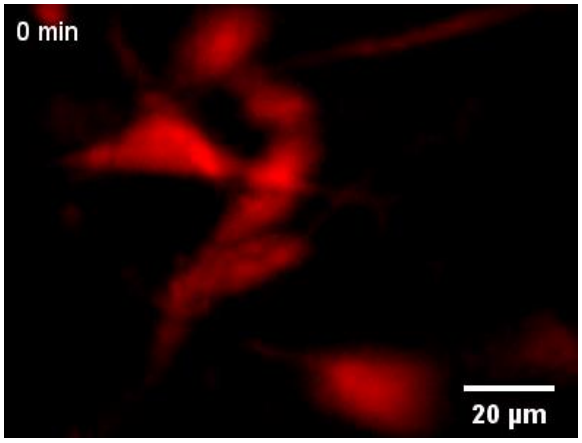

Movie S3. Living cell imaging from U87 GBM cells labeled with the red fluorophore mCherry by infecting with LV_Pgk1p-mCherry cultured in 3D GCNT web. Images were taken with a 20X and 0.75 NA air objective, 2 Hz. Stack of 20 images with z-steps of 3 µm every 3 minutes.

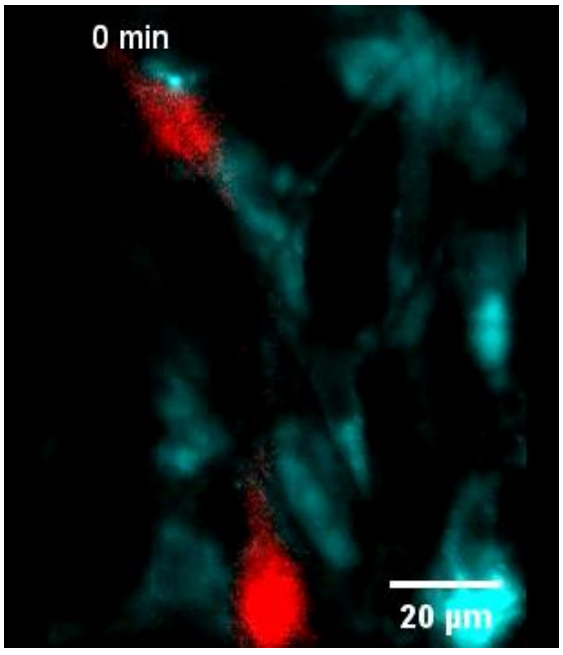

Movie S4. Living cell imaging from U87 GBM cells labeled with the red fluorophore mCherry by infecting with LV_Pgk1p-mCherry and cortical cells labeled with the fluorescent probe DiD co-cultured in 3D GCNT web. Images were taken with a 20X and 0.75 NA air objective, 2 Hz. Stack of 20 images with z-steps of 3 µm every 3 minutes.

3.3 Molecular mechanisms of the blockage of glioblastoma motility

In collaboration with Alessandra Magistrato at SISSA and her student we performed an investigation of the action of three inhibitors of the small GTPAse Rac1 and Cdc42. I performed the wet analysis and the group of Alessandra Magistrato performed the molecular dynamic simulations. The wet analysis was performed in collaboration with Jing Xu and therefore the same manuscript is presented in the PhD thesis of both of us.

In what follow I have reported a very preliminary draft of the manuscript, which we will complete in the next months, hopefully before the end of the present year.

Molecular mechanisms of the blockage of glioblastoma motility

Abstract

Glioblastoma (GBM) is the most common and lethal brain tumor. GBM have a remarkable degree of motility and are able to infiltrate in the healthy brain. In order to perform a rational-based drug-repositioning study we have used known inhibitors of two small Rho GTPase, Rac1 and Cdc42, which are upregulated in GBM and are involved in signaling processes underlying the orchestration of the cytoskeleton and therefore in cellular motility. The selected inhibitors (R-ketorolac and ML141 for Cdc42 as well as R-ketorolac and EHT 1864 for Rac1) have been successfully employed to reduce the infiltration propensity of the GBM. All-atoms simulations have unprecedentedly disclosed the binding poses of these drugs on the target proteins, providing a rationale at atomic-level of detail of their non-competitive inhibition mechanism.

Introduction

Glioblastoma (GBM; World Health Organization grade IV glioma) is the most common and lethal intrinsic tumor. Unlike other solid tumor cell types, GBM invades the surrounding brain and in contrast with other kind of cancers, GBM rarely metastasizes to other organs. Although several attempts, for instance using several drugs such as bevacizumab or immunotherapies [1-3], have been made to stop and counteract GBM infiltration, GBM treatment is still mainly focused and primarily limited to surgical resection followed by concurrent radiation therapy with some chemotherapic reagent such temozolomide [4, 5]. GBM represents one of the most comprehensively genomically characterized cancer types [6, 7], leading to recognition of groups of tumors defined by four distinct transcription profiles (proneural, neural, classical, and mesenchymal). Mutations leading to the transformation of healthy astrocytes into malignant glioma and/or GBM [5] are very diverse and indeed there are at least the four above mentioned different transcription profiles at the basis of brain tumors.

The molecular mechanisms at the basis of cellular motility are similar in all cells and in healthy cells and neurons as well as in malignant GBM. The process of polymerization of actin filaments is the main source of cellular motion and protrusion, which is regulated and controlled by several proteins such as Actin related protein 2/3 complex (Arp2/3), cofilin, formin and molecular motors, such as myosin, dynein, controlling different features of cellular motility [8]. A key role in cellular motility and migration is played by the small GTP-ases, which are presented in all migrating cells. Rho family GTPase has distinct and specific roles in the regulation of growth, maintenance and retraction of growth cones (GCs) [9]. The mammalian typical Rho GTPase family consists of three subfamilies, Rho subfamily (RhoA, RhoB and RhoC), Rac subfamily (Rac1, Rac2, Rac3 and RacG) and Cdc42 subfamily (Cdc42, RhoQ and RhoJ) [10]. RhoA, Rac1 and Cdc42 are well-studied members of Rho GTPase family controlling distinct cytoskeletal elements. Activation of Rac1 stimulates actin polymerization to form lamellipodia [11], Cdc42 induces the polymerization of actin to form filopodia and Rho

regulates the bundling of actin filaments into stress fibers and the formation of focal adhesion complexes [12].

The GTP-binding proteins of Rho family are activated by a variety of growth factors, cytokines, adhesion molecules, hormones, integrins, G-proteins and the other biologically active substances [13, 14]. Biochemical approaches have shown that Rho GTPase also involves crosstalk. Depending upon the concentration and localization of these Rho GTPases, mammalian cells show different morphology, movement and behavior [15]. GTPase work via a cyclic mechanism in which they pass from an active guanine triphosphate (GTP) bound form, to an inactive Guanine Diphospate (GDP) bound form after the GTP hydrolysis occurs fostered by the GTPase-activating protein (GAP), in which the GEF enhance the exchange of the GTP/GDP nucleotide.

At the basis of the present manuscript there is the biological observation that the cellular motility - allowing cells to move, migrate and infiltrate - is in essence very similar in all kind of cells and is primarily based on the orchestration of the cytoskeleton and of a variety of adhesion molecules. The proteins involved in these biological processes as well as their inhibitors are known and in the present manuscript we focus on three inhibitors of cellular motility, i.e. ML141, EHT 1864 and R-ketorolac. These inhibitors will be employed to monitor their ability to reduce cellular motility. Complementarily, Molecular Dynamics (MD) simulations have been instrumental to have a better understanding of their binding mode and mechanisms of the action of these inhibitors from an atomic-level perspective. Our outcomes remark the importance of abrogating the cellular mobility in infiltrative tumor types like GBM, and provide a fundamental advance in understanding the mechanism of small molecules inhibitors of Rho GTPase, which are of pivotal importance to devise novel more effective drug-candidates.

Results

According to The Cancer Genome Atlas (TCGA) (cancergenome.nih.gov), the analysis of the expression level of proteins involved cellular motility in normal tissue and GBM is here reported in Figure 1A and C for Rac1 and Cdc42 and showing that Rac1 and Cdc42 are both upregulated in primary and recurrent tumors. The overexpression of these two proteins is strongly related to a lower survival time of the patient (Figure 1 B and D).

Cdc42 and Rac1 are primarily involved in cellular motility [16] and their upregulation leads to a higher infiltration ability of malignant GBM to invade the healthy tissue. We selected three inhibitors R-ketorolac, ML141 and EHT 1864 to carry out an in silico investigation of the binding of these drugs to Cdc42 and to Rac1 (R-ketorolac and ML141 for Cdc42 as well as R-ketorolac and EHT 1864 for Rac1) and their effect on the migration and infiltration of GBM. These three inhibitors have a rather different structure (Figure 1E) both in size and in chemical properties. R-ketorolac contains a carboxylic moiety, which, being negatively charged at physiological pH, will enter into cells - and inside GBM - much more slowly that ML141, who is neutral, and of EHT 1864, who is positively charged. R-ketorolac is known to affect the activity of both Rac1 and Cdc42, with the following half inhibitory concentrations (IC50): R-ketorolac 0.57 μM and 1.01 μM for Rac1 and Cdc42, respectively [17]. Conversely, ML141 and EHT 1864 are exclusive inhibitors of Cdc42 (IC50 of 0.20 μM) [18] and Rac1 (IC50 1–5 μM) [19, 20], respectively. These values of IC50 refer to biochemical assay in which the target proteins and the inhibitors have been purified and are in a solution. In the next section we will examine the effect of these inhibitors on the migration of GBM and the effective concentration are higher because of the more complex conditions.

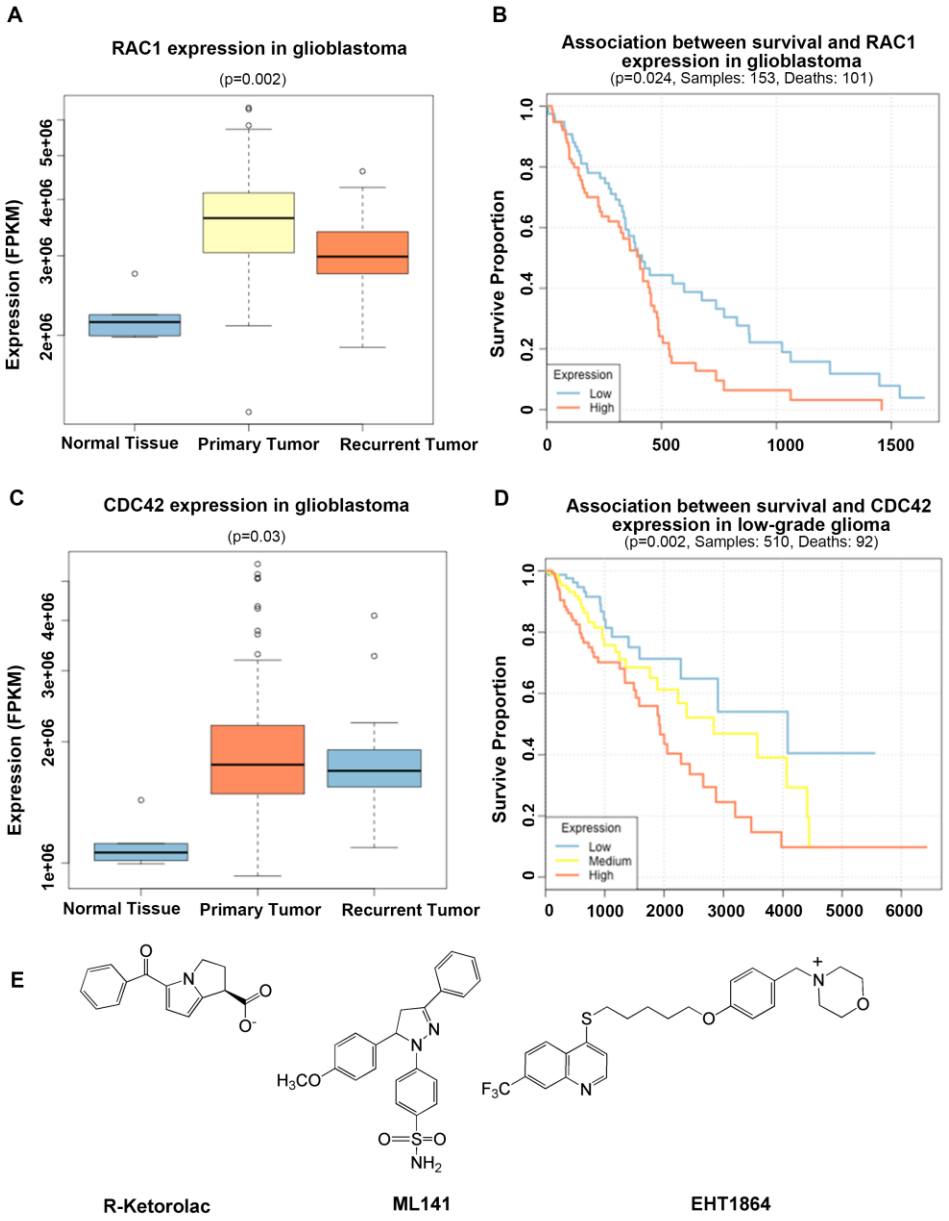

Figure 1 - Analysis of Rac1 and Cdc42 in GBM: differential expression and association to patient survival in The Cancer Genome Atlas (TCGA) data. A and C, Rac1 (A) and Cdc42 (C) is significantly overexpressed in glioma tumor samples, compared to matched normal brain tissue. P-value calculated using DESeq2. B. GBM patients with higher Rac1 expression are associated to higher risk than patients with lower Rac1 expression. D, Low-grade glioma patients with higher Cdc42 expression are associated to higher risk

than patients with lower Cdc42 expression P-value calculated using log-rank test. E, Sketch of R-ketorolac, ML141 and EHT 1864 molecular structure.

The action of the inhibitors on GBM migration

We analysed GBM cell line U87 which is very often used for understanding properties of high grade GBM. Migration and infiltration were studied by the transwell assay (Figure 2 and 3) and by live cell imaging (Figure 4 and 5). The transwell migration assay is a standard method of measuring cell movement through an empty space. The transwell assay is based on the use of a hollow plastic chamber sealed at one end with a porous membrane. The chamber is suspended over a larger well which containing a specific medium. Migrating cells, i.e. infiltrating GBM are plated inside the chamber and allowed to migrate through the pores to the other side of the membrane. Migrated cells are fixed after a given time, stained and counted. Live cell imaging methods visualize individual cells in a dish and take an image every minute and in this way can follow the motility of individual cells. These two methods are complementary: live cell imaging require a substantial illumination of the cells under investigation and cannot be used for experiments lasting several days, while the transwell assay can be used over several days with only minor side effects on the investigated cells (Figure 2). The elongated and fusiform shapes in Figure 2 are the profile of the migrating U87 GBM in control conditions (first column) and in the presence of 1, 10 and 20 μM of EHT 1864 (second, third and fourth column). The assay was conducted for three days (first, second and third row in Figure 2). Visual inspection shows that more GBM cells are able to invade into the empty space at later days and that this migration is reduced by increasing amount of EHT 1864.

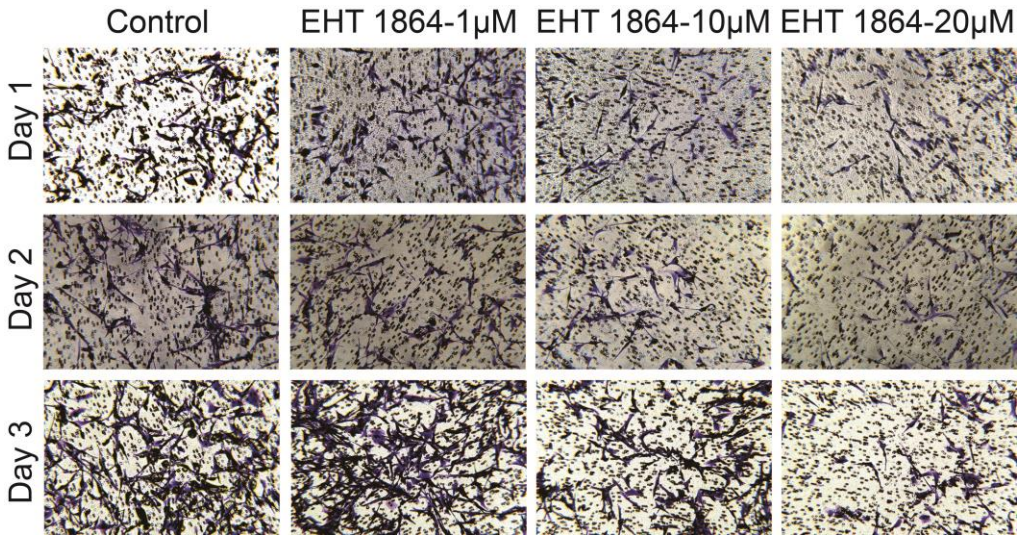

Figure 2 – Rac1 inhibitor EHT 1864 reduces transwell migration of U87 GBM cells. Transwell assay was conducted for three days (first, second and third row) in the presence of 0, 1, 10 and 20 μM of EHT 1864 (first, second, third and fourth column).

The number of GBM present in the empty space at different days obtained by crystal violet and calculated with image J, and we found that 1 μM EHT 1864 has a small effect on GBM migration but 20 μM EHT 1864 almost halved the number of migrating GBM both for the GBM cell line U87 on day 2 and day 3 (Figure 2).

We also computed the number of migrating cells per field at different days and in the presence of different amount of the tested inhibitors. Collected data from at least three different experiments show that 50 μM ML141 blocked almost completely migration at Day1 (Figure 3B), while the action of EHT 1864 (Figure 3A) and of R-ketorolac (Figure 3C) was more prominent at Day2. This observation is consistent with the more pronounced ability of ML141 to cross the lipid membrane and act on the interior of cells.

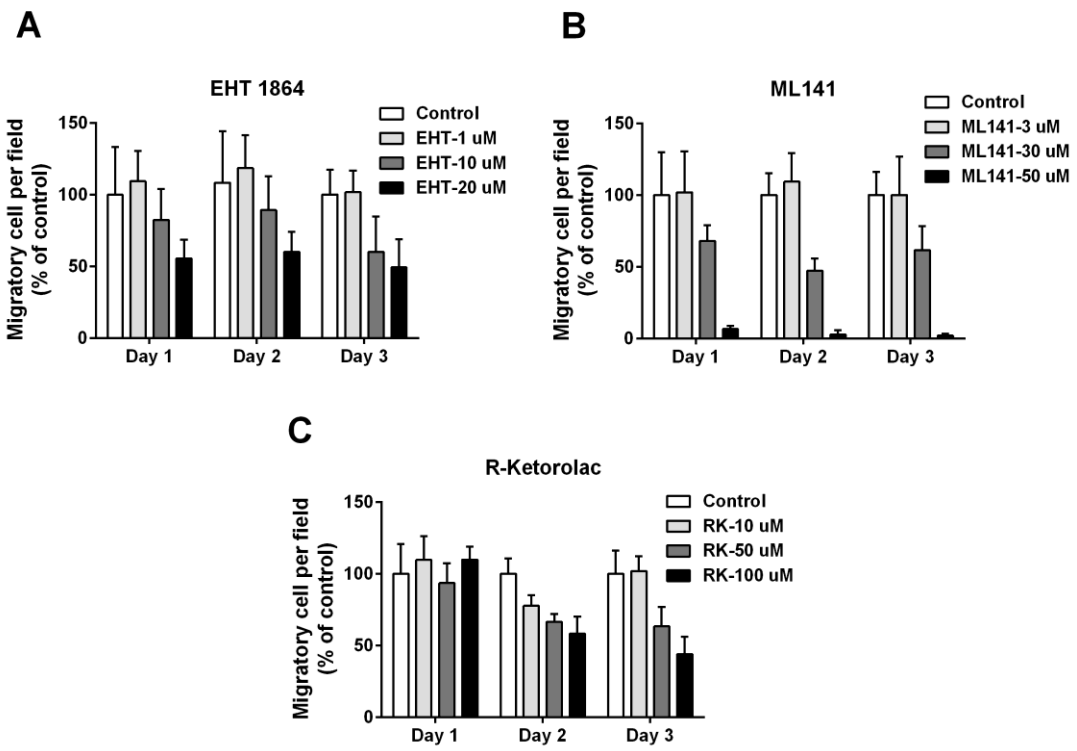

Figure 3 - Three inhibitors EHT 1864 (A), ML141 (B) and R-ketorolac (C) inhibit U87 GBM cell migration in transwell assay depending on concentration and time of treatment.

At later days, such as Day3 we observed often a higher number of cells per field (comparing Day3 and Day2 for EHT 1864 in Figure 2) than at previous days because GBM replicates. Collected data indicate that the concentration of the inhibitors blocking half of the GBM motility is approximately 20, 30 and 50 μM for EHT 1864, ML141 and R-ketorolac, respectively.

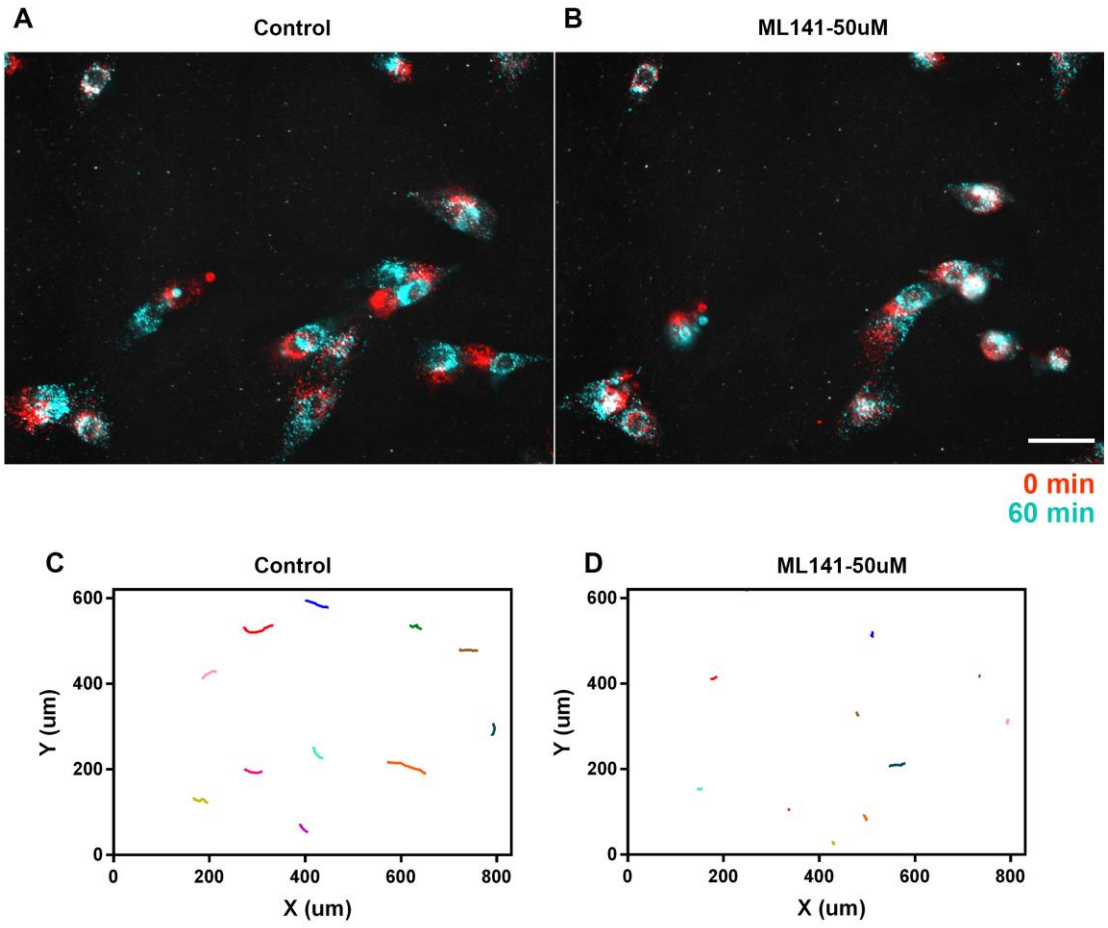

Figure 4 - ML141 inhibits U87 GBM cells motility analyzed with live cell imaging. A and B, Live cell imaging frames at different recording time points were merged before and after 50 μM of ML141 treatment. Red indicates cells at T=0 min, cyan indicates the same cells at T=60 min. When two channels are co-localized, they appear white and indicating immobilizing cells. C and D, Migration trajectories before and after 50 μM of ML141 treatment were reconstructed.

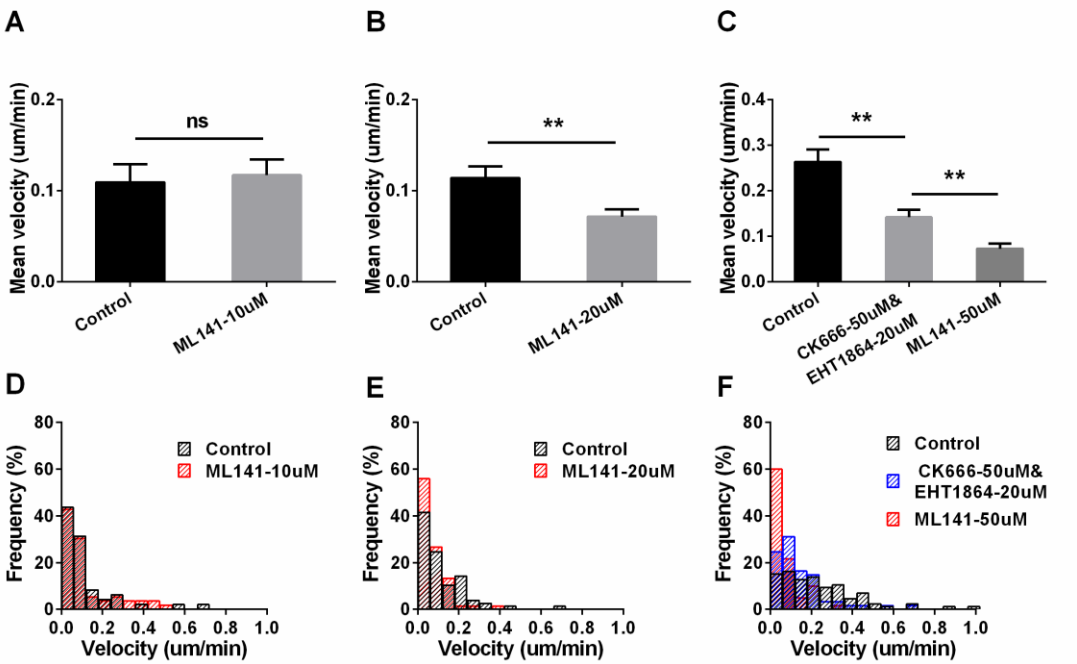

Figure 5 – Effect of ML141 on velocities of U87 GBM cells. A-C, Mean velocity was significantly decreased by 20 μM (B) and 50 μM (C) of ML141. Data were shown as mean ± sem, **p<0.01. D-F, Velocity distribution of U87 GBM cells before and after 10, 20 and 50 μM ML141 treatment.

We looked also to the action of these inhibitors with live cell imaging (Figure 4 and Figure 5) and we observed a very rapid action of ML141 on GBM motility: the addition of 50 μM halved the motility with some minutes and similarly EHT 1864 had a rather fast action. In contrast, we could not detect a fast action of R-ketorolac, presumably because of the presence of the carboxylic group which limits its ability to cross the lipid membrane. The inhibitory action of R-ketorolac is best seen with the transwell assay and requires at least 24 hours.

Live cell imaging allows the tracking over time of an individual migrating GBM and therefore provides an estimate of the mean velocity of migrating cells. As GBM cells replicate very efficiently, both the transwell assay and live cell imaging are not exempt of limitations: in the presence of a high replication activity the transwell assay can underestimate the effect of an inhibitor and the live cell

imaging tracking can be confused during a mitosis. Nevertheless, the combination of the two assays provides a reliable characterization of the effect of the used inhibitors on GBM motility.

Molecular mechanism of inhibition from molecular simulations

According to the experiments reported above the tested inhibitors (Figure 3), known to target the Rac1 and Cdc42 proteins, were able to reduce the migration and/or the infiltration propensity of the U87 cell lines. As such, we employed docking and all atom explicitly solvated classical MD simulations to unveil the molecular mechanism of inhibition of the above mentioned inhibitors.

Identification of the inhibitor's binding pose via docking and Molecular Dynamics simulations

Since all drugs are known to exert a non-competitive inhibition mechanism (i.e. the do exert inhibition of the small-molecule inhibitor without competing with their natural cofactor (i.e. Guanine Triphosphate (GTP) cofactor), we have initially identified possible binding cavities, distinct from the GTP binding site, possibly able to host these small molecule. This search was done considering both the GTP and GDP-bound form of the proteins, which represent their active and inactive form, respectively. In the GDP-bound form of the proteins, we identified by using site detector algorithms two cavities (sites 1 and 2) on Cdc42 and only one cavity (Site 1) on Rac1 potentially able to bind the inhibitors. No cavity was instead present in the GTP bound form of the protein. In order, to assess the druggability of these pockets, we docked the investigated inhibitors on site1, which flanks the GTP binding cavity. Remarkably only the R-enantiomer of R-ketorolac and of ML141 could be docked in this site, consistently with experimental findings showing inhibitory activity on Rho GTPases, exclusively for this enantiomer. The binding stability of the drug, was monitored by performing 100-400 ns long MD simulations for each drug/GTPase adduct. Site 2, identified

exclusively for Cdc42, is rather small and flexible. As a result, all molecules docked in this site rapidly dissociated within the first 30 ns MD simulations. This first set of simulations unprecedentedly allowed to predict the binding pose of R-ketorolac and ML141 on Cdc42 and that of R-ketorolac and EHT 1864 on Rac1 (Figure 6). In the following we perform systematic analysis to unravel the molecular mechanism exerted by the used inhibitors on the small Rho GTPases.

Inhibition mechanism of Cdc42

We initially focused in dissecting the inhibition mechanism of the two investigated Cdc42 inhibitors. (Figure 6A and B). Different non-competitive mechanisms may be operative for small Rho GTPases depending if the inhibitors exert their action by interfering with the GTP or GEF biding [20]. Our set of simulations predict that the carboxylic moiety of R-ketorolac coordinates the Mg^{2+} ion. This coordination may weaken the interaction of the metal ion with the GDP phosphates. This coordination may facilitate the release of GDP cofactor release from Cdc42 and/or preventing the binding of a new GTP molecule in an optimal position to undergo a new cycle. Thus, consistently with experimental evidences, R-ketorolac, can be classified as a GTP binding inhibitor, possibly. Additionally, the aromatic ring of R-ketorolac lies in the vicinity of the switch II region, where the GEF proteins have been demonstrated to bind in crystallographic studies, possibly interfering with the binding of these proteins (Figure 6).

At variance of R-ketorolac, the binding pose of ML141 predicted from docking and MD simulations reveals that the drug protrudes towards the Mg^{2+} ion site with its amine moiety (Figure 6B). Its interaction with the Mg2+ ion and with the pocket flanking the GDP binding site confirm its interference also with the GDP/GTP binding, as suggested experimentally. Also one of the aromatic ring of ML141 heads toward the small cavity lined by switch II also approaches the GEF binding pocket nearby the Phe56 residue (Figure 6).

We next inspected the impact of R-ketorolac and ML141 on the structural and functional properties of Cdc42, by monitoring the RMSF of the drug/protein adduct as compared to that of the Cdc42 protein *per se*. Ostensibly, the regions mostly affected by drug binding are those corresponding to switches I and II for R-ketorolac, whose flexibility surprisingly increase upon drug binding. In contrast, ML141 only slightly affects the switch I. In order to understand how drug binding could impact the internal motion of the protein we also computed the per-residue cross-correlation matrix (CCM). Positive regions of the CCM indicate dynamically coupled regions, associated to a lock step motion of the protein, while negative regions indicate the negatively correlated motion with the corresponding parts of the protein moving in an opposite manner [21]. The CCM of the GDP bound-Cdc42 shows a dynamical coupling of two functionally relevant regions, switch I and switch II, with switch I being moving in a lockstep motion with α1, α4, β6 and β1, while being negatively correlated with αi (Figure 7A) and switch II being negatively correlated with switch I, β1 and αi. This is consistent with an opening/closing motion of the switch I disclosed by the essential dynamics of the proteins (Figure 8), which capture the most relevant slow vibrational motion of the protein. The observed movement of the GDP-bound Cdc42 is most likely instrumental to the loading/release of the GTP/GDP cofactor, and to engage the interactions with the variety of protein effectors that mediate the small Rho GTPase signaling. To monitor the impact of the R-ketorolac and ML141 binding on these internal motion of Cdc42 we also computed the CCM of the drug-bound protein. This CCM, plotted as a difference with respect to the undrugged form of the protein (Figure 7B, C), reveals that both drugs dampen the overall internal motion of the Cdc42 (Figure 8) thus preventing the GTP/GDP exchange and Rho GTPase activation.

The computed binding free energy (ΔG_b) of both drugs to Cdc42 revealed that the binding of R-ketorolac to Cdc42 (ΔG_b, of -154 ± 5 kcal/mol) is energetically favored with respect to that of ML141 (ΔG_b, of -45 ± 6 kcal/mol). The electrostatic

interactions between the negatively charged carboxyl moiety of R-ketorolac and the Mg^{2+} ion markedly contribute to the ΔG_b. In addition, residues Lys16 and Val36 stabilize drug binding by establishing electrostatic and hydrophobic interactions, respectively. We remark that the computed ΔGb are calculated rely on force fields and neglect the electronic rearrangements of the charge density induced by the Mg^{2+} ions (charge transfer and polarization effects) to the coordinating ligands. As a result, the calculated ΔG_b is most likely overestimated [22]. In addition to Lys16 also Phe37, Ala59 and Tyr64 contribute to the ΔG_b of ML141 by establishing hydrophobic interactions. Surprisingly, none of the two drugs establishes persistent H-bonds with their binding pocket.

As a further check we monitored if ML141 could bind at the Cdc42/GEF interface. Indeed, small molecules able of stabilizing the GEF/GTPase adduct may permanently inactivate the GTPase cycle. Among the GEF proteins known to bind to Cdc42 we selected Dock9 since an X-ray structure of this protein in complex with Cdc42 is available. Thus, ML141 was docked in a cavity at the interface of Cdc42/Dock9, and the resulting binding pose of ML141 resulted to be stable in MD simulations. The binding of ML141 had a limited impact on the Cdc42/Dock9 flexibility (i.e. does not markedly affected the RMSF of the two switch regions, which, in the adduct, are locked by Dock9). Upon ML141 binding an increase of positive correlation of the two Cdc42 switches is observed (Figure 7D), underlining a partial recovery of Cdc42 internal motion which, counteracts the stability of Dock9 binding. Consistently, the ΔG_b of ML141 at the Dock9/Cdc42 interface is smaller than in the single Cdc42 protein (ΔG_b = -28 ± 3 kcal/mol) being stabilized by hydrophobic and electrostatic interactions with residues Gln342, Glu403, respectively, from Dock9 and with hydrophobic interactions with Leu67 from Cdc42. This suggests that ML141 most likely bind to site 1 of Cdc42 protein, in line with its activity as nucleotide binding inhibitors suggested experimentally.

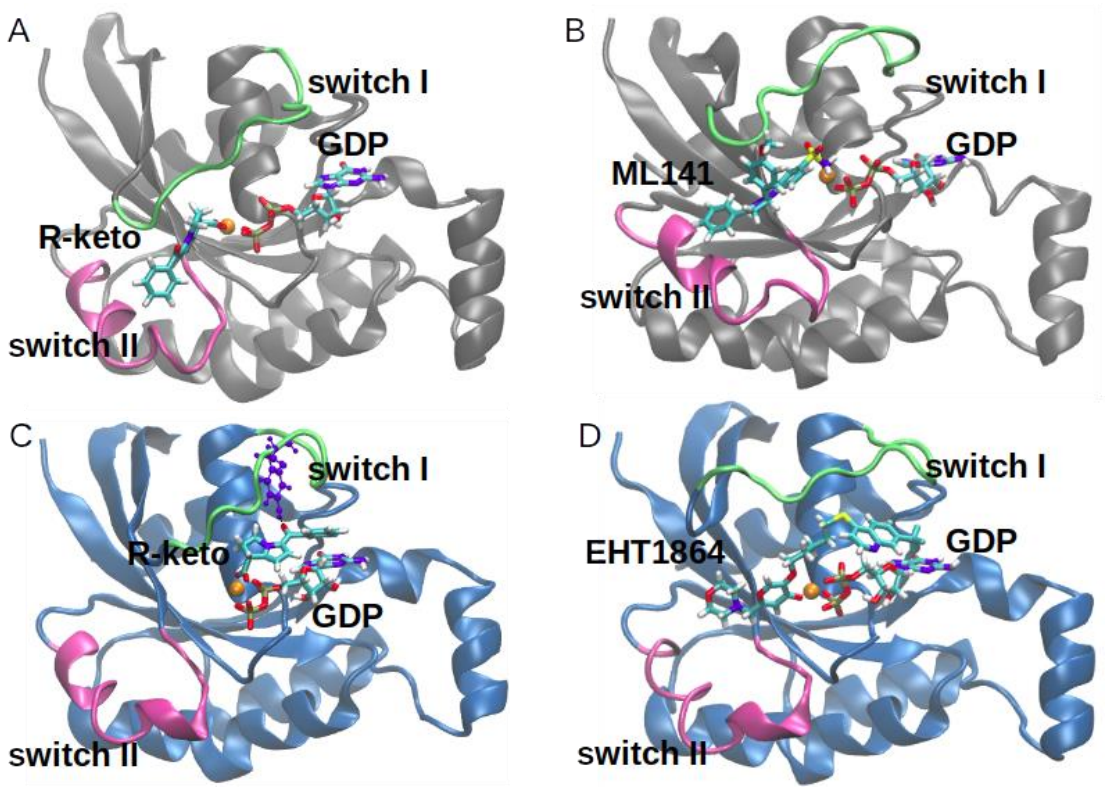

Figure 6 – Binding pose of R-ketorolac (R-keto, A) and ML141 (B) on Cdc42, R-keto (C) and EHT 1864, (D) on Rac1. Cdc42 and Rac1 are shown in gray and blue new cartoons, respectively, switch I (from residue 27 to residue 37) and II (from residue 59 to residue 73) in lime and mauve, respectively, Mg^{2+} ions is pictured in orange van deer Waals sphere and Guanine diphosphate (GDP) and the inhibitors are shown as licorice and colored by atom name. In C the hydrogen bond between R-keto and Tyr32 (depicted as blue balls and sticks) of Rac1 is shown.

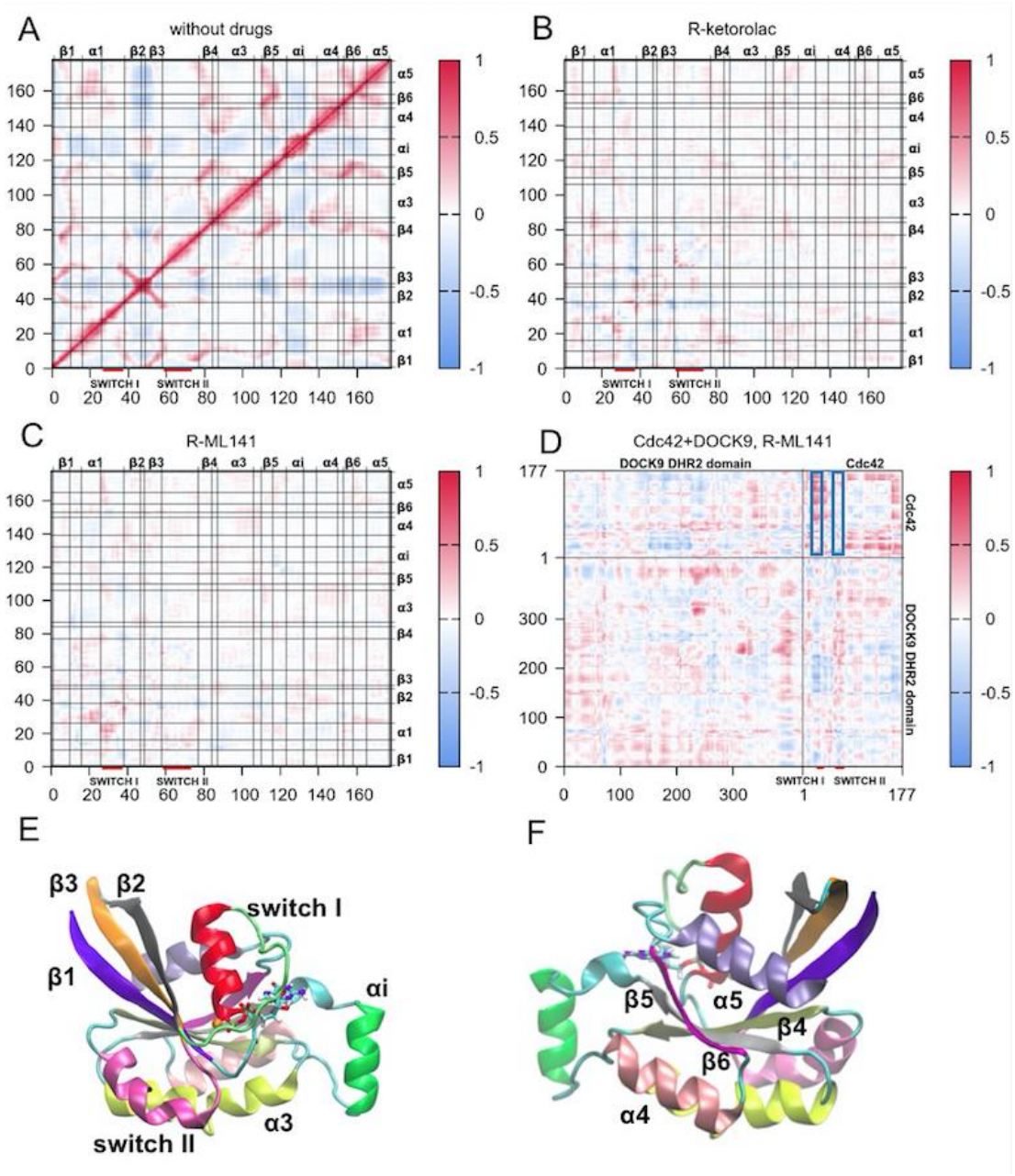

Figure 7 – Per-residue cross correlation matrix (CCM) of Guanine diphosphate (GDP)-bound Cdc42 (A). Difference between the per-residue CCM of GDP-bound Cdc42 in complex with R-ketorolac (B) and ML141 (C) and Cdc42 and the CCM of GDP-bound Cdc42 without drug. Difference between the per-residue CCM of GDP-bound Cdc42 in upon binding of Dock9 and ML141 and the CCM of GDP-bound Cdc42 alone (D). The Pearson's cross correlation coefficients vary from -1 (anticorrelated motion, blue) to +1

(correlated motion, red). Horizontal and vertical lines define different regions of the protein: β1 (residues 1 to 10), α1 (residues 16 to 26), β2 (residues 38 to 47), β3 (residues 49 to 58), β4 (residues 77 to 84), α3 (residues 87 to 106), β5 (residues 110 to 116), αi (residues 123 to 132), α4 (residues 139 to 150), β6 (residues 153 to 158), α5 (residues 165 to 177). Domain partitioning of Cdc42 is shown in E and F. Residues corresponding to switch I and II are highlighted by red lines.

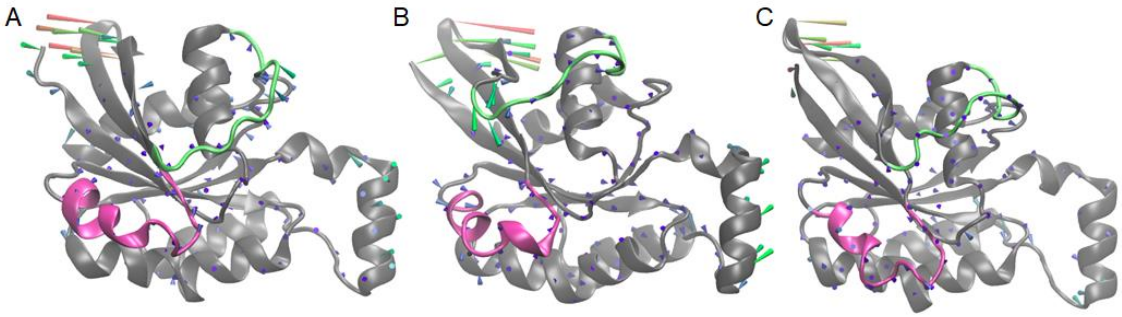

Figure 8 – Porcupine plot representing the essential dynamics of Cdc42 in the GDP-bound form (A), in complex with R-ketorolac (B), with ML141 (C). Cdc42 is depicted in gray new cartoons, with switch I and II highlighted in lime and mauve, respectively. The arrows indicate the direction of the motion, their length and color (from blue to red) is representative of the motion amplitude.

Inhibition Mechanism of Rac1

The same simulation protocol was also instrumental to elucidate the binding mode and the inhibition mechanism of R-ketorolac and EHT 1864 to Rac1. Also in this case docking and MD simulations predict that both drugs bind nearby the GDP binding site. R-ketorolac coordinates the Mg^{2+} ion with its carboxylic moiety, similarly to what observed in Cdc42, while EHT 1864 occupies the cavity between the GDP molecule and switch I (Figure 6). In spite of the structural similarity of Cdc42 and Rac1, the pocket lined by switch II is smaller in Rac1 that in Cdc42 due to the presence of Trp56 in the first as compared to Phe56 in the latter. As a result, the aromatic ring of R-ketorolac in Rac1 lines switch I, being stabilized by π-stacking interaction with the GDP cofactor (Figure 6). Consistently

with the binding poses observed, both drugs upon binding to Rac1 (Figure 6C and D) principally perturb switch I. Interestingly, the binding of the studied inhibitors locks the internal dynamics of the protein, hampering the opening/closing motion of the switch loops, (Figure 9) upon R-ketorolac binding. Conversely, EHT 1864 does not interfere with the Rac1's internal dynamics. The CCM of both systems also highlights marked differences. While R-ketorolac introduces small changes in the per-residue CCM (Figure 10), EHT 1864 largely perturbs the protein dynamics increasing the negatively/positively coupled motions of switch I and II respectively (Figure 10).

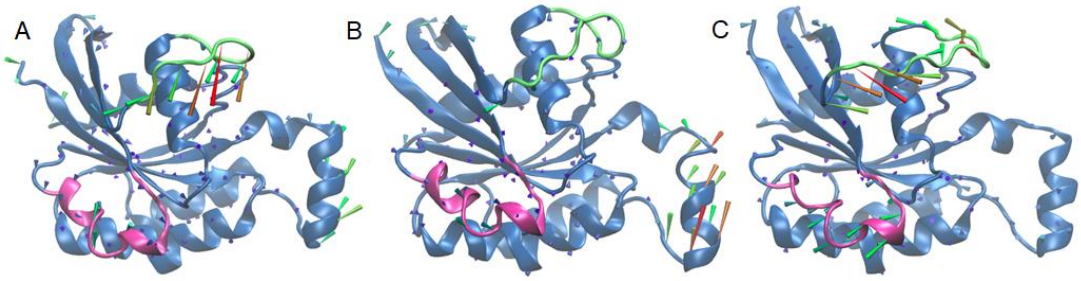

Figure 9 – Porcupine plot representing the essential dynamics of Rac1 in the free GDP bound form (A), in complex with R-ketorolac (B), in complex with EHT 1864 (C). Cdc42 is depicted in blue new cartoons, with switch I and II highlighted in lime and mauve, respectively. The arrows indicate the direction of the motion, their length and color (from blue to red) is representative of the motion amplitude.

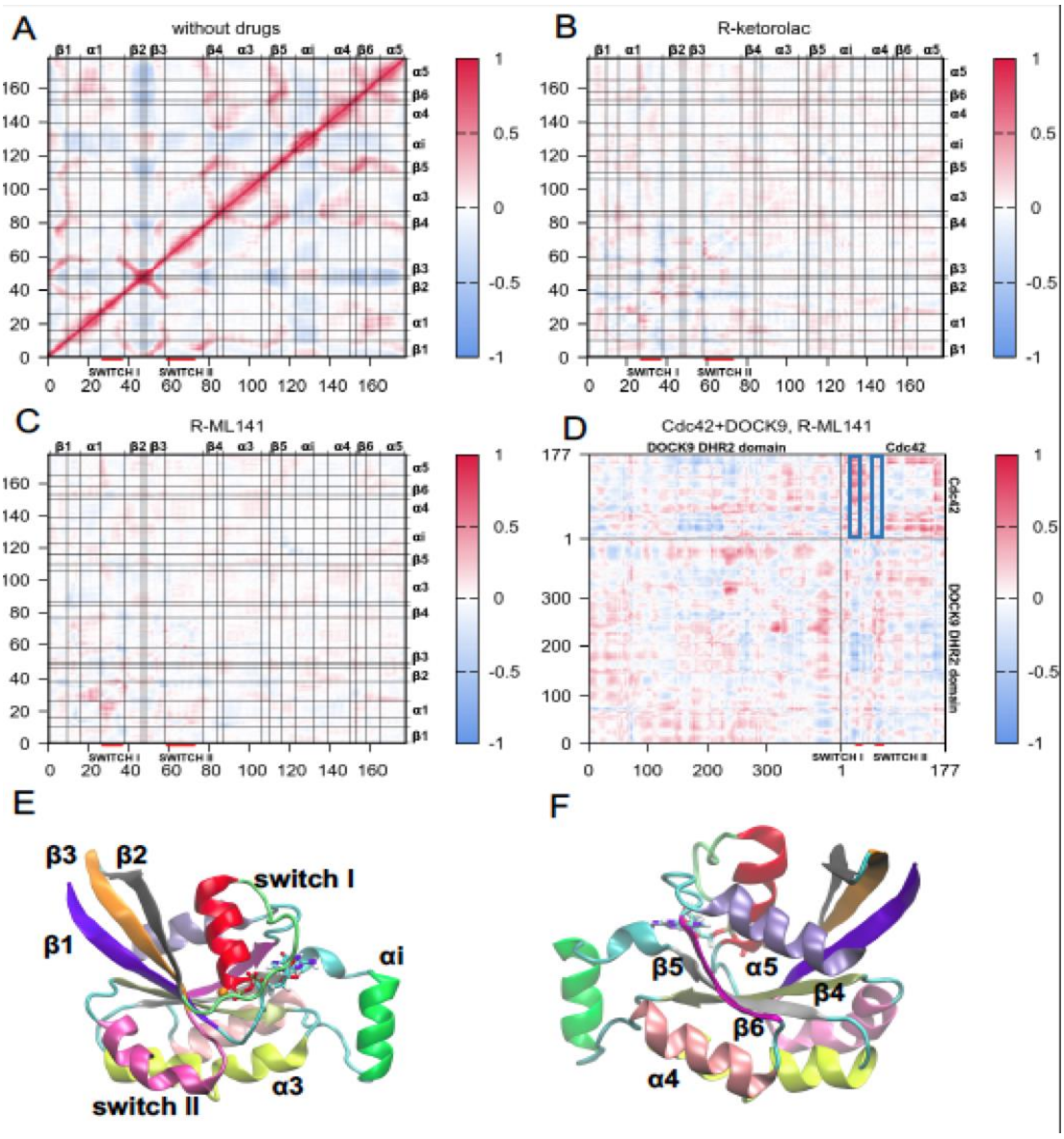

Figure 10 – Per-residue correlation matrix (CCM) for the GDP bound form of Rac1 (A). Difference between the per residue CCM of GDP-bound Rac1 in complex with R-ketorolac (B) and EHT 1864, charge +1 (C) and the same form of the protein without drugs. Difference between the per-residue CCM of GDP-bound Rac1 in complex with Dock2 and EHT 1864, charge +1, and the same form of the protein without drugs (D). The Pearson's cross correlation coefficients vary from -1 (blue, anti-correlated motion) to +1 (red, correlated motion). Horizontal and vertical lines define different regions of the protein: β1 (residues 1 to 10), α1 (residues 16 to 26), β2 (residues 38 to 47), β3 (residues 49 to 58), β4 (residues 77 to 84), α3 (residues 87 to 106), β5 (residues 110 to

116), αi (residues 123 to 132), α4 (residues 139 to 150), β6 (residues 153 to 158), α5 (residues 165 to 177). Domain partitioning of Rac1 is shown in E and F. Switch I and II are highlighted by red lines under the matrices.

The calculated ΔG_bs reveal that R-ketorolac binds more strongly than EH1864 to Rac1 (ΔG_b=-182 ± 7 kcal/mol and ΔG_b=-62 ± 9 kcal/mol for R-ketorolac and EHT 1864, respectively) and that R-ketorolac has a larger binding affinity towards Rac1 than to Cdc42, consistently with its higher potency (lower IC_{50}) [20]. Similarly to its binding pose in Cdc42, the binding of R-ketorolac is mostly due to the electrostatic interactions of its carboxyl moiety with the Mg^{2+} ions, being here further stabilized by electrostatic interactions with Tyr32, and by hydrophobic interactions with Cys18 and Pro29. Its binding pose is also stabilized by a persistent H-bond formed between the hydroxyl group of Tyr32 and its carbonyl oxygen. In contrast, the binding of EHT 1864, mostly establishes hydrophobic interactions with the binding pocket and electrostatic interactions between its amine moiety of the drug and Asp38.

As in the Cdc42 case, we also monitored if EHT 1864 could bind at the interface of Rac1 and a specific GEF, i.e. Dock2 for which a crystal structure was available. Docking simulations followed by MD simulation confirmed once more the presence of a druggable pocket at the Rac1/Dock2 interface. The binding of EHT 1864 at this site induces a slight increase of the switch I flexibility. Consistently, the CCM of the Rac1/EHT 1864 adduct registers an increase of the positive correlation (Figure 10) of this critical region. Therefore, the binding of EHT 1864 at the Rac1/Dock2 is not effective in blocking functional dynamics of protein, but rather destabilized the Rca1/Dock2 adduct. This is further confirmed by a decrease of the ΔG_b (-28 ± 6 kcal/mol) with respect to that of EHT 1864 binding to Rac1. Constituently with its suggested activity as nucleotide binding inhibitor EHT 1864 most likely targets the Rac1 rather than the Rca1/Dock2 adduct.

Discussion

The present study illustrates the effect of three inhibitors R-ketorolac, ML141 and EHT 1864 on the migration and motility of GBM and a detailed analysis based on all-atom simulations elucidates the binding pose and the mechanism of these inhibitors on two small GTPases, Cdc42 and Rac1, involved in cellular motility. The complementary use of the two approaches provide a better insight and it is important also to clearly understand their differences.

In vivo and in silico comparison

In the experimental analysis shown in Figure 2-5, the inhibitors are added to the extracellular medium bathing the GBM and therefore these drugs must cross the cellular membrane before interacting with Rac1 and Cdc42. Therefore, it is expected that the concentration of the inhibitors halving half of the migration $K_{1/2migration}$ to be different from the concentration inhibiting half of Rac1 and Cdc42 activity in *in vitro* conditions. From the transwell experiments performed in U87 GBM cell line we have estimated that $K_{1/2migration}$ to be approximately 20, 30 and 50 μM for EHT 1864, ML141 and R-ketorolac, respectively. For EHT 1864, the corresponding values obtained in vitro conditions are 1-5 μM [19], and 20 μM on MDA-MB-231 and MCF-7 breast cancer cells [23]. For ML141, 2 μM in vitro conditions [24], 3 μM for 50% reduction on ovarian cancer cell migration [18]. R-ketorolac against Rac1 and Cdc42 in Hela cells with values of 0.57 μM and 1.01 μM [25], respectively. The reduced efficacy of the compounds, as compared to in vitro tests and migration characteristics in other cell line types, suggest that other pathways may also be relevant to stop the infiltration and migration propensities of the GBM.

Switches, binding and docking sites in Cdc42 and Rac1

The set of docking and MD simulations performed supply a molecular basis for the inhibition mechanism exerted by the known GTPase inhibitors tested in this

study. R-ketorolac, bearing a carboxylic moiety, coordinates the Mg^{2+} ions, in line with the high affinity of carboxylic moieties towards Mg^{2+} ions observed in protein enzymes. Its binding may reduce the binding strength of GDP towards the Mg^{2+} metal triggering GDP dissociation and inactivating the small Rho GTPase function by hampering the GDP/GTP exchange. Nevertheless, the binding of R-ketorolac is slightly different in Cdc42 and Rac1, where in the first both switch I and II regions are lined by the drug hampering the opening/closing motion of the cavity and possibly affecting also the interactions with the GEF proteins in Cdc42. Conversely, when binding to Rac1 R-ketorolac exclusively affects the switch I, which is less involved in the GEF interaction/stabilization. The discussed difference in the binding poses is also confirmed also by the predicted binding mode of ML141 and EHT 1864, the first heading towards the switch II cavity, while the second being mainly and mostly lined by switch I. While ML141 engages strong interactions with the cavity and hampers the typical opening/closing motion of the switches I/II, which necessary to GTP/GDP upload/release. Conversely, in spite of its larger size EHT 1864, does not completely freeze the movement of Rac1. Being Rho GTPases at the cross road of an intricate signaling interactome and being their action co-adjuvated by several interacting partners, we have attempted at predicting if/how the binding of the studied inhibitors could differently affect the interactions with selected proteins. Notably, by superimposing the drug-bound form of Rac1/Cdc42 proteins with selected Rho GTPase partners, for which the crystal structure in complex with their partner GTPase is available, it emerges that R-ketorolac and EHT 1864 appears to counteract the binding of specific Rac1 protein partner, plexin B1 [26]. P-Rex1 and Epithelial cell transforming protein 2 (ETC2) [27], among the others which are involved in GBM migration and invasive propensity, while affecting to a lower extent the interaction with a typical GEF such as Dock2. Conversely the binding of both R-ketorolac and ML141 appears to potentially have an impact even on GEF (Dock9) binding.

Specific actions of R-ketorolac, ML141 and EHT 1864

Migration and motility in cells is regulated by a complex and highly interconnected network of proteins. Therefore, pharmacological inhibition of these proteins simultaneously could be of therapeutic benefit.

R-ketorolac is an inhibitor both of Rac1 and Cdc42, while ML141 is more specific for Cdc42 and EHT 1864 inhibits Rac1 preferentially. According to previous research, in melanoma Rac1 is not only overexpressed but also mutated [28]. The knockdown of Rac1 in melanoma cells depresses the formation of invadopodia [29], and in this case decreases its capacity to promote cancer metastasis. The already approved drug R-ketorolac and in particular its R-enantiomer inhibits Rac1 and Cdc4 in ovarian cancer [30], and potentially contributes to the observed survival benefit. This observation suggest to use the same drug for treating glioma/GBM at their early stages also in the case of brain cancer. R-ketorolac is a drug already approved by the US Food and Drug Administration (FDA) in 1989, while ML141 and EHT 1864 not yet at the moment. Therefore, to study the molecular mechanism and working concentration of these three inhibitors will benefit the clinical promotion and use.

Materials and methods

Cell culture

U87 GBM cells (#89081402, Sigma-Aldrich) were cultured in DMEM supplemented with 10% fetal bovine serum (FBS; Invitrogen, Life Technologies, Gaithersburg, MD), 1% PenStrep (100 U/ml penicillin and 100 µg/ml streptomycin; Invitrogen). The GFP-labelled U87 GBM cells were infected by a mix containing lentiviral vector, LV-GFP. All the cells were cultured in an incubator at 37°C, 5% CO_2, 95% relative humidity and medium was replaced every 3 days. Once 70–80% of confluence had been reached, the cells were re-plated at a density of $2.5\times10^3/cm^2$.

Transwell assay

5×10^5 U87 GBM cells in DMEM medium (without FBS) were seeded to the top chambers of 12-well transwell plates (Millipore; 8 µm pore size), and 10% FBS DMEM medium was added to the well. Inhibitors were employed in both the chamber and the well. After incubation for indicated time, cells in the top of the chamber (non-migrating cells) were removed from the chambers, and cells in the bottom of the chamber (migrating cells) were fixed with 4% PFA for 20 min and stained with 5% crystal violet for 30 min in room temperature. The migrated cells were counted with a microscope.

Live-cell imaging

GFP labelled U87 GBM cells were plated at a density of 8.0×10^4 cells into 35-mm dishes with a glass bottom and cultured for 1 day. Live-cell imaging experiments were performed on an epi-fluorescence microscope (Nikon Ti2-E) equipped with a chamber incubator and light-emitting diode (LED) illumination (λ=490 nm for). During all imaging experiments, cells were kept at 37°C, 5% CO_2 and 95% humidity. Time-lapse images were taken with 50 ms of exposure time and one image was taken every 2 min. The videos were analysed using the Fiji plugin

TrackMate [31], which allows the selection of regions of interest (ROIs) for every cell and obtain the average velocities for each cell.

Computational model building

The starting configurations for the building the models of the Cdc42 and Rac1 proteins were taken from the crystal structures deposited in the protein data bank (PDB) (PDBid 5CJP and 2YIN, for Cdc42 and Rac1, respectively). Conversely, in order to investigate the binding of the drug at the interface with the specific GEF proteins, we used the crystal structures of Dock9/Cdc42 and Dock2/Rac1 complexes with Cdc42 and Rac1 deposited in the PDB (PDB id 2WMO and 2YIN). For each system the protein structures were prepared, and the protonation state of the ionizable residues was determined by using Schödinger software suite.

Since the investigated inhibitors are known to act via a non-competitive mechanism (i.e. they do not compete with the GTP substrate) we initially looked for possible binding pockets able to host the inhibitors studies here, following an already established computational protocol [32]. To this aim we used the SiteMap [33] and FTMap softwares [34]. The search of druggable pockets was carried on the crystal structure of the proteins and on selected frames of the equilibrated molecular dynamics (MD) trajectories of each protein in the Guanine triphosphate (GTP) and Guanine diphosphate (GDP) bound state. As a result, we identified two possible druggable pockets on Cdc42 and one pocket on Rac1. Docking simulations of the experimentally tested inhibitors were then performed to find a binding pose of the drugs on these pockets, following an ensemble docking approach [35]. Namely, we used as target protein structures: (i) the crystal structure of Rac1 and Cdc42 in the free form and the protein structure in complex with their specific GEFs, (ii) a representative of the equilibrated part of the simulation trajectory selected by a cluster analysis; (iii) a visually selected trajectory frame of the GDP- bound form of the proteins in which the pockets

were able to accommodate the studied inhibitors. Prior to performing docking simulations, each drug was prepared considering all possible protonation states. Docking simulations were done with the Glide program of the Schödinger suite.

As a result, the R-ketorolac was considered in its negative, R-ML141 in its neutral and EHT 1864 in its positive form, which are predicted to be the most abundant at physiological pH.

Molecular dynamics (MD) simulations

The topology of the system was built with the Amber2018 tool *tleap* using the amber ff1ILDN force field (FF) [36]. The parameters of the GTP and GDP cofactors and of the tested drugs were built according to the following procedure: each molecule was subjected to a structure minimization using the Jaguar program at density functional theory (DFT) B3LYP level of theory and the 6-31G** basis set. Next, electrostatic potential (ESP) derived charges were computed according to the Merz-Kolmann partitioning scheme using the Gaussian software (Gaussian 09, R. A. G. I., Wallingford CT, 2016). With the same basis set, and converted in RESP charges with the resp module of amber tools 2018. For the other FF parameters the general amber force field (Gaff) was employed [37]. For the Mg^{2+} ion present in the active site we used the Aqvist parameters [38]. The systems were solvated by adding a layer of 10 Angstrom of TIP3P water molecules [39] and neutralized with Na^{+} ions, using the Joung and Cheatman parameters [40]. This lead to a total number of 44662 atoms for GDP-bound Cdc42, 35813 atoms for GDP-bound Cdc42 in complex with R-ketorolac, 36611 atoms for GDP-bound Cdc42 in complex withML141; 92293 atoms for GDP-bound in complex with Cdc42 and Dock9 ; 92310 atoms for for GDP-bound Cdc42 in complex with ML141 and Dock9; 34986 atoms for GDP-bound Rac1, 34739 atoms for GDP-bound Rac1 +R-ketorolac, 34415 atoms for GDP-bound Rac1 in complex with EHT 1864; 95331 atoms for GDP-bound Rac1 in complex with Dock2 and 95156 atoms for GDP-bound Rac1 in complex with Dock2 + EHT

1864. Overall ten different systems were simulated and extensively analyzed in this study. The system topology was then converted to the GROMACS format with the acpype software [41].

A short minimization was run before annealing the system to 300K. The pressure was equilibrated to 1atm using the Berendsen barostat. In the simulations with the drugs, after equilibration the position of the drug in the binding site was restrained for 30 ns and subsequently a production run was started removing the constraint. For all simulations the pressure was kept to equilibrium value with the Parrinello-Rahman barostat [42] while the temperature was controlled with the velocity rescale thermostat [43]. The length of the simulations of Cdc42 and Rac1 without drugs is 440 ns.

Analysis

The root mean square deviation (RMSD), the root mean square fluctuation (RMSF), the principal component analysis (PCA) and the per residue correlation matrix were derived using both GROMACS2018 [44] and Amber 18 programs [45]. In particular the GROMACS2018 tools were used to compute the RMSD (gmx rms) and RMSF (gmx rmsf), while the hydrogen (H)-bonds and cross correlation matrix were computed with the AMBER2018 tool *cpptraj*. A cluster analysis was performed with the GROMACS2018 cluster tool using the algorithm described in Daura's report *[46]*. Only Cα atoms of each residue were considered to compute RMSD, RMSF and correlation matrix. To compute the RMSD the whole trajectory was used, while all other properties were evaluated on a stable (almost flat RMDS) final 100 ns part of the whole trajectory. The PCA was performed with the GROMACS 2018 tools (gmx covar, gmx anaeig). To obtain the PCs we applied the following protocol: the trajectory was first fitted on the reference structure to remove translational and rotational motion, then the mass-weighted covariance matrix was computed for the Cα atoms and diagonalized [21]. The eigenvectors exhibiting the largest eigenvalues pinpoint the most relevant motions sampled during the simulation, which is also referred to as principal components (PCs) [47].

The motion along the first eigenvector (essential dynamics), i.e. the vector corresponding to the largest eigenvalue, is commonly referred as essential dynamics and represents the most relevant motion of the system. This was visualized with the VMD program, and arrows highlighting the direction of motion were drawn using the porcupineplot.tcl plugin of the VMD program.

Energetic analysis.

Binding free energies between the proteins and selected ligands (ΔG_b) were calculated by using the Molecular Mechanics-Generalized Born Surface Area (MM-GBSA) method [48] with Amber18 also using the per-residue decomposition

tool to gain a direct view of how each residue lining the binding site contributes to drug-binding. The value of the igb flag was set to 2 and a salt concentration of 0.1 M was used. MM-GBSA calculations were performed on 100 equally distant frames the last 100 ns part of the equilibrated MD trajectory, following a protocol used in previous studies. The conformational entropic contribution of the free energy was not considered, as this term usually does not improve the quality of the results [49]. For what concerns the energetic contribution of each residue in the protein we used a threshold of 1 kcal/mol, absolute value, above which one residue was considered as significant in favoring/disfavoring the binding of the drug.

Reference

1. M. Weller, P. Roth, M. Preusser, et al., *Vaccine-based immunotherapeutic approaches to gliomas and beyond.* Nat Rev Neurol, 2017. **13**(6): p. 363-374.
2. S.J. Bagley, A.S. Desai, G.P. Linette, et al., *CAR T-cell therapy for glioblastoma: recent clinical advances and future challenges.* Neuro Oncol, 2018. **20**(11): p. 1429-1438.
3. R.J. Diaz, S. Ali, M.G. Qadir, et al., *The role of bevacizumab in the treatment of glioblastoma.* J Neurooncol, 2017. **133**(3): p. 455-467.
4. A.A. Thomas, C.W. Brennan, L.M. DeAngelis, et al., *Emerging therapies for glioblastoma.* JAMA Neurol, 2014. **71**(11): p. 1437-1444.
5. R. Stupp, W.P. Mason, M.J. van den Bent, et al., *Radiotherapy plus concomitant and adjuvant temozolomide for glioblastoma.* N Engl J Med, 2005. **352**(10): p. 987-996.
6. K.P.L. Bhat, V. Balasubramaniyan, B. Vaillant, et al., *Mesenchymal differentiation mediated by NF-kappaB promotes radiation resistance in glioblastoma.* Cancer Cell, 2013. **24**(3): p. 331-346.
7. J. Behnan, G. Finocchiaro, and G. Hanna, *The landscape of the mesenchymal signature in brain tumours.* Brain, 2019. **142**(4): p. 847-866.
8. C.W. Pak, K.C. Flynn, and J.R. Bamburg, *Actin-binding proteins take the reins in growth cones.* Nat Rev Neurosci, 2008. **9**(2): p. 136-147.
9. T.R. Stankiewicz and D.A. Linseman, *Rho family GTPases: key players in neuronal development, neuronal survival, and neurodegeneration.* Front Cell Neurosci, 2014. **8**: p. 314.
10. W.A. Sayyad, P. Fabris, and V. Torre, *The Role of Rac1 in the Growth Cone Dynamics and Force Generation of DRG Neurons.* PLoS One, 2016. **11**(1): p. e0146842.
11. A.J. Ridley, H.F. Paterson, C.L. Johnston, et al., *The small GTP-binding protein rac regulates growth factor-induced membrane ruffling.* Cell, 1992. **70**(3): p. 401-410.
12. C.D. Nobes and A. Hall, *Rho, rac, and cdc42 GTPases regulate the assembly of multimolecular focal complexes associated with actin stress fibers, lamellipodia, and filopodia.* Cell, 1995. **81**(1): p. 53-62.
13. A.J. Ridley, *Rho GTPases and actin dynamics in membrane protrusions and vesicle trafficking.* Trends Cell Biol, 2006. **16**(10): p. 522-529.
14. A. Hall, *Rho family GTPases.* Biochem Soc Trans, 2012. **40**(6): p. 1378-1382.
15. S. Etienne-Manneville and A. Hall, *Rho GTPases in cell biology.* Nature, 2002. **420**(6916): p. 629-635.
16. X. Chi, S. Wang, Y. Huang, et al., *Roles of rho GTPases in intracellular transport and cellular transformation.* Int J Mol Sci, 2013. **14**(4): p. 7089-7108.
17. Y. Guo, S.R. Kenney, C.Y. Muller, et al., *R-Ketorolac Targets Cdc42 and Rac1 and Alters Ovarian Cancer Cell Behaviors Critical for Invasion and Metastasis.* Mol Cancer Ther, 2015. **14**(10): p. 2215-2227.

18. L. Hong, S.R. Kenney, G.K. Phillips, et al., *Characterization of a Cdc42 protein inhibitor and its use as a molecular probe.* J Biol Chem, 2013. **288**(12): p. 8531-8543.
19. A. Shutes, C. Onesto, V. Picard, et al., *Specificity and mechanism of action of EHT 1864, a novel small molecule inhibitor of Rac family small GTPases.* J Biol Chem, 2007. **282**(49): p. 35666-35678.
20. M.D.M. Maldonado and S. Dharmawardhane, *Targeting Rac and Cdc42 GTPases in Cancer.* Cancer Res, 2018. **78**(12): p. 3101-3111.
21. L. Casalino, G. Palermo, A. Spinello, et al., *All-atom simulations disentangle the functional dynamics underlying gene maturation in the intron lariat spliceosome.* Proc Natl Acad Sci U S A, 2018. **115**(26): p. 6584-6589.
22. L. Casalino, G. Palermo, N. Abdurakhmonova, et al., *Development of Site-Specific Mg(2+)-RNA Force Field Parameters: A Dream or Reality? Guidelines from Combined Molecular Dynamics and Quantum Mechanics Simulations.* J Chem Theory Comput, 2017. **13**(1): p. 340-352.
23. J. Molnar, C. Fazakas, J. Hasko, et al., *Transmigration characteristics of breast cancer and melanoma cells through the brain endothelium: Role of Rac and PI3K.* Cell Adh Migr, 2016. **10**(3): p. 269-281.
24. Z. Surviladze, A. Waller, J.J. Strouse, et al., *A Potent and Selective Inhibitor of Cdc42 GTPase*, in *Probe Reports from the NIH Molecular Libraries Program*. 2010: Bethesda (MD).
25. T.I. Oprea, L.A. Sklar, J.O. Agola, et al., *Novel Activities of Select NSAID R-Enantiomers against Rac1 and Cdc42 GTPases.* PLoS One, 2015. **10**(11): p. e0142182.
26. E. Angelopoulou and C. Piperi, *Emerging role of plexins signaling in glioma progression and therapy.* Cancer Lett, 2018. **414**: p. 81-87.
27. M. Chen, H. Pan, L. Sun, et al., *Structure and regulation of human epithelial cell transforming 2 protein.* Proc Natl Acad Sci U S A, 2020. **117**(2): p. 1027-1035.
28. M. Krauthammer, Y. Kong, B.H. Ha, et al., *Exome sequencing identifies recurrent somatic RAC1 mutations in melanoma.* Nat Genet, 2012. **44**(9): p. 1006-1014.
29. O.Y. Revach, S.E. Winograd-Katz, Y. Samuels, et al., *The involvement of mutant Rac1 in the formation of invadopodia in cultured melanoma cells.* Exp Cell Res, 2016. **343**(1): p. 82-88.
30. Y. Guo, S.R. Kenney, L. Cook, et al., *A Novel Pharmacologic Activity of Ketorolac for Therapeutic Benefit in Ovarian Cancer Patients.* Clin Cancer Res, 2015. **21**(22): p. 5064-5072.
31. J.Y. Tinevez, N. Perry, J. Schindelin, et al., *TrackMate: An open and extensible platform for single-particle tracking.* Methods, 2017. **115**: p. 80-90.
32. J. Sgrignani, M. Bon, G. Colombo, et al., *Computational approaches elucidate the allosteric mechanism of human aromatase inhibition: a novel possible route to Small-molecule regulation of CYP450s activities?* J Chem Inf Model, 2014. **54**(10): p. 2856-2868.

33. T.A. Halgren, *Identifying and characterizing binding sites and assessing druggability.* J Chem Inf Model, 2009. **49**(2): p. 377-389.
34. R. Brenke, D. Kozakov, G.Y. Chuang, et al., *Fragment-based identification of druggable 'hot spots' of proteins using Fourier domain correlation techniques.* Bioinformatics, 2009. **25**(5): p. 621-627.
35. A. Spinello, S. Martini, F. Berti, et al., *Rational design of allosteric modulators of the aromatase enzyme: An unprecedented therapeutic strategy to fight breast cancer.* Eur J Med Chem, 2019. **168**: p. 253-262.
36. J.A. Maier, C. Martinez, K. Kasavajhala, et al., *ff14SB: Improving the Accuracy of Protein Side Chain and Backbone Parameters from ff99SB.* J Chem Theory Comput, 2015. **11**(8): p. 3696-3713.
37. J. Wang, R.M. Wolf, J.W. Caldwell, et al., *Development and testing of a general amber force field.* J Comput Chem, 2004. **25**(9): p. 1157-1174.
38. J. Aqvist, *Ion-water interaction potentials derived from free energy perturbation simulations.* The Journal of Physical Chemistry, 1990. **94**(21): p. 8021-8024.
39. W.L. Jorgensen, J. Chandrasekhar, J.D. Madura, et al., *Comparison of simple potential functions for simulating liquid water.* The Journal of chemical physics, 1983. **79**(2): p. 926-935.
40. I.S. Joung and T.E. Cheatham, 3rd, *Determination of alkali and halide monovalent ion parameters for use in explicitly solvated biomolecular simulations.* J Phys Chem B, 2008. **112**(30): p. 9020-9041.
41. A.W. Sousa da Silva and W.F. Vranken, *ACPYPE - AnteChamber PYthon Parser interfacE.* BMC Res Notes, 2012. **5**: p. 367.
42. M. Parrinello and A. Rahman, *Crystal structure and pair potentials: A molecular-dynamics study.* Physical review letters, 1980. **45**(14): p. 1196.
43. G. Bussi, D. Donadio, and M. Parrinello, *Canonical sampling through velocity rescaling.* J Chem Phys, 2007. **126**(1): p. 014101.
44. D. Van Der Spoel, E. Lindahl, B. Hess, et al., *GROMACS: fast, flexible, and free.* J Comput Chem, 2005. **26**(16): p. 1701-1718.
45. A.B. Rubenstein, K. Blacklock, H. Nguyen, et al., *Systematic Comparison of Amber and Rosetta Energy Functions for Protein Structure Evaluation.* J Chem Theory Comput, 2018. **14**(11): p. 6015-6025.
46. X. Daura, K. Gademann, B. Jaun, et al., *Peptide folding: when simulation meets experiment.* Angewandte Chemie International Edition, 1999. **38**(1‐2): p. 236-240.
47. J. Borisek, A. Saltalamacchia, A. Galli, et al., *Disclosing the Impact of Carcinogenic SF3b Mutations on Pre-mRNA Recognition Via All-Atom Simulations.* Biomolecules, 2019. **9**(10).
48. I. Massova and P.A. Kollman, *Combined molecular mechanical and continuum solvent approach (MM-PBSA/GBSA) to predict ligand binding.* Perspectives in drug discovery and design, 2000. **18**(1): p. 113-135.
49. J. Borisek, A. Saltalamacchia, A. Spinello, et al., *Exploiting Cryo-EM Structural Information and All-Atom Simulations To Decrypt the Molecular Mechanism of Splicing Modulators.* J Chem Inf Model, 2020. **60**(5): p. 2510-2521.

4. Conclusion and Future Perspectives

During my PhD, I mainly focused on clarifying the relations between Ca^{2+} level, Ca^{2+} related pathway MCU and GBM malignancy.

Firstly, I established experimental parameters to measure intracellular Ca^{2+} by co-staining cells with Fluo-4 AM and Fura Red AM calcium indicators simultaneously and carried out ratiometric calcium imaging experiment with the live-cell imaging setup. This method allows us to record Ca^{2+} signals, meanwhile, to obtain absolute Ca^{2+} concentration.

Secondly, by comparing Ca^{2+} levels in three different cells (human astrocytes, U87 GBM cell line, primary GBM stem cells from patients), we have shown that Ca^{2+} signal level in GBM cells is higher than that in healthy human astrocyte, which is positively correlated to MCU expression levels.

Thirdly, MCU overexpression/knockdown changes intracellular Ca^{2+} signal dynamics, confirming that MCU takes part in Ca^{2+} signal regulation. In particular, MCU silencing in GBM cells dramatically reversed the high proliferation capacity by blocking the cell G1/S transition via declining the transcriptional activation function of cyclin D1 pathway [66, 67].

Fourthly, MCU silencing in U87 GBM cells prevented GBM migration by targeting Rac1.

Altogether, these results indicate that targeting MCU may be an attractive candidate for GBM treatment. I conclude my thesis by pointing out the crucial role of Ca^{2+} regulation in GBM malignancy, which could lead to potential drugs.

References

1. S. Lapointe, A. Perry, and N.A. Butowski, *Primary brain tumours in adults.* Lancet, 2018. **392**(10145): p. 432-446.

2. M.C. Ashby and A.V. Tepikin, *Polarized calcium and calmodulin signaling in secretory epithelia.* Physiol Rev, 2002. **82**(3): p. 701-734.

3. G.R. Monteith, N. Prevarskaya, and S.J. Roberts-Thomson, *The calcium-cancer signalling nexus.* Nat Rev Cancer, 2017. **17**(6): p. 367-380.

4. D. De Stefani, A. Raffaello, E. Teardo, et al., *A forty-kilodalton protein of the inner membrane is the mitochondrial calcium uniporter.* Nature, 2011. **476**(7360): p. 336-340.

5. N. Robil, F. Petel, M.C. Kilhoffer, et al., *Glioblastoma and calcium signaling--analysis of calcium toolbox expression.* Int J Dev Biol, 2015. **59**(7-9): p. 407-415.

6. A. Alvarez-Buylla and J.M. Garcia-Verdugo, *Neurogenesis in adult subventricular zone.* J Neurosci, 2002. **22**(3): p. 629-634.

7. L.N. Sutton, P. Phillips, and B. Lange, *Midline supratentorial tumors.* Neurosurg Clin N Am, 1992. **3**(4): p. 821-837.

8. J.L. Shah, G. Li, J.L. Shaffer, et al., *Stereotactic Radiosurgery and Hypofractionated Radiotherapy for Glioblastoma.* Neurosurgery, 2018. **82**(1): p. 24-34.

9. I. Paw, R.C. Carpenter, K. Watabe, et al., *Mechanisms regulating glioma invasion.* Cancer Lett, 2015. **362**(1): p. 1-7.

10. A.A. Thomas, C.W. Brennan, L.M. DeAngelis, et al., *Emerging therapies for glioblastoma.* JAMA Neurol, 2014. **71**(11): p. 1437-1444.

11. R. Stupp, W.P. Mason, M.J. van den Bent, et al., *Radiotherapy plus concomitant and adjuvant temozolomide for glioblastoma.* N Engl J Med, 2005. **352**(10): p. 987-996.

12. Q. Xie, S. Mittal, and M.E. Berens, *Targeting adaptive glioblastoma: an overview of proliferation and invasion.* Neuro Oncol, 2014. **16**(12): p. 1575-1584.

13. D.L. Silbergeld, R.C. Rostomily, and E.C. Alvord, Jr., *The cause of death in patients with glioblastoma is multifactorial: clinical factors and autopsy*

findings in 117 cases of supratentorial glioblastoma in adults. J Neurooncol, 1991. **10**(2): p. 179-185.

14. S. Imataka, Y. Akiyama, R. Yokoyama, et al., *Transdural Propagation of Glioblastoma Through Foramen Rotundum.* World Neurosurg, 2018. **111**: p. 240-242.

15. S.A. Richard, Y. Ye, H. Li, et al., *Glioblastoma multiforme subterfuge as acute cerebral hemorrhage: A case report and literature review.* Neurol Int, 2018. **10**(1): p. 7558.

16. M. Weller, P. Roth, M. Preusser, et al., *Vaccine-based immunotherapeutic approaches to gliomas and beyond.* Nat Rev Neurol, 2017. **13**(6): p. 363-374.

17. S.J. Bagley, A.S. Desai, G.P. Linette, et al., *CAR T-cell therapy for glioblastoma: recent clinical advances and future challenges.* Neuro Oncol, 2018. **20**(11): p. 1429-1438.

18. A.M. Gardeck, J. Sheehan, and W.C. Low, *Immune and viral therapies for malignant primary brain tumors.* Expert Opin Biol Ther, 2017. **17**(4): p. 457-474.

19. H.F. Zhao, J. Wang, W. Shao, et al., *Recent advances in the use of PI3K inhibitors for glioblastoma multiforme: current preclinical and clinical development.* Mol Cancer, 2017. **16**(1): p. 100.

20. N.J. Krogan, S. Lippman, D.A. Agard, et al., *The cancer cell map initiative: defining the hallmark networks of cancer.* Mol Cell, 2015. **58**(4): p. 690-698.

21. P. Wesseling and D. Capper, *WHO 2016 Classification of gliomas.* Neuropathol Appl Neurobiol, 2018. **44**(2): p. 139-150.

22. D.N. Louis, H. Ohgaki, O.D. Wiestler, et al., *The 2007 WHO classification of tumours of the central nervous system.* Acta Neuropathol, 2007. **114**(2): p. 97-109.

23. D. Lv, Y. Li, W. Zhang, et al., *TRIM24 is an oncogenic transcriptional co-activator of STAT3 in glioblastoma.* Nat Commun, 2017. **8**(1): p. 1454.

24. Q.T. Ostrom, H. Gittleman, P. Liao, et al., *CBTRUS Statistical Report: Primary brain and other central nervous system tumors diagnosed in the United States in 2010-2014.* Neuro Oncol, 2017. **19**(suppl_5): p. v1-v88.

25. C. Rhiner, B. Diaz, M. Portela, et al., *Persistent competition among stem cells and their daughters in the Drosophila ovary germline niche.* Development, 2009. **136**(6): p. 995-1006.

26. C. Alifieris and D.T. Trafalis, *Glioblastoma multiforme: Pathogenesis and treatment.* Pharmacol Ther, 2015. **152**: p. 63-82.

27. P.E. Theodorakis, E.A. Muller, R.V. Craster, et al., *Physical insights into the blood-brain barrier translocation mechanisms.* Phys Biol, 2017. **14**(4): p. 041001.

28. R.K. Oberoi, K.E. Parrish, T.T. Sio, et al., *Strategies to improve delivery of anticancer drugs across the blood-brain barrier to treat glioblastoma.* Neuro Oncol, 2016. **18**(1): p. 27-36.

29. J.D. Lathia, S.C. Mack, E.E. Mulkearns-Hubert, et al., *Cancer stem cells in glioblastoma.* Genes Dev, 2015. **29**(12): p. 1203-1217.

30. D. Garnier, B. Meehan, T. Kislinger, et al., *Divergent evolution of temozolomide resistance in glioblastoma stem cells is reflected in extracellular vesicles and coupled with radiosensitization.* Neuro Oncol, 2018. **20**(2): p. 236-248.

31. A. Arora and E.M. Scholar, *Role of tyrosine kinase inhibitors in cancer therapy.* J Pharmacol Exp Ther, 2005. **315**(3): p. 971-979.

32. C.A. Liu, C.Y. Chang, K.W. Hsueh, et al., *Migration/Invasion of Malignant Gliomas and Implications for Therapeutic Treatment.* Int J Mol Sci, 2018. **19**(4).

33. A. Mintz, D.M. Gibo, B. Slagle-Webb, et al., *IL-13Ralpha2 is a glioma-restricted receptor for interleukin-13.* Neoplasia, 2002. **4**(5): p. 388-399.

34. C.E. Brown, C.D. Warden, R. Starr, et al., *Glioma IL13Ralpha2 is associated with mesenchymal signature gene expression and poor patient prognosis.* PLoS One, 2013. **8**(10): p. e77769.

35. W. Debinski, D.M. Gibo, B. Slagle, et al., *Receptor for interleukin 13 is abundantly and specifically over-expressed in patients with glioblastoma multiforme.* Int J Oncol, 1999. **15**(3): p. 481-486.

36. A. Rodriguez, C. Brown, and B. Badie, *Chimeric antigen receptor T-cell therapy for glioblastoma.* Transl Res, 2017. **187**: p. 93-102.

37. A.J. Ekstrand, N. Sugawa, C.D. James, et al., *Amplified and rearranged epidermal growth factor receptor genes in human glioblastomas reveal*

deletions of sequences encoding portions of the N- and/or C-terminal tails. Proc Natl Acad Sci U S A, 1992. **89**(10): p. 4309-4313.

38. M.S. Islam, *Calcium Signaling: From Basic to Bedside.* Adv Exp Med Biol, 2020. **1131**: p. 1-6.

39. R.J. Williams, *Calcium.* Methods Mol Biol, 2002. **172**: p. 21-49.

40. R.Y. Tsien, T. Pozzan, and T.J. Rink, *Calcium homeostasis in intact lymphocytes: cytoplasmic free calcium monitored with a new, intracellularly trapped fluorescent indicator.* J Cell Biol, 1982. **94**(2): p. 325-334.

41. R.Y. Tsien, *A non-disruptive technique for loading calcium buffers and indicators into cells.* Nature, 1981. **290**(5806): p. 527-528.

42. A.S. Walker, G. Neves, F. Grillo, et al., *Distance-dependent gradient in NMDAR-driven spine calcium signals along tapering dendrites.* Proc Natl Acad Sci U S A, 2017. **114**(10): p. E1986-E1995.

43. M. Tada, A. Takeuchi, M. Hashizume, et al., *A highly sensitive fluorescent indicator dye for calcium imaging of neural activity in vitro and in vivo.* Eur J Neurosci, 2014. **39**(11): p. 1720-1728.

44. B. Katz and R. Miledi, *The role of calcium in neuromuscular facilitation.* J Physiol, 1968. **195**(2): p. 481-492.

45. M. Nishiyama, K. Hong, K. Mikoshiba, et al., *Calcium stores regulate the polarity and input specificity of synaptic modification.* Nature, 2000. **408**(6812): p. 584-588.

46. M.A. Di Castro, J. Chuquet, N. Liaudet, et al., *Local Ca2+ detection and modulation of synaptic release by astrocytes.* Nat Neurosci, 2011. **14**(10): p. 1276-1284.

47. B. Tombal, S.R. Denmeade, J.M. Gillis, et al., *A supramicromolar elevation of intracellular free calcium ([Ca(2+)](i)) is consistently required to induce the execution phase of apoptosis.* Cell Death Differ, 2002. **9**(5): p. 561-573.

48. J. Wu, A.S. Abdelfattah, L.S. Miraucourt, et al., *A long Stokes shift red fluorescent Ca2+ indicator protein for two-photon and ratiometric imaging.* Nat Commun, 2014. **5**: p. 5262.

49. S. Shimozono, T. Fukano, T. Nagai, et al., *Confocal imaging of subcellular Ca2+ concentrations using a dual-excitation ratiometric indicator based on green fluorescent protein.* Sci STKE, 2002. **2002**(125): p. pl4.

50. C. Lohr, *Monitoring neuronal calcium signalling using a new method for ratiometric confocal calcium imaging.* Cell Calcium, 2003. **34**(3): p. 295-303.

51. R.M. Paredes, J.C. Etzler, L.T. Watts, et al., *Chemical calcium indicators.* Methods, 2008. **46**(3): p. 143-151.

52. V.A. Cuddapah, S. Robel, S. Watkins, et al., *A neurocentric perspective on glioma invasion.* Nat Rev Neurosci, 2014. **15**(7): p. 455-465.

53. T. Demuth and M.E. Berens, *Molecular mechanisms of glioma cell migration and invasion.* J Neurooncol, 2004. **70**(2): p. 217-228.

54. N. Prevarskaya, R. Skryma, and Y. Shuba, *Calcium in tumour metastasis: new roles for known actors.* Nat Rev Cancer, 2011. **11**(8): p. 609-618.

55. J.M. Kim, M. Lee, N. Kim, et al., *Optogenetic toolkit reveals the role of Ca2+ sparklets in coordinated cell migration.* Proc Natl Acad Sci U S A, 2016. **113**(21): p. 5952-5957.

56. F.C. Tsai, A. Seki, H.W. Yang, et al., *A polarized Ca2+, diacylglycerol and STIM1 signalling system regulates directed cell migration.* Nat Cell Biol, 2014. **16**(2): p. 133-144.

57. C. Zitt, B. Strauss, E.C. Schwarz, et al., *Potent inhibition of Ca2+ release-activated Ca2+ channels and T-lymphocyte activation by the pyrazole derivative BTP2.* J Biol Chem, 2004. **279**(13): p. 12427-12437.

58. J. Xu, N. Galvanetto, J. Nie, et al., *Rac1 Promotes Cell Motility by Controlling Cell Mechanics in Human Glioblastoma.* Cancers (Basel), 2020. **12**(6).

59. J.M. Cook-Mills, J.D. Johnson, T.L. Deem, et al., *Calcium mobilization and Rac1 activation are required for VCAM-1 (vascular cell adhesion molecule-1) stimulation of NADPH oxidase activity.* Biochem J, 2004. **378**(Pt 2): p. 539-547.

60. F.M. Davis, I. Azimi, R.A. Faville, et al., *Induction of epithelial-mesenchymal transition (EMT) in breast cancer cells is calcium signal dependent.* Oncogene, 2014. **33**(18): p. 2307-2316.

61. K.M. Yamada and M. Sixt, *Mechanisms of 3D cell migration.* Nat Rev Mol Cell Biol, 2019. **20**(12): p. 738-752.

62. C.R. Kahl and A.R. Means, *Regulation of cell cycle progression by calcium/calmodulin-dependent pathways.* Endocr Rev, 2003. **24**(6): p. 719-736.

63. J.G. Chafouleas, L. Lagace, W.E. Bolton, et al., *Changes in calmodulin and its mRNA accompany reentry of quiescent (G0) cells into the cell cycle.* Cell, 1984. **36**(1): p. 73-81.

64. G. Pande, N.A. Kumar, and P.S. Manogaran, *Flow cytometric study of changes in the intracellular free calcium during the cell cycle.* Cytometry, 1996. **24**(1): p. 55-63.

65. N. Takuwa, W. Zhou, M. Kumada, et al., *Ca(2+)-dependent stimulation of retinoblastoma gene product phosphorylation and p34cdc2 kinase activation in serum-stimulated human fibroblasts.* J Biol Chem, 1993. **268**(1): p. 138-145.

66. C.J. Sherr and J.M. Roberts, *CDK inhibitors: positive and negative regulators of G1-phase progression.* Genes Dev, 1999. **13**(12): p. 1501-1512.

67. J.Y. Kato and C.J. Sherr, *Inhibition of granulocyte differentiation by G1 cyclins D2 and D3 but not D1.* Proc Natl Acad Sci U S A, 1993. **90**(24): p. 11513-11517.

68. R. Sonntag, N. Giebeler, Y.A. Nevzorova, et al., *Cyclin E1 and cyclin-dependent kinase 2 are critical for initiation, but not for progression of hepatocellular carcinoma.* Proc Natl Acad Sci U S A, 2018. **115**(37): p. 9282-9287.

69. Y. Arata, M. Fujita, K. Ohtani, et al., *Cdk2-dependent and -independent pathways in E2F-mediated S phase induction.* J Biol Chem, 2000. **275**(9): p. 6337-6345.

70. T. Ma, B.A. Van Tine, Y. Wei, et al., *Cell cycle-regulated phosphorylation of p220(NPAT) by cyclin E/Cdk2 in Cajal bodies promotes histone gene transcription.* Genes Dev, 2000. **14**(18): p. 2298-2313.

71. M. Winey, *Cell cycle: driving the centrosome cycle.* Curr Biol, 1999. **9**(12): p. R449-452.

72. Y. Han, C. Liu, D. Zhang, et al., *Mechanosensitive ion channel Piezo1 promotes prostate cancer development through the activation of the Akt/mTOR pathway and acceleration of cell cycle.* Int J Oncol, 2019. **55**(3): p. 629-644.

73. J. Choi and M. Husain, *Calmodulin-mediated cell cycle regulation: new mechanisms for old observations.* Cell Cycle, 2006. **5**(19): p. 2183-2186.

74. H.L. Roderick and S.J. Cook, *Ca2+ signalling checkpoints in cancer: remodelling Ca2+ for cancer cell proliferation and survival.* Nat Rev Cancer, 2008. **8**(5): p. 361-375.

75. J. Jeong, J.N. VanHouten, P. Dann, et al., *PMCA2 regulates HER2 protein kinase localization and signaling and promotes HER2-mediated breast cancer.* Proc Natl Acad Sci U S A, 2016. **113**(3): p. E282-290.

76. S.K. Frandsen, H. Gissel, P. Hojman, et al., *Direct therapeutic applications of calcium electroporation to effectively induce tumor necrosis.* Cancer Res, 2012. **72**(6): p. 1336-1341.

77. M. Ott, V. Gogvadze, S. Orrenius, et al., *Mitochondria, oxidative stress and cell death.* Apoptosis, 2007. **12**(5): p. 913-922.

78. I.W. Cheney, D.E. Johnson, M.T. Vaillancourt, et al., *Suppression of tumorigenicity of glioblastoma cells by adenovirus-mediated MMAC1/PTEN gene transfer.* Cancer Res, 1998. **58**(11): p. 2331-2334.

79. D.M. Li and H. Sun, *PTEN/MMAC1/TEP1 suppresses the tumorigenicity and induces G1 cell cycle arrest in human glioblastoma cells.* Proc Natl Acad Sci U S A, 1998. **95**(26): p. 15406-15411.

80. N.N. Danial and S.J. Korsmeyer, *Cell death: critical control points.* Cell, 2004. **116**(2): p. 205-219.

81. M. Osswald, E. Jung, F. Sahm, et al., *Brain tumour cells interconnect to a functional and resistant network.* Nature, 2015. **528**(7580): p. 93-98.

82. J. Hamilton, T. Brustovetsky, J.E. Rysted, et al., *Deletion of mitochondrial calcium uniporter incompletely inhibits calcium uptake and induction of the permeability transition pore in brain mitochondria.* J Biol Chem, 2018. **293**(40): p. 15652-15663.

83. M. Fan, J. Zhang, C.W. Tsai, et al., *Structure and mechanism of the mitochondrial Ca(2+) uniporter holocomplex.* Nature, 2020. **582**(7810): p. 129-133.

84. Y. Kirichok, G. Krapivinsky, and D.E. Clapham, *The mitochondrial calcium uniporter is a highly selective ion channel.* Nature, 2004. **427**(6972): p. 360-364.

85. K.J. Kamer and V.K. Mootha, *The molecular era of the mitochondrial calcium uniporter.* Nat Rev Mol Cell Biol, 2015. **16**(9): p. 545-553.

86. D. De Stefani, R. Rizzuto, and T. Pozzan, *Enjoy the Trip: Calcium in Mitochondria Back and Forth.* Annu Rev Biochem, 2016. **85**: p. 161-192.

87. A. Tosatto, R. Sommaggio, C. Kummerow, et al., *The mitochondrial calcium uniporter regulates breast cancer progression via HIF-1alpha.* EMBO Mol Med, 2016. **8**(5): p. 569-585.

88. S. Marchi, L. Lupini, S. Patergnani, et al., *Downregulation of the mitochondrial calcium uniporter by cancer-related miR-25.* Curr Biol, 2013. **23**(1): p. 58-63.

89. A. Vultur, C.S. Gibhardt, H. Stanisz, et al., *The role of the mitochondrial calcium uniporter (MCU) complex in cancer.* Pflugers Arch, 2018. **470**(8): p. 1149-1163.

90. C. Yu, Y. Wang, J. Peng, et al., *Mitochondrial calcium uniporter as a target of microRNA-340 and promoter of metastasis via enhancing the Warburg effect.* Oncotarget, 2017. **8**(48): p. 83831-83844.

91. M.J. Yoon, A.R. Lee, S.A. Jeong, et al., *Release of Ca2+ from the endoplasmic reticulum and its subsequent influx into mitochondria trigger celastrol-induced paraptosis in cancer cells.* Oncotarget, 2014. **5**(16): p. 6816-6831.

92. T. Ren, H. Zhang, J. Wang, et al., *MCU-dependent mitochondrial Ca(2+) inhibits NAD(+)/SIRT3/SOD2 pathway to promote ROS production and metastasis of HCC cells.* Oncogene, 2017. **36**(42): p. 5897-5909.

93. L. Chen, Q. Sun, D. Zhou, et al., *HINT2 triggers mitochondrial Ca(2+) influx by regulating the mitochondrial Ca(2+) uniporter (MCU) complex and enhances gemcitabine apoptotic effect in pancreatic cancer.* Cancer Lett, 2017. **411**: p. 106-116.

94. X. Zhou, Y. Ren, L. Kong, et al., *Targeting EZH2 regulates tumor growth and apoptosis through modulating mitochondria dependent cell-death pathway in HNSCC.* Oncotarget, 2015. **6**(32): p. 33720-33732.

95. I.S. Song, H.K. Kim, S.R. Lee, et al., *Mitochondrial modulation decreases the bortezomib-resistance in multiple myeloma cells.* Int J Cancer, 2013. **133**(6): p. 1357-1367.

96. C. Giorgi, M. Bonora, S. Missiroli, et al., *Intravital imaging reveals p53-dependent cancer cell death induced by phototherapy via calcium signaling.* Oncotarget, 2015. **6**(3): p. 1435-1445.

97. C.T. Madreiter-Sokolowski, B. Gottschalk, W. Parichatikanond, et al., *Resveratrol Specifically Kills Cancer Cells by a Devastating Increase in the Ca2+ Coupling Between the Greatly Tethered Endoplasmic Reticulum and Mitochondria.* Cell Physiol Biochem, 2016. **39**(4): p. 1404-1420.

98. C. Wiel, H. Lallet-Daher, D. Gitenay, et al., *Endoplasmic reticulum calcium release through ITPR2 channels leads to mitochondrial calcium accumulation and senescence.* Nat Commun, 2014. **5**: p. 3792.

99. C. Loubiere, S. Clavel, J. Gilleron, et al., *The energy disruptor metformin targets mitochondrial integrity via modification of calcium flux in cancer cells.* Sci Rep, 2017. **7**(1): p. 5040.

100. A. Roesch, A. Vultur, I. Bogeski, et al., *Overcoming intrinsic multidrug resistance in melanoma by blocking the mitochondrial respiratory chain of slow-cycling JARID1B(high) cells.* Cancer Cell, 2013. **23**(6): p. 811-825.

101. N. Takata, Y. Ohshima, M. Suzuki-Karasaki, et al., *Mitochondrial Ca2+ removal amplifies TRAIL cytotoxicity toward apoptosis-resistant tumor cells via promotion of multiple cell death modalities.* Int J Oncol, 2017. **51**(1): p. 193-203.

Acknowledgement

My deepest gratitude goes first and foremost to my supervisor, Prof. Vincent Torre, for his consistent guidance and support during my PhD.

I would like to thank Prof. Daniela Cesselli in University Hospital of Udine, Prof. Yili Yang in ISM and Prof. Guosheng Cheng in SINANO for their help and advice.

I would like to express my gratitude to Prof. Michele Mazzanti and Prof. Hugh Robinson for their advices on my PhD thesis.

I would like to thank also all the professors of the Neuroscience area that have given me very useful advice and support, as well for their nice lectures.

My gratitude also goes to all my friends met in SISSA, for their help and the nice and joyful time shared together.

I deeply appreciate my boyfriend. Thank you for your understanding and thank you for always being there.

Last but not least, my gratitude goes to my parents and my brother, for their support and love all through these years.